Sensitivity of the Thermal Structure and Circulation Patterns of a Simple Idealized Lake and Lake Erie to External Driving Forces

by

Funmilayo Adeku

A thesis
presented to the University of Waterloo
in fulfillment of the
thesis requirement for the degree of
Master of Mathematics
in
Applied Mathematics

Waterloo, Ontario, Canada, 2022

Author's Declaration

I hereby declare that I am the sole author of this thesis. This is a true copy of the thesis, including any required final revisions, as accepted by my examiners.

I understand that my thesis may be made electronically available to the public.

Abstract

Lake Erie has been a great source of economic growth and drinking water for both Canada and the United States. All lakes in temperate regions that stratify during summer are prone to hypoxia as they will experience some degree of dissolved oxygen (DO) depletion in the hypolimnion, however, Lake Erie has been very unlucky as it experiences almost all the classes of hypoxic conditions due to its thin hypolimnion. Lately, many researchers focus on Lake Erie to understand the reasons for the abnormally large harmful algal blooms in Lake Erie and its hypoxic and anoxic conditions which has been negatively affecting its aquatic ecosystems and services, water quality, etc., which in turn has impacted the economy.

Understanding the lake's thermal structure and circulation patterns are crucial for precise assessment of the water quality, physics, and biochemical characteristics, and also the effects of climate change on the lake in order to make informed management decisions. In this thesis, the 3-D hydrodynamics MITgcm was used to model a simple Idealized Lake and Lake Erie to study the sensitivity of their thermal structures and circulation patterns to different external driving forces using the two common 2-band short wave parameterizations, Jerlov IA and III and a 3-band short wave radiation model to simulate the motion. The simple idealized lake was forced with South-North linearly varying winds, long wave and short wave radiation, relative humidity, and air temperature while Lake Erie was modeled on a 500 m horizontal grid and forced with the meteorological data obtained from the National Water Research Institute of Environment Canada and the National Data Buoy Center for year 2008. The model results from simulating the simple Idealized Lake (the modeled current in the upper layer) has a good agreement with the analytical results, this confirms the robustness of MITgcm model. Our work suggests that the 2-band model (Jerlov IA and III) produced less warm water in the shallow areas than the 3-band model especially during summer period where it (the 3-band model) overestimated the water temperatures, thus, we suggest that the 3-band model should only be employed when modeling deep lakes for accurate predictions of the thermal structure. We also found out that the overly warm water in lakes is due to solar radiation (short wave and long wave radiation) and not the air temperature and the inflow water temperature forcings e.g. (1)the water in the Idealized Lake warms up quickly when we modeled with no shortwave radiation but with long wave and cools down faster when modeled with no long wave and no shortwave and (2) the effects of the changes in external forcings in some of our model have slight influence on the thermal structure at 20 m depth and no impact at 1 m and 10 m depths in the eastern basin and central basin (image not shown).

Acknowledgements

Firstly, I am eternally grateful to the ALMIGHTY, the Beneficent and the Merciful for bringing me this far.

My profound appreciation goes to my supervisors, Professors Kevin Lamb and Marek Stastna for the opportunity of learning under their tutelage, for the impacted knowledge, the guidance, and the endless support throughout my program. Your kindness and patience with me, at my lowest moments is unquantifiable.

I would also like to acknowledge all my colleagues at the Fluid Lab, Lake Futures, and my office mates especially Ala'. Thank you Yangxin for being always ready to provide answers to all my research questions and personal concerns even after you have graduated.

Further, I want to sincerely appreciate my thesis committee members, Professors Micheal Waite and Francis Poulin for accepting to review my work.

I am so much thankful to Lake Futures for sponsoring this study and earnestly grateful to Great Lakes Environmental Research Laboratory, National Water Research Institute of Environment Canada, and the National Data Bouy Center supplying meteorological data and bathymetry.

To my biggest fans, my lovely sons, Fouad and Abdul-Malik, you have been my greatest strength and the reason I kept pushing! Thank you for your understanding on days that I had to turn down "family movie nights" or cancel extra curricula activities because of a deadline. Your maturity is applaudable. Look at us, we have grown! Mama has added another feather to her cap.

To my dear Mom, you have shown me the true meaning of sacrifice. You left everything including your comfort zone to an entirely new environment to support me in many ways on this journey, I am truly grateful for the gift of your love. I know you are proud of me already.

I would also like to acknowledge my sisters, Rahmat and Shola, for the usual care and support. Thank you for being there each time I needed you.

And finally to my girls and cheerleaders, Asmau, Jelilat, Wunmi, Kemi, Qudroh, Meenah, Kanwulia, Maggie, and Doyin thank you for being my strong support system. It was a tough journey but WE DID IT!!! I appreciate and love you all.

Dedication

This thesis is dedicated to my lovely sons, Fouad and Abdul-Malik.

Table of Contents

List of Figures

List of Tables

Chapter 1

Goals and Outline of the Thesis

The main goals of this thesis are: (1) To examine the sensitivity of the circulation patterns and thermal structure of idealized lakes and Lake Erie for short (8 days) and seasonal (180 days) time periods to different driving forces using the 2-band (Jerlov IA, IB, and III) and a 3-band short wave radiation as implemented in the MITgcm model to simulate the motion. (2) To compare the results from our models for the period and locations of interest and make conclusions accordingly.

The thesis is organized as follows:
In chapter 2, we discuss different types of lakes as characterized by the occurrence of lake–wide mixing events. We introduce some terms (such as thermal stratification, eutrophication, hypoxia, etc.) that are relevant to the thesis and which also shed more light on why significant researcher efforts have recently focused on Lake Erie.

Chapter 3 focuses on the physical processes in lakes and some of the driving forces, with more emphasis on solar radiation and wind forcing. This is done, because these two physical drivers have a proven influence on the seasonal variation of temperature distribution in lakes.

In chapter 4, we discuss model equations (e.g. conservation laws) and some theory relevant to this thesis.

Chapter 5 describes the model used for our simulations, the MITgcm, how it was developed and the theories behind its development. The model setups for both the Toy Lake and

Lake Erie configurations are presented here as well.

Chapter 6 and 7 both report on simulations using the MITgcm to model the Toy Lake and Lake Erie, respectively. These two chapters could be presented together, however we decided to separate them for easy navigation between the two lakes of interest. In these chapters we describe our models based on the driving forces employed, presents the results from our models in form of images and plots, and then compare the results.

Chapter 8 outlines our conclusion from simulating the motion in both idealized lakes and Lake Erie using various driving forces and outlines possible future work.

Chapter 2

Introduction

2.1 Lakes

A lake is a large body of water localized in a basin and surrounded by land ([24]; [43] [19]. Most lakes are fed and drained by rivers and streams. They can be natural (those that are found in mountainous areas, rift zones, or areas that have gone through glaciation e.g. lakes in northern Ontario) or artificially constructed for reasons like industrial, domestic (drinking), agriculture, recreation, hydro-electricity generation, etc. There are about 1.42 millions lakes in the world with varied depth, area, and volume ([4]; [19]; [43]). Canada is estimated to home about 60% of the total number of lakes in the world with $879,800$ lakes.

Most of the lakes on Earth lie in the Northern Hemisphere at higher latitudes and are freshwater ([4]; [19]; [43]). Further, most lakes have at least one natural outflow (e.g river or stream). Lakes without a natural outflow drain their excess water through evaporation or underground seepage or both [43]. There are five Laurentian Great Lakes in North America; **Lake Superior** ($82,000\ km^2$) , **Lake Huron** ($60,000\ km^2$), **Lake Michigan** ($58,000\ km^2$), **Lake Erie** ($25,700\ km^2$), and **Lake Ontario** ($19,000\ km^2$) ([4]; [19]; [43]).

Lakes play an important role in influencing the ecology and weather patterns of an area, in fact, all the lakes in the world (together) have profound effects on the global climate [39]. A lake's health depends greatly on the dissolved oxygen concentration which also determines the amount of aquatic plants and animals in the lake ([39]; [13]).

Nitrogen and phosphorus are the most common nutrients in lakes. They are usually products of influxes from runoff and human activities [39]. Nitrogen and phosphorus are very important for the growth of aquatic plants and animals such as algae, bacteria, etc.; they support the aquatic ecosystem at the base of the food web [13]. However, when these nutrients are in abundance (eutrophication, more details on this later), it leads to continuous rapid multiplication (reproduction) of the aquatic plants and animals, then consequently increases the rates of respiration and decomposition, which will subsequently cause oxygen depletion in some parts or throughout the lake.

2.1.1 Lake Zones

Most lakes have three distinct zones, except for some really deep lakes that have four zones.

1. **The Littoral Zone** is the near shore and shallow portion of the lake where sunlight penetrates to the bottom of the lake to aid photosynthesis for the growth of aquatic plants.

   It was defined by the Minnesota Department of Natural Resources as the portion of the lake that is 15 feet or 4.572 m in depth.

2. **The Limnetic or Pelagial Zone** is the open area of the lake where light does not penetrate to the bottom, it is away from the bottom and at the same time far from the shoreline [24]. The major difference between littoral and the limnetic zones is that the littoral zone supports growth of rooted plants which is impossible in the limnetic zone because of the lack of sunlight to aid photosynthetic-activities.

3. **The Benthic Zone** is the bottom that is covered by an area of mud, rocks, gravel, etc. where animals live.

4. **Profoundal Zone** is the deepest portion of an extremely deep lake (e.g. Lake Baikal in Russia); below the range of light penetrations.

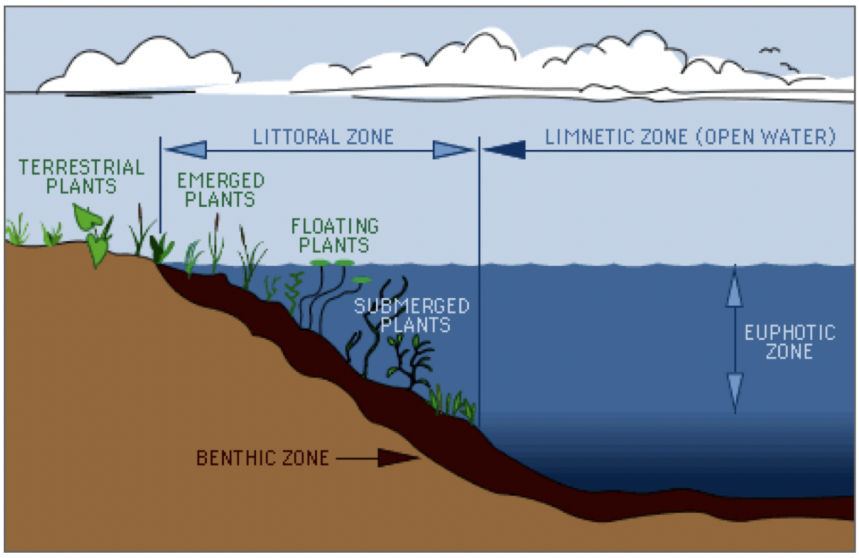

Figure 2.1: Schematic showing the three distinct zones of a lake [32].

2.1.2 Types of Lakes

Lakes can be classified into three categories based on the number of times mixing events or overturns occur in a year [24].

1. **Holomictic Lakes** mix one or more times per year down to the bottom [24]. They are lakes in which the temperature and the density are uniform from the surface to the bottom at a specific time of the year, this results in complete mixing of the lake [27]. Most lakes are holomictic. There are four types of holomictic lakes; **monomictic lakes**, **dimictic**, **polymictic lakes**, and **oligomictic lakes**.

   (a) **Monomictic Lakes** are lakes that mix from the surface to the bottom during one mixing period each year [45]. Monomictic lakes can be grouped into two sub-categories;

      i. **Warm monomictic** are lakes that are never frozen, mix one per year, and are stably stratified for the rest of the year ([27]; [45]). During summer, the waters at the surface and bottom do not mix due to the difference in the densities. During winter, the temperature of the surface water is equal

to the bottom water, thus, there is no significant stratification formed and consequently, the lakes mix thoroughly from the surface to the bottom throughout the winter. They can be found in both temperate and tropical climate regions.

ii. **Cold monomictic** are lakes that are covered by ice for most of the year, warms sufficiently enough to thaw but the temperature does not exceed $4^o C$, thus the ice inhibits mixing during winter ([27]; [45]). During summer, there is no major stratification formed, hence, the lake mix thoroughly from the surface to the bottom. These types of lakes are common in cold climate regions.

(b) **Polymictic lakes** are never ice-covered, do not develop serious stratification as a result of their shallowness, hence, they experience several episodes of complete mixing per year. ([27]; [46]). Even though these kinds of lake are often well mixed from the surface to the bottom on average, however, some weak and temporary stratification can be formed during low-wind periods. Like monomictic lakes, polymictic lakes can also be grouped into two sub-categories;

i. **Warm polymictic lakes** are found in region that does not develop ice-cover during winter [27].
ii. **Cold polymictic lakes** are lakes that are ice-covered during winter period [27].

(c) **Dimictic Lakes** are lakes whose temperature difference between the surface and bottom is negligible twice per year, in spring and fall ([27]; [24]; [41]). They are ice-covered for some part of the year, stably stratified for some part of the year, and mix in spring and fall. Lake Superior is an example of a dimictic lake.

(d) **Oligomictic Lakes** are never ice-covered, stratified for most part of the time, however cooling enough to mix in some years but not in others ([27]; [24]).

2. **Meromictic Lakes** are lakes that have layers of water that do not intermix for years, decades, or centuries, that is, they rarely mix completely to the bottom ([24]; [44]). Stratification in this type of lake can be endogenic caused by internal events like

accumulation of organic materials in the sediment and decaying or ectogenic which is caused by external events such as intrusion of saltwater settling in the hypolimnion. Meromictic lakes are divided into three distinct layers.

(a) **Mixolimnion** is the top layer and behaves essentially like holomictic lakes.

(b) **Chemocline or Chemolimnion** is the middle layer.

(c) **Monimolimnion** is the bottom layer and experience hypoxia with the dissolved oxygen concentration less than 1 $mg\ L^{-1}$ and saltier than the other parts of the lake due to the lack of mixing between the layers.

3. **Amictic Lakes** are lakes that are ice-covered always and can be found in Arctic, Antarctic, and alpine regions ([27]; [40]). They exhibit inverse cold water stratification, that is, the water temperature increase with depth. These lakes may experience melting around their perimeters during summer.

2.1.3 Eutrophication

One of the major issues affecting a lake's health is **eutrophication**. It happens in the presence of excess nutrients like phosphorus and/or nitrogen in the lake mostly as a result of runoff from the farmland, untreated sewage, etc. This process usually results in increased plants growth and algal blooms, increased oxygen demand and low or no oxygen production, and subsequently fish death due to insufficient oxygen ([34]; [36]; [14]).

2.1.4 Lake Erie and its Geometry

Lake Erie is the fourth largest Laurentian Great Lake by area. It is about 400 km long and 90 km wide [5]. It is the shallowest, smallest by volume, most biologically productive, the southernmost of the Laurentian Great Lakes, and the eleventh largest globally by surface area ([5]; [38]). It is situated on the international boundary between Canada and the United States. Lake Erie is situated below Lake Huron and to the west of Lake Ontario ([5]; [48]). Its shore length, area, and water volume are 1286 km, 25700 km^2, and 545 km^3, respectively with a mean depth of 19 m ([5]; [24]). Lake Erie has three distinct basins; the shallow part with average depth of 7.4 m is called the **western basin**,

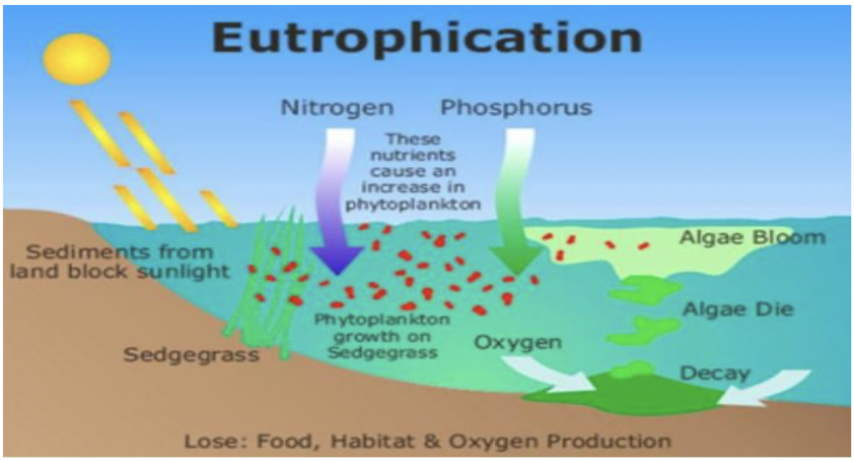

(a)

(b)

(c)

Figure 2.2: (a) The Process of Eutrophication, (b) Sample of eutrophication in a water body, and (c) Implications of eutrophication on fishes ([14]; [10]).

the **central basin** is characterized by its relatively flat topography, has average depth of 18.5, and the deepest part with maximum and average depths of 64 m and 24.4 m respectively is called the **eastern basin** (see 2.3) ([5]; [9]; [31]). The western and central basins are separated by Point Pelee while Long Point separates the central and the eastern basins.

Because Lake Erie is large, it is affected by the Earth's rotation. Its Rossby number (details on this later) is about 0.1; the ratio of the inertial force to the Coriolis force in the Navier-Stokes equation (4.9).

Lake Erie's primary inlet is the Detroit River and main outlet is the Niagara River into

Lake Ontario which is a source of hydroelectric supply to Canada and the United States [5]. Lake Erie has a relatively small water retention time of 2.6 years and it is the warmest of the five Great Lakes because of its small size and shallowness ([17]; [12]). Its internal Rossby radius, ratio of the phase speed of the internal wave, C_I to the Coriolis force, f is O(5) km [5], which is why the Earth's rotation has great influence on the internal wave in Lake Erie since its Rossby radius is less than its lateral dimension (e.g. [47]). Circulation in Lake Erie is driven by a combination of tributary flow (e.g. inflows from Huron River, Raisin River of Michigan, Maureen River, Sandusky River, Cuyahoga, Grand Rivers of Ohio and Ontario, Cattaraugus Creek of New York, etc.) and wind because of its relatively small volume. Because of the large size of Lake Erie, its circulation is affected by the effects of earth's rotation like other water bodies with about the same size or larger ([5]; [31]).

Approximately 34 million people in both Canada and the United States live in the Great Lakes basin with one-third of the total population residing within the Lake Erie watershed, exposing to enormous stress due to human activities like agriculture, urbanization, and industrialization ([35]; [17]). Lake Erie's watershed is an excellent location for farming because of its soil and low latitude, unfortunately this has caused algal blooms and hypolimnetic hypoxia in the central basin of Lake Erie due to the excess nutrients such as phosphorus entering the lake as a result of the application of fertilizers to the farmland and other human activities.

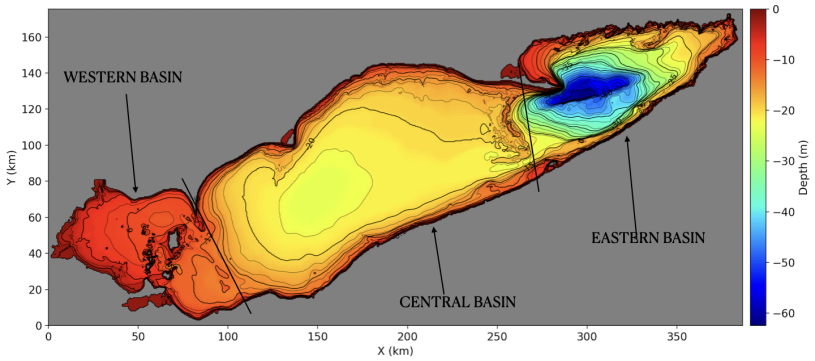

Figure 2.3: Bathymetry of Lake Erie showing its three distinct basins

2.1.5 Geostrophy

Geostrophic balance or geostrophy occurs when there is a balance between the Coriolis force and the pressure gradient force, this results in **geostrophic flow**. In nature, the actual current is usually different from the geostrophic flow due to other forces like friction from the ground and wind stress. Hence, the actual current would be the same as the geostrophic flow if there is no friction and the isobars are straight. Friction slows the flow down and reduces the Coriolis force effect, this gives the pressure gradient force an increased effect while the fluid still moves from high to low pressure with large deflection. Geostrophic flow can be found in the ocean.

Geostrophic flow can be baroclinic (flow in which the fluid density changes with depth) or barotropic (flow whose temperature and density are vertically uniform). A geostrophic flow's direction is usually parallel to the isobars (equal pressure), with the high pressure to the right of the flow in the Northern Hemisphere and to the left of the flow in the Southern Hemisphere([28]; [20]).

The geostrophic equations (2.1) and (2.2) (i.e. there is a dominant balance between the pressure gradient and the Coriolis terms) are simplified versions of the Navier-Stokes equations in a rotating reference frame solved with the assumption that the system is in steady state (neglecting the nonlinear acceleration term).Viscous effects are also negligible.

$$fv = \frac{1}{\rho}\frac{\partial p}{\partial x} \tag{2.1}$$

$$fu = -\frac{1}{\rho}\frac{\partial p}{\partial y} \tag{2.2}$$

where f, ρ, u, v, and p are the Coriolis parameter, density, horizontal velocities in x and y directions, and pressure, respectively.

2.1.6 Thermal Stratification in Lakes

Most lakes in temperate regions separate into three distinct layers due to the difference in temperature during summer when solar energy penetrates through the surface: the epil-

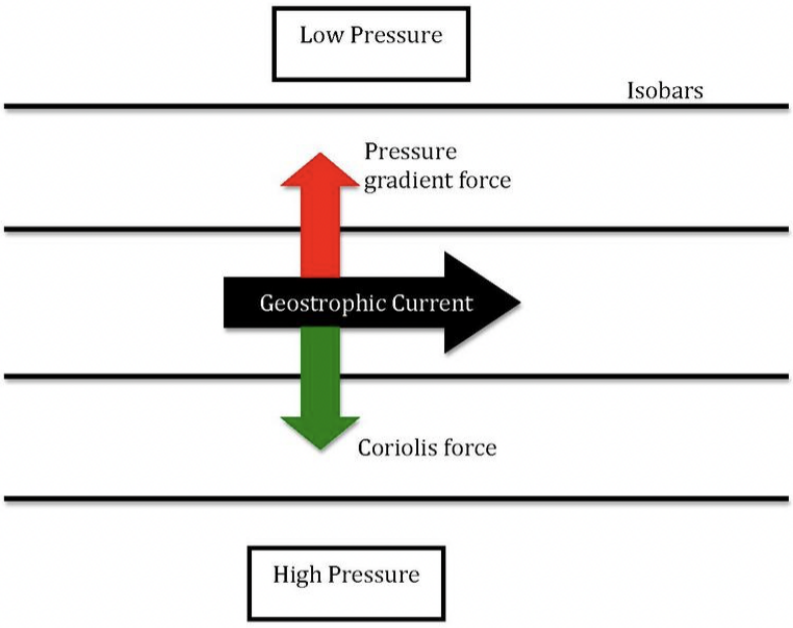

Figure 2.4: Schematic description of the geostrophic flow. Retrieved from [42]

imnion, metalimnion, and hypolimnion ([11]; [25]; [24]).

1. **Epilimnion**: the topmost layer in a thermally stratified lake, the warmest during summer and where most photosynthesis happens. It is also referred to as the surface mixed layer. It is the most dynamic layer with almost uniform temperature; it is the most dynamic because it has the most exposure to sunlight, wind, and human activities, and stimulates processes in other parts of the lake. Oxygen will be close to saturation in this layer due to its exposure to the atmosphere. Most of the important physical processes in the lake take place in this layer.

2. **Metalimnion**: the middle layer in a thermally stratified lake, it is also called the thermocline. It is the thin layer below the epilimnion across which the temperature, density, and other physical factors change rapidly unlike what is experienced in both epilimnion and hypolimnion. The thickness of this layer depends on the seasonal weather variations, latitude, and currents.

3. **Hypolimnion**: the bottom layer in a stratified lake. It is the most dense, coldest during summer, and warmest during winter. This layer can have low oxygen concentrations, less than $2 - 3\ mg/L$ during summer when there is no mixing.

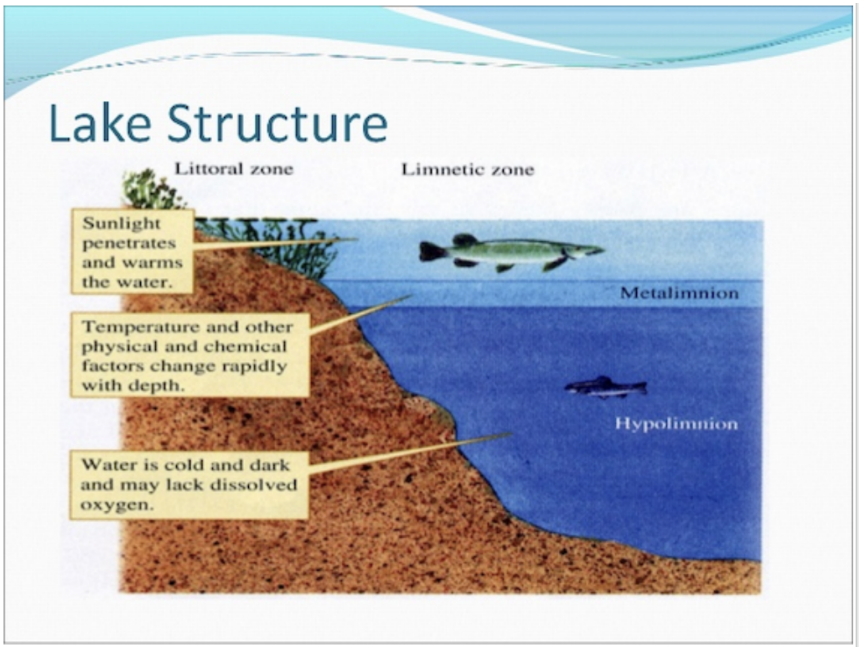

Figure 2.5: Structure of a Stratified Lake. Retrieved from [33]

2.2 Motivations for Studying Lake Erie

About 12 million people (approximately one-third of the total number of human residing in the Great Lakes' watershed [17]) live in Lake Erie's watershed with a larger percentage of the population in the United States' side. It is a great source of drinking water for more than 11 million people ([38]; [17]).

In addition, Lake Erie is a home for agriculture as some parts of the lake's basin have suitable climate for growing crops. Lake Erie serves as a shipping lane for maritime vessels except during winter months when the lake is covered with ice [38].

Lake Erie is also home for commercial and recreational fishing (e.g. recreational walleye fishing especially in the western basin of Lake Erie (Ohio) during the late spring). There are also many public parks (e.g. Point Pelee National Park, Ontario, Long Point Provincial Park, Ontario, Presque Isle State Park, Pennsylvania, etc.) around the lake which makes it safe for biking and other recreational activities including water sports. Lake Erie is also a famous spot for divers since it has many shipwrecks.

Understanding the lake's thermal structure and circulation patterns are crucial for precise assessment of water quality, physics, and biochemical characteristics of the lake, and also the effects of climate on the lake in order to make informed management decisions ([17]; [37]; [8]; [5]; [6]; [31]; [8]).

Lake Erie has been a great source of economic growth for both Canada and the United States. Many researchers focus on Lake Erie lately to understand the reason for the abnormally large harmful algal blooms in the lake and hypoxic and anoxic conditions which has been negatively affecting the aquatic ecosystems and its services, water quality, etc., which in turn has impacted the economy ([5]; [37]).

2.2.1 Hypoxia

Hypoxia or hypoxic condition arises when there is oxygen depletion, reduction in the concentration of dissolved oxygen (DO) to a level where it becomes detrimental to the aquatic ecosystems and their services. Although many researchers estimated the range of oxygen concentration level that gives rise to hypoxia to be between $2 - 4\ mg/L$; for example, [2] stated that DO concentration between $1 - 2\ mg/L$ has negative effects on many aquatic ecosystems while [23] noticed that the survival rate for some of the aquatic organisms decreased when the DO concentration level goes below $3\ mg/L$. However, the DO concentrations that likely have detrimental effects on aquatic organisms varies from class of the aquatic organisms to the environment and the length of exposure, which is why [37] defined **hypoxia** as any situation in which the reduction of the DO concentrations has significant negative impacts on aquatic ecosystems and its services.

Different factors such as increased or reduced temperature, runoff from farmland (i.e. nutrients), storm activities, etc., also contribute to the development of hypoxic condition [15]. [37] classified hypoxic conditions in Great Lakes into four distinct groups namely

hypolimnetic, diel, over-winter, and episodic based on the processes that give rise to the each condition.

All lakes in temperate regions that stratify during summer are prone to hypoxia as they will experience some degree of DO depletion in the hypolimnion, this is basically, why summer stratification is the main cause of hypolimnetic hypoxia since the strong stratification in the metalimnion inhibits the downward mixing of oxygen thus isolates it from the atmosphere; this happens throughout summer period and continues until fall when the surface waters cool down and results in lake turnover which restore the DO concentration [37].

Hypoxia in Great Lakes has been major concern for many years. In particular, Lake Erie has been very unlucky as it experiences almost all the hypoxic conditions due to its thin hypolimnion, with the hypolimnetic and over-winter hypoxia being the main concerns. For instance, Lake Erie has the highest Annual Maximum Ice Coverage among the five Laurentian Great Lakes based on the estimate of the long-term mean between 1973 and 2010 ([37]; [5]; [48]), the ice cover blocks the air-water interface and reduces the penetration of light, and subsequently hinders the production of oxygen as photosynthesis will not be able to take place ([37]; [21]. Also, during the summer period the central and western basins of Lake Erie develop stratification and subsequently hypoxic conditions at the bottom of the lake (hypolimnion) due to its thinness (depth of the hypolimnion) as a result of the rise in temperature at the surface and the reduced wind-driven mixing because of the summer thermocline (e.g. the bowl-shaped thermocline in offshore of the central basin of Lake Erie reduces the volume of the hypolimnetic water which in turn hasten the oxygen depletion rate in the basin) [37]; [6]).

During mid the 1960s and early 1970s, in an effort to reduce the negative effects of hypoxia in Laurentian Great Lakes and their watersheds, the governments of the USA and Canada passed a bi-national Great Lakes Water Quality Agreement (GLWQA) and restated in the review in 2012 [15]. At the time, it was believed that the phosphorus (P) load had significant effects on hypoxia. Thus, one of the objectives of GLWQA was to maintain the DO concentration in the hypolimnion of the central basin of Lake Erie by reducing the amount of external P load to Lake Erie from 30 Gg per year that was experienced earlier to 11 Gg per year. This goal was met by the mid 1980s and remains close to the target load with some variations annually due to the weather. However, since the mid 1990s there have been increased in algal blooms and subsequently hypolimnetic hypoxia occurs annually in various intensities, and as a result the general lake's health was impacted negatively.

Even though there was overall decrease in nutrients load, however, the Hypolimnetic Oxygen Depletion (HOD) rate in the central basin of Lake Erie increased [37]. The reasons for the relapse has not been completely identified. [15] stated that apart from the external P load, other factors such as hypolimnion thickness since it depends on the water level, diurnal stratification, climate change, etc. affect the HOD. Conroy et al., 2010 found that increase in storm activity results in increase vertical mixing, deoxygenation in the hypolimnion, and subsequently increase in HOD rates in the Sandusky sub-basin; they suggested that the temporal and spatial sampling analysis should be included when developing a model to determine the HOD rates in aquatic ecosystems [15].

Consequently, the effects of hypoxia/anoxia on Lake Erie's health and the subsequent negative impacts on the economy have been the reasons for the recent focus on Lake Erie by researchers and lake managers.

Chapter 3

Physical Drivers of Lake Motion

Physical processes in lakes, such as thermal stratification, mixing, eutrophication, etc. are driven by external forcing. Examples of external forcing include short wave radiation, long wave radiation, air temperature, humidity, wind, influx from tributaries, etc. Thus, external drivers are crucial in accurate, predictive modeling of lakes.

In this chapter we talk about some physical processes in lakes and some of the driving forces. More emphasis is placed on solar radiation and wind forcing as they have both been proven to be major factors influencing the seasonal and sub-seasonal variation of the temperature distribution in lakes [24].

Solar Radiation

Solar radiation is a major source of energy that drives circulation in both the atmosphere and the water bodies especially during summer when the effects of the wind curls are less important ([17]; [5]; [7]). It is received at the Earth's surface directly from the sun and also as diffuse radiation from the sky as an electromagnetic waves of different wavelengths [24]. Solar radiation has significant effects on the circulation patterns and also on the thermal structures in lakes and oceans [17]. Its penetration depth depends largely on the turbidity (measure of the relative clarity of a fluid) of the water. Factors such as runoff from storms, build up of dissolved colored organic matters, algae, etc. influence the turbidity of a water body.

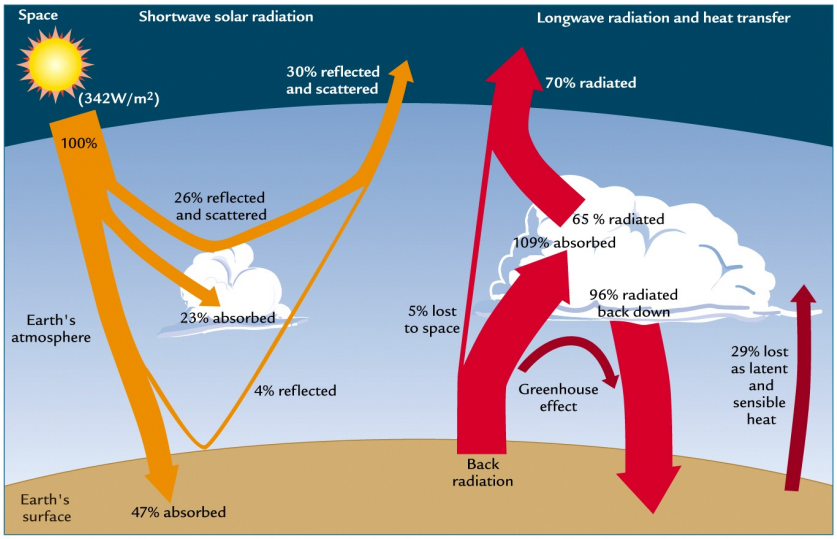

Figure 3.1: Schematic diagram showing the Earth-Atmosphere energy balance [18].

Short wave radiation (e.g. in the visible range of wavelengths) has a higher amount of energy compared to long wave radiation. The sun emits radiation over a large range of wavelengths. Radiation from the sun varies diurnally and over the course of the year due to variations in the Earth's tilt and the distance from the sun. The Earth emits long wave (or infrared) radiation which is a function of its temperature.

Solar radiation incident on the surface of water is divided into

1. short wavelength in the ultra-violet part of the radiation spectrum. It represents 2% of the total incoming solar radiation and its divided into 3 bands, UVA, UVB, and UVC ([17]; [24]),

2. Photosynthetically Active Radiation, PAR; is the visible spectrum and makes up 53% of the total incoming solar radiation ([17]; [24]), and

3. the infrared and near-infrared wavelengths which accounts for the 45% of the total solar radiation ([17]; [24]).

Parameterization of shortwave radiation in the water column determines the dynamics of the mixed layer. It is usually parameterized as 2-band and 3-band, which involves splitting the solar radiation into two and three parts, respectively with different attenuation coefficients and absorption length scales [17].

2-band parameterization of shortwave radiation is very popular among researchers modeling oceans and lakes' mixed layer, however, more robust and accurate parameterization is require for better understanding of the mixed layer dynamics ([17]; [29]). Andrea and Morel, 1993 [29] discovered "that the 2-band model underestimates the absorption of the solar radiation in the upper few meters of the mixed layer and over-estimates it in the remaining part of the water column". [17] found similar results when they explored the sensitivity of the seasonal evolution of the thermal structure of Lake Erie on parametrizations of vertical mixing and radiative heat fluxes.

Note that for all our idealized lakes simulations, we used the parameterized vertical attenuation of short wave radiation, $Q(z)$ given as in [17], ((3.1)) with (6.2) as Q_{sw}.

$$Q(z) = Q_{sw} \sum_{n=1}^{N} \alpha_n \ \exp\left(\frac{-z}{L_n}\right) \tag{3.1}$$

where, for 12 hours of daylight

$$Q_{sw} = \begin{cases} 500\ W\ m^{-2}\left(1 - \cos\left(\frac{2\pi t}{12\ h}\right)\right) & \text{if } t < 12\ h\text{: t=0 depicts sunrise} \\ 0 & \text{if } t \geq 12\ h\text{: t=12 depicts sunset.} \end{cases} \tag{3.2}$$

(3.2) is for estimating the net incoming shortwave radiation at the surface, and the precise form of this quantity is not necessarily the same in different studies (e.g. (6.2)). $n = 1, 2, 3..., N$ are the number of wave number bands, α_n are the fractions of the insolation resident in the band (that is the attenuation coefficients), with $\sum_{n=1}^{N} \alpha_n = 1$, and L_n is the attenuation length scales. Therefore, for the 2-band and 3-band model, N will be 2 and 3, respectively. The values for all the parameters are given in tables 3.2 and 3.1.

In numerical simulations, such as those with MITgcm model, the emission or absorption of energy from the long wave radiation happens in the upper grid cell, thus the energy is

α_1	α_2	α_3	L_1 (m)	L_2 (m)	L_3 (m)
0.55	0.445	0.005	0.25	1	2.5

Table 3.1: 3-band model: Attenuation coefficients (fraction of the insolation resident in the band) and its extinction length scales reproduced from [17].

Jerlov Water Type	α_1	α_2	L_1 (m)	L_2 (m)
I	0.58	0.42	0.35	23
IA	0.62	0.38	0.6	20
IB	0.67	0.33	1	17
II	0.77	0.23	1.5	14
III	0.78	0.22	1.4	7.9

Table 3.2: 2-band short wave radiation: Attenuation coefficients and its the extinction length scales for different Jerlov water types reproduced from [17].

lost or gained over a subset of the upper mixed layer.

The amount of long wave radiation that is emitted depends on the surface temperature. At the Earth's surface, the higher the surface temperature, the greater the long wave radiation emission. Similarly, the higher the atmospheric temperature (energy absorbed from the Earth's surface, water vapour, and cloud cover), the greater the long wave radiation emission; this follows the the Stefan Boltzmann Law (see (3.3) for the quantitative expression).

We want to estimate the cooling of the upper mixed layer after 8 days. In this chapter, we just present general results as such, since we know that the long wave energy emission varies with time, we use the Stefan Boltzmann's Law and the specific heat formula to derive an expression that can be used to estimate how much the initial temperature of the upper mixed layer (temperature at the surface) decreases over a given time. To do this, we explored two options.

Option 1 : Consider a layer of fluid with depth H, assuming energy is lost uniformly from that layer and the layer remains well mixed i.e. temperature is constant in the upper mixed layer. We also assume that the long wave emission is constant in time and use Stefan-Boltzmann's Law to estimate the rate of energy lost per unit area when the temperature of the upper mixed layer, $T_s = 12^oC = 285.15K$ as

$$-j^* = \epsilon\ \sigma\ T_s^4 \tag{3.3}$$

Here $-j^*$, ϵ, σ, and T_s represent the rate of energy lost per unit time per unit area; the emissivity of water, 0.96; Stefan-Boltzmann's constant, $5.67 \times 10^{-8}\ J\ s^{-1}\ K^{-4}$; and the temperature of the upper mixed layer in K respectively.

$$\begin{aligned} -j^* &= 0.96 \times 5.67 \times 10^{-8} J\ s^{-1} K^{-4} \times (285.15K)^4 \times 1\ m^{-2} && (3.4)\\ &= 359.871783\ J\ s^{-1}\ m^{-2} && (3.5)\\ j^* &= -359.871783\ J\ s^{-1}\ m^{-2} && (3.6)\\ &\approx -359.87\ J\ s^{-1}\ m^{-2} && (3.7) \end{aligned}$$

The rate of energy emitted per unit area, j^* can also be represented as

$$j^* = \frac{\Delta E}{\Delta t} \tag{3.8}$$

Here Δt is the change in time (seconds) and ΔE is the change in energy per unit area which can be estimated using the specific heat equation

$$\Delta E = M\ C\ \Delta T \tag{3.9}$$

Here M, C, and ΔT are the mass per unit area (i.e. $\rho\ H$ density of water multiplied by the depth of the water layer), the specific heat capacity of water, and the change in temperature, respectively.

We estimate the change in temperature in the layer of water with thickness H due to the emission of long wave radiation by combining (3.8) and (3.9)

$$\Delta T = \frac{j^* \ \Delta t}{M \ C} \tag{3.10}$$

$$= \frac{-359.871783 \ J \ s^{-1} \ m^{-2} \ \Delta t}{998 \ kg \ m^{-3} \ H \times 4182 \ J \ kg^{-1} \ {}^oC^{-1}} \tag{3.11}$$

$$= \big(-0.86225 \times 10^{-6} \ H \ t \big)^o C \ m^{-1} \ s^{-1} \tag{3.12}$$

From (3.12), we estimate the change in temperature after certain period of time for the specified depth of the water layer H, for example, the temperature after one day (i.e. $t = 86400 \ s$) and 8 (i.e. $t = 691200 \ s$) days for $H = 10 \ m$, are $-0.745 \ {}^oC$ and $-5.959872 \ {}^oC$ respectively. Thus, with the temperature at the surface T_s, $12 \ {}^oC$, we have temperature after one day and 8 days as $T(t = 86400 \ s) = 12 - 0.745 = 11.255 \ {}^oC$ and $T(t = 691200 \ s) = (12 - 5.96) \ {}^oC = 6.04 \ {}^oC$, respectively.

Option 2 : We take into account the time varying temperature of the layer of water i.e. we assume that the long wave emission varies with time and derive an expression for estimating temperature after a given period of time, say $T(t_2)$ for the specified water layer thickness H. From (3.9) we have

$$\Delta T = \frac{\Delta E}{MC} \tag{3.13}$$

Combining (3.3), (3.8), and (3.13), we have

$$\Delta T = \frac{j^* \ \Delta t}{M \ C} \tag{3.14}$$

$$= \frac{-\epsilon \ \sigma \ T^4 \ \Delta t}{M \ C} \tag{3.15}$$

$$\frac{\Delta T}{T^4} = -\frac{\epsilon \ \sigma \ \Delta t}{\rho \ H \ C} \tag{3.16}$$

Taking the limit of (3.16) as $\Delta t \longrightarrow 0$, we get the differential equation

$$\frac{\mathrm{d}T}{\mathrm{d}t} = -\frac{\epsilon \ \sigma \ \ T^4}{\rho \ H \ C} \tag{3.17}$$

Integrating (3.17) over the range of t, we have

$$T(t_2) = \left[\left(\frac{1}{T(t_1 = T_s)}\right)^3 + \frac{3\,\epsilon\,\sigma\,T(t_2 - 0)}{\rho\,H\,C}\right]^{-\frac{1}{3}} \tag{3.18}$$

$$= \left[\left(\frac{1}{T_s)}\right)^3 + \frac{3\epsilon\,\sigma\,T(t_2)}{\rho\,H\,C}\right]^{-\frac{1}{3}} \tag{3.19}$$

Using $\rho = 998\ kg\ m^{-3}$, $H = 10\ m$, $T_s = 285.15\ K$, and $T(t_2 = 86400\ s)$; 1 day and $T(t_2 = 691200\ s)$; 8 days in (3.18), we have $T(86400\ s) = 11.26\ ^oC$ and $T(691200\ s) = 6.28\ ^oC$, which represent the temperatures of the upper mixed layer after one day and 8 days, respectively and thus we have the change in temperature as $-0.74\ ^oC$.

Comparing the results from our two options (Option 1 relative to Option 2), we found out that

1. The change in temperatures after one day are $\Delta T_1 = 0.745\ ^oC$ and $\Delta T_2 = 0.74\ ^oC$ for options 1 and 2 respectively. There is difference is $0.005\ ^oC$ which translates to 0.6756% of ΔT_2 .

2. However, after 8 days the percentage difference increased to 3.8217% with $0.24\ ^oC$ difference between the estimated temperatures.

Therefore, it is safe to say option 2 is better if we are estimating temperature over a long period as errors accumulate over time which makes predictions using option 1 questionable.

Wind Forcing

Wind forcing is the most important factor driving circulation in a water body (i.e. the primary mechanical driver). The most important parameter governing the wind driven

regime is the wind stress (also known as surface-shear stress) τ_s, force per unit area acting on the water surface due to wind [47]. The wind stress from downward eddy-transport of horizontal momentum from the atmosphere ($\tau = \rho_a < U'W' >$; prime represents fluctuations) will act on the water surface due to the wind forcing and can generate waves on the surface of the water body.

Wind stress is usually parameterized by the drag coefficient (see (3.20)) since waves serve as another way of transferring momentum to the water (i.e. produces additional roughness that increase the friction and heightens the wind stress from the air to the water) [47]. The drag coefficient depends on the wind speed, the presence of surface waves, and the wave development (3.21), thus, it is safe to say the wind stress depends on the wind speed and the wave development. Wave development can be estimated from the significant wave height $H_{(1/3)} = 0.051\sqrt{\frac{w_*^2\, X}{g}}$; X is the fetch, the distance traveled by winds/waves across an open water, however, because the value is usually not readily available, most researchers use wave age to estimate the wave development instead of the significant wave height.

$$\tau = \rho_a\, C_{10}\, U^2 \tag{3.20}$$

$$C_{10} \approx \left[k^{-1}\ln\frac{10\ g}{C_{10}U_{10}} + K\right]^{-2} \tag{3.21}$$

where ρ_a is the air density, C_{10} is the drag coefficient for U_{10}, the horizontal wind speed at 10 m above the bottom which can be estimated from (3.22), g is the acceleration due to the gravity, and $K = 11.3$ is the Charnock constant while k is the Von Karman constant [47].

$$U(z) = \frac{w_*}{k}\ln\frac{z}{z_0} \tag{3.22}$$

with z_0 being the length of the roughness given as

$$z_0 = \frac{w_*^2}{g}e^{-kK} \tag{3.23}$$

or approximately $z_0 = 0.0097\ \frac{w_*^2}{g}$, where w_* is the friction velocity in air; $w_* = \frac{\tau}{\rho_a}$ and $\frac{w_*^2}{g}$ is the wave height [47].

Further, the total vertical flux of the momentum at the surface is split into two with one part feeding the current and the other part feeding the waves (see (3.24)), which is why the applied wind stress from the atmosphere is larger than the momentum flux into the surface boundary layer as some of the wind stress is used for transporting and maintaining the waves [47].

$$\tau = \tau_{\text{SBL}} + \tau_{\text{Wave}} \tag{3.24}$$

where $\tau_{\text{SBL}} = \rho < U'W' >$ forces the remaining water underneath the waves and SBL in τ_{SBL} stands for surface boundary layer.

For a given wind speed, the observed surface stress is higher near the shore that is opposite to the direction of the wind (upwind shore) than in the open water and also larger in lakes than open oceans due to the pronounced wave-induced complexity as a result of the limited horizontal extent [47].

In this chapter we have talked about the importance of external forcing such as wind forcing and solar radiation on the physical processes in lakes (e.g. thermal stratification). For all the simulations in this thesis, we use different short wave radiation parameterizations (2-band with various Jerlov water types and the 3-band) using the attenuation coefficients and length scales values provided in tables 3.2 and 3.1 along side with wind forcing; observed meteorology data for Lake Erie and 5.2 for the idealized lake. More details on the external forcing for the Toy Lake and Lake Erie can be found in chapter 5.

Chapter 4

Model Equations and other Theory

4.1 Governing Equations

Continuity Equation

The general form of the continuity equation is given as

$$\frac{1}{\rho}\frac{D\rho}{Dt} + \vec{\nabla} \cdot \vec{U} = 0 \tag{4.1}$$

$$\vec{\nabla} \cdot \vec{U} = 0 \tag{4.2}$$

$$\vec{U} = (u, v, w) \tag{4.3}$$

where ρ is the density of the fluid, $\frac{D}{Dt}$ is the material derivative $\left(\frac{D}{Dt} = \frac{\partial}{\partial t} + \vec{U} \cdot \vec{\nabla}\right)$, $\vec{\nabla} = \frac{\partial}{\partial x} + \frac{\partial}{\partial y} + \frac{\partial}{\partial z}$, and $\vec{U}$ is the fluid velocity.

Momentum Equation

(4.4) is the Navier-Stokes equation for an incompressible fluid

$$\rho \frac{D\vec{U}}{Dt} = -\vec{\nabla} p + \rho g + \mu \nabla^2 \vec{U} \tag{4.4}$$

where p is the pressure, μ is the viscosity, and ∇^2 is the Laplacian operator.

Euler Equation

If the viscous effects in a system are ignored then we have Euler equation (see (4.5)); e.g. ignoring μ in (4.4).

$$\rho \frac{D\vec{U}}{Dt} = -\vec{\nabla} p + \rho g. \tag{4.5}$$

In a rotating reference frame (4.4) becomes

$$\frac{D\vec{U}}{Dt} + 2\Omega \times \vec{U} = -\frac{\vec{\nabla} p}{\rho} + g \tag{4.6}$$

$$2\Omega \times \vec{U} = (-fv, fu, 0) \tag{4.7}$$

where f is the Coriolis parameter ($f = 2\Omega \sin\theta$), θ is the constant latitude, and Ω as the angular velocity.

4.2 Definitions

Boussinesq approximation

Boussinesq approximation is used when the density variations are small, then we can set $\rho = \rho_0 + \tilde{\rho}$, where $\tilde{\rho} \ll \rho_0$, hence $\rho \frac{D\vec{U}}{Dt} \approx \rho_0 \frac{D\vec{U}}{Dt}$ [28]. In the Boussinesq approximation, the change in the densities in (4.1) and (4.4) are neglected except in gravity term where density ρ is multiplied by g and treats other properties (e.g. viscosity; μ, diffusivity; k, specific heat capacity; C_p) as constants. This does not mean the density is constant along the

direction of motion rather the magnitude of $\frac{1}{\rho}\frac{D\rho}{Dt}$ in (4.1) is small relative to the maximum of $[|u_x|, |v_y|, |w_z|]$ ([28]; [20]). See (4.8) for the Navier-Stokes equations of motion using Boussinesq approximation in a rotating frame of reference.

$$\begin{aligned} \frac{Du}{Dt} - fv &= -\frac{1}{\rho_0}\frac{\partial p}{\partial x} \\ \frac{Dv}{Dt} + fu &= -\frac{1}{\rho_0}\frac{\partial p}{\partial y} \\ \frac{Dw}{Dt} &= -\frac{1}{\rho_0}\frac{\partial p}{\partial z} - \frac{\rho}{\rho_0}g \end{aligned} \tag{4.8}$$

Rossby Number: The Rossby number is one of the important parameters in ocean and lake dynamics. It's used to determine the significance of the Earth's rotation in a given process [24]. For instance, if the Rossby number is small, then it means the inertial force is very small and can be neglected; this approximation is usually referred to as **Geostrophic Approximation** while a large Rossby number implies that either the Coriolis force or the horizontal length is small and thus the planetary rotation can be neglected [28]. It can be represented as

$$R_o = \frac{\text{Nonlinear acceleration}}{\text{Coriolis force}} \tag{4.9}$$

$$\approx \frac{U^2 L}{fL} \tag{4.10}$$

$$= \frac{U}{fL} \tag{4.11}$$

where U, f, and L are the horizontal velocity, Coriolis parameter, and the horizontal length, respectively.

Rossby Radius of Deformation, L_D is the length scale of a motion at which the Earth's rotation becomes the main driving force (that is horizontal scale at which the rotation effects is as important as the bouyancy effects) ([24]; [20]). It can be barotropic or baroclinic. For a two layer fluid, the baroclinic Rossby radius is

$$L_D = \frac{1}{f}\sqrt{g\frac{\Delta\rho}{\rho}\frac{h_1 h_2}{H}} = \frac{c}{f} \tag{4.12}$$

where h_1 and h_2 are the thicknesses of the epilimnion and hypolimnion, $H = h_1 + h_2$ is the total water depth, ρ is a reference density and $\Delta\rho$ is the difference, c is the linear long wave speed, and f is the Coriolis parameter. If the ratio of the Rossby radius of deformation to the lake's width is greater than or equal to 1, then the planetary rotation is an important factor for the circulation.

Current in the Upper Layer of a 2-layer Channel

To estimate the current in the upper layer in a 2-layer lake or water body, we derive an expression using the Boussinesq approximation by considering a 2-layer flow in an infinitely long channel of width $2L$ with boundaries at $x = \pm L$ and bottom at $z = -H$.

We assume that the fluid consists of two layers of constant density water with density ρ_1 in the upper layer and density ρ_2 in the lower layer, the flow is motionless at the surface ($z = 0$), and the two layers have constant thickness with h_1 as the upper layer thickness and $h_2 = H - h_1$ as the lower layer thickness while the undisturbed interface is at $z = -h_1 = -H + h_2$ (see figure 4.1).

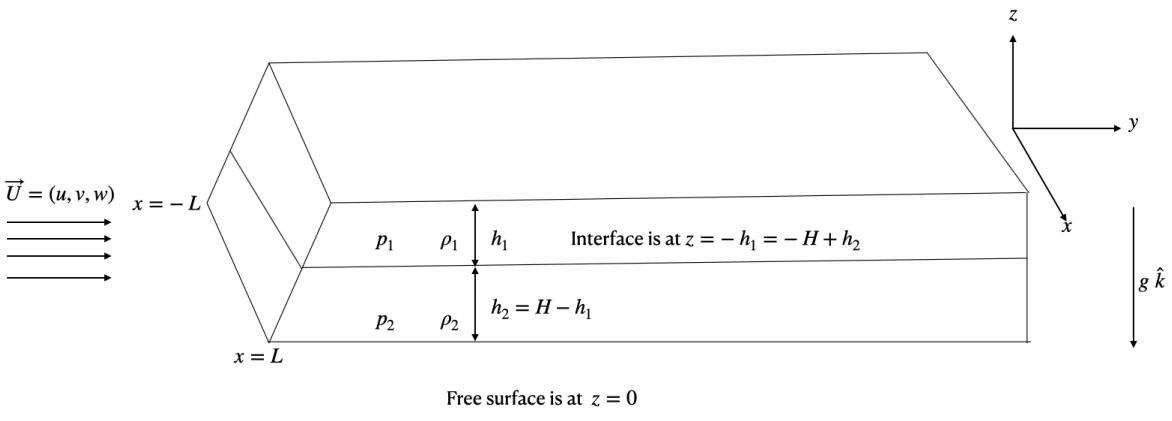

Figure 4.1: Schematic illustration of the initial state of a flow in an infinitely long channel.

Suppose that there is a steady flow along the channel (i.e., $y-$direction only) with the interface between the two layers now at $z = -h_1 - \zeta(x)$ and free surface at $z = \eta(x)$, and $-H < -h_1 + \zeta < \eta$ for all x. The fluid is on an f-plane (i.e., we included rotational effects). Above the water is air at constant atmospheric pressure p_a. Only the along channel velocity component in the upper layer is non-zero i.e. no motion at the bottom layer: $\vec{U} = (0, v(x), 0)$ (see figure 4.2). We ignore the viscous effects and surface tension.

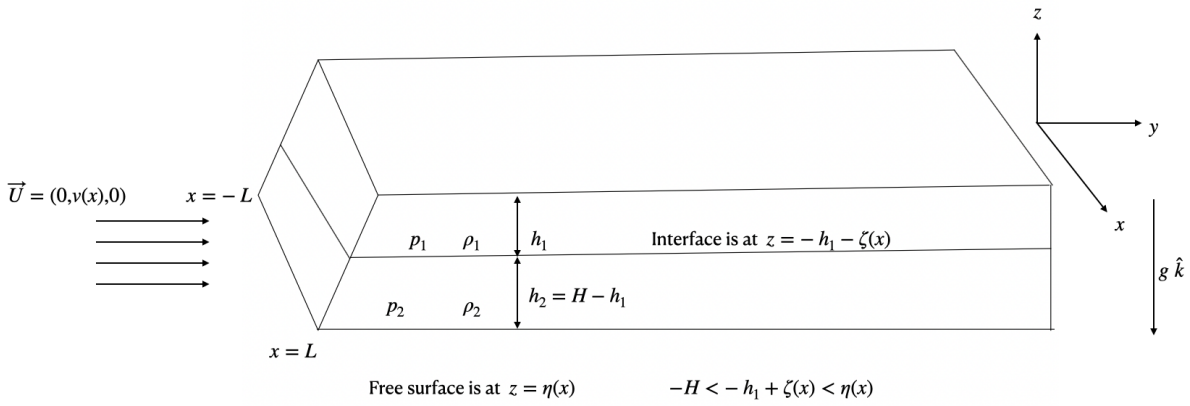

Figure 4.2: Schematic illustration of a flow in an infinitely long channel.

Using (4.3) and (4.7) in (4.6) to get expressions for the x, y and z components of the equations of motion in a rotating reference frame we have

$$\frac{Du}{Dt} - fv = -\frac{1}{\rho}\frac{\partial p}{\partial x} \tag{4.13}$$

$$\frac{Dv}{Dt} + fu = -\frac{1}{\rho}\frac{\partial p}{\partial y} \tag{4.14}$$

$$\frac{Dw}{Dt} = -\frac{1}{\rho}\frac{\partial p}{\partial z} - g \tag{4.15}$$

Geostrophic Flow with a Motionless Bottom Layer

Using the fact that $u = 0$ [i.e. from $\vec{U} = (u, v, w) = (0, v(x), 0)$] in (4.13) we have

$$-fv = -\frac{1}{\rho}\frac{\partial p}{\partial x} \tag{4.16}$$

Also, using the fact that $u = 0$ and $v = v(x)$ in (4.14) we have

$$0 = -\frac{1}{\rho}\frac{\partial p}{\partial y} \tag{4.17}$$

Similarly, using the fact that $w = 0$ in (4.15) we have

$$\frac{\partial p}{\partial z} = -g\rho \tag{4.18}$$

To get the pressure field $p_1(x, z)$ in the upper layer; we integrate (4.18) between z and $\eta(x)$

$$\int_z^{\eta(x)} dp = -\int_z^{\eta(x)} \rho_1 g dz \tag{4.19}$$

$$p\big(x, \eta(x)\big) - p_1(x, z) = -\rho_1 g \left[\eta(x) - z\right] \tag{4.20}$$

$$p_1(x, z) = p\big(x, \eta(x)\big) + \rho_1 g \left[\eta(x) - z\right] \tag{4.21}$$

Note that $p\big(x, \eta(x)\big) = p_a$, therefore using this fact in (4.21) we have

$$p_1(x, z) = p_a + \rho_1 g[\eta(x) - z] \tag{4.22}$$

Similarly, to get the pressure field $p_2(x, z)$ in the lower layer, we integrate (4.18) between z and $-h_1 + \zeta(x)$, having in mind the density in the lower layer is ρ_2

$$p\big(x, -h_1 + \zeta(x)\big) - p_2(x, z) = -\rho_2 g \left[-h_1 + \zeta(x) - z\right] \tag{4.23}$$

$$p_2(x,z) = p\big(x, -h_1 + \zeta(x)\big) + \rho_2 g\left[-h_1 + \zeta(x) - z\right] \tag{4.24}$$

where $p\big(x, -h_1+\zeta(x)\big)$ is the pressure distribution at the interface and can be derived from (4.22) by replacing z with $-h_1 + \zeta(x)$

$$\begin{aligned} p\big(x, -h_1 + \zeta(x)\big) &= p_a + \rho_1 g\left[\eta(x) - \big(-h_1 + \zeta(x)\big)\right] \\ &= p_a + \rho_1 g\eta(x) + \rho_1 g h_1 - \rho_1 g\zeta(x) \end{aligned} \tag{4.25}$$

Substituting (4.25) into (4.24)

$$\begin{aligned} p_2(x,z) &= p_a + \rho_1 g\eta(x) + \rho_1 g h_1 - \rho_1 g\zeta(x) + \rho_2 g\left[-h_1 + \zeta(x) - z\right] \\ &= p_a + \rho_1 g\eta(x) - \rho_2 g z - \Delta\rho g h_1 + \Delta\rho g\zeta(x) \end{aligned} \tag{4.26}$$

where $\Delta\rho = \rho_2 - \rho_1$.

(4.22) and (4.26) give the pressure distributions in the upper and lower layers respectively. Replace z with $-H = -h_2 - h_1$ in (4.26) and obtain an expression for the bottom pressure $p_b(x)$;

$$\begin{aligned} p_b(x) &= p(x,-H) = p_a + \rho_1 g\eta(x) + \rho_2 g h_2 + \rho_1 g h_1 + \Delta\rho g\zeta(x) \\ &= p_b^* + \rho_1 g\eta(x) + \Delta\rho g\zeta(x) \end{aligned} \tag{4.27}$$

where $p_b^* = p_a + \rho_1 g h_1 + \rho_2 g h_2$.

Assuming the volume of each layer is preserved or the area in an $x-z$ slice is preserved, then

$$\int_{-L}^{L} \eta(x)dx = \int_{-L}^{L} \zeta(x)dx = 0 \tag{4.28}$$

We also use (4.27) to derive an expression for the average pressure at the bottom by integrating (4.27) between $x = L$ and $x = -L$ as follows

$$\begin{aligned}\int_{-L}^{L} p_b(x)dx &= \int_{-L}^{L} \big[p_a + \rho_1 g\eta(x) + \rho_2 g h_2 + \rho_1 g h_1 + \Delta\rho g\zeta(x)\big]dx \\ &= 2L\big[p_a + \rho_2 g h_2 + \rho_1 g h_1\big]\end{aligned} \tag{4.29}$$

using the fact that average of $\eta(x)$ and the average of $\zeta(x)$ are zero when each layer is preserved (i.e. (4.28)) in (4.29)

$$\frac{1}{2L}\int_{-L}^{L} p_b(x)dx = p_a + \rho_2 g h_2 + \rho_1 g h_1 \tag{4.30}$$

Thus we have (4.30) as the average value of $p_b(x)$.

From (4.16) and (4.17) we can deduce that p (pressure) is independent of x and y in the lower layer since there is no motion at the lower layer i.e. $v(x) = 0$; this means that the pressure at the bottom is constant, thus we can re-write (4.30) using this fact as

$$p_b = p_a + \rho_2 g h_2 + \rho_1 g h_1 \tag{4.31}$$

Comment: (4.31) implies that the pressure at the bottom balances the sum of the downward forces per unit area acting on the fluid; where the downward forces are the atmospheric pressure on the surface, the gravitational force per unit area on the upper layer and the gravitational force per unit area on the lower layer.

Further, we use the fact that the fluid is motionless in the bottom layer and derive an expression for $\eta(x)$ from (4.27)

$$\begin{aligned}\eta(x) &= \frac{1}{\rho_1 g}\left[p_b - p_a - \rho_2 g h_2 - \rho_1 g h_1 - \Delta\rho g\zeta(x)\right] \\ &= \frac{p_b - p_a}{\rho_1 g} - \frac{\rho_2}{\rho_1}H + \frac{\Delta\rho}{\rho_1}h_1 - \frac{\Delta\rho}{\rho_1}\zeta(x)\end{aligned} \tag{4.32}$$

where $H = h_1 + h_2$

Substituting (4.31) into (4.32) we have

$$\eta(x) = -\frac{\Delta\rho}{\rho_1}\zeta(x) \tag{4.33}$$

It is clear from (4.33) that $\eta(x)$ does not depend on the undisturbed layer thicknesses h_1 and h_2.

From (4.16), we derive an expression for the current $v_1(x)$ in the upper layer

$$v_1(x) = \frac{1}{f\rho_1}\frac{\partial p}{\partial x} \tag{4.34}$$

In (4.34), we have replaced $v(x)$ in (4.16) with $v_1(x)$, the corresponding velocity in the $y-$direction in the upper layer.

Taking the x derivative of (4.22), i.e. the pressure in the upper layer

$$\frac{\partial p}{\partial x} = \rho_1 g\eta_x(x) \tag{4.35}$$

Also, we take the x derivative of (4.33)

$$\eta_x(x) = -\frac{\Delta\rho}{\rho_1}\zeta_x(x) \tag{4.36}$$

Using (4.35) and (4.36) in (4.34), we have $v_1(x)$ in terms of $\eta(x)$ as

$$v_1(x) = \frac{g}{f}\eta_x(x) \tag{4.37}$$

and in terms of $\zeta(x)$ as

$$v_1(x) = -\frac{g}{f}\frac{\Delta\rho}{\rho_1}\zeta_x(x) \tag{4.38}$$

Note that for a **Boussinesq approximation**, $v_1(x)$ is the same and ρ_1 can be replaced with ρ_0 in (4.38), to estimate the geostrophic current in the upper layer using (4.8). We decided not to include the detailed derivation in this thesis as it's similar to everything we have here.

Chapter 5

MITgcm

5.1 Description of MITgcm

The MITgcm (Massachusetts Institute of Technology general circulation model) was developed at the Massachusetts Institute of Technology and was one of the first non-hydrostatic models of the ocean ([1]; [3]; [26]). It was originally formulated to study oceanic, atmospheric, and climate phenomena [17]. It is a numerical computer code written in FORTRAN, which solves the equations of motion governing the ocean and Earth's atmosphere using finite volume technique (in finite volume technique, the governing equations are integrated over finite volumes that make up a discrete grid)([1]; [3]; [26]). The model uses a rectangular horizontal grid and a z-grid. The model was developed based on incompressible Navier-Stokes equations (incompressible Boussinesq equations to be specific; see (4.8)) with the non-hydrostatic terms to accommodate overturning and mixing processes ([17]; [1]; [3]; [26]). The model also uses an Arakawa-C grid for the horizontal discretization and an Adams-Bashforth time-stepping for time discretization.

The combination of non-hydrostatic and the finite volume in MITgcm makes the model suitable for studying the mixing process and the dynamical interactions with steep topography ([1]; [3]). It has been employed successfully to many water bodies to model the circulation [17]. In all our simulations, the hydrostatic approximation is used because the horizontal resolution is much larger than the total water depth.

In the MITgcm model, U and V represent the eastward and northward velocities respectively. The values of U and V are identical both in the east and west boundaries because

the grid is periodic with N_x and N_y grid points in x and y directions for all variables, (e.g. $U_{N_x+1,j} = U_{1,j}$ for all j and $V_{i,N_y+1} = V_{i,1}$ for all i. Also the wind stress in x- and y-directions (eastward and northward) are applied at the U and V grid points respectively. That is, the northward wind stress applied at V grid point (i, j) is physically imposed at $x = (i - 0.5)\Delta x$ and $y = (j - 1)\Delta y$ while the eastward wind stress applied at U grid point (i, j) is physically imposed at $x = (i - 1)\Delta x$ and $y = (j - 0.5)\Delta y$ (see Figure 5.1).

Therefore, for a northward wind stress $Windy(x) = U_m x$, where x ranges from 0 to L_x on the western and eastern boundaries respectively and N_x cells in x direction is the wind stresses at $x = 0.5\Delta x$, $1.5\Delta x$,... $(N_x - 0.5)\Delta x$; for $i = 1$ to N_x. Thus, we have $Windy(x) = U_m(i + 0.5)\Delta x$ for $x = x_i$ and $i = 1, 1, 2, ..., N_x$ with $\Delta x = \frac{L_x}{N_x}$.

or

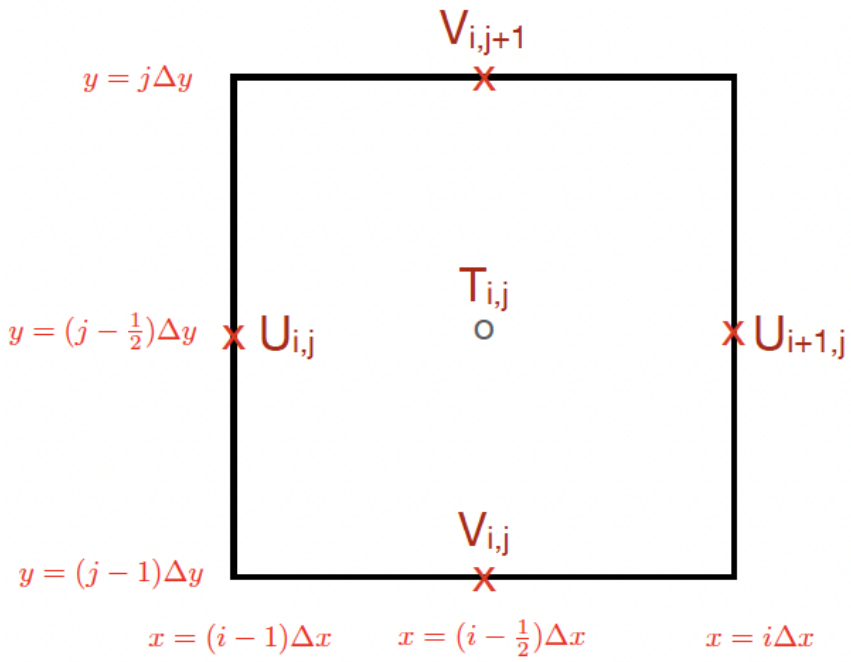

Figure 5.1: Schematic description of the horizontal grid structure, copied from Prof. K. G. Lamb's note

5.2 Idealized Lake Model Setup

A toy lake of length $L_x(km)$ in the x -direction, width L_y (km) in y direction, and depth z (m) was modeled using the MITgcm model. The model was forced with South-North linearly varying winds (m/s). The wind$x$, wind$y$, long wave and short wave downward radiations, air temperature, and air humidity are given every 3600 seconds. The lake emits long wave radiation and KPP mixing scheme is used for the horizontal diffusion and vertical mixing [17]. The end time for the simulation was 8.25 days. The horizontal (Δx and Δy) and vertical resolutions are 100 m and $\Delta z = 0.5$ m, respectively. We used 16 core processors and the duration for running each simulation was around 2 days.

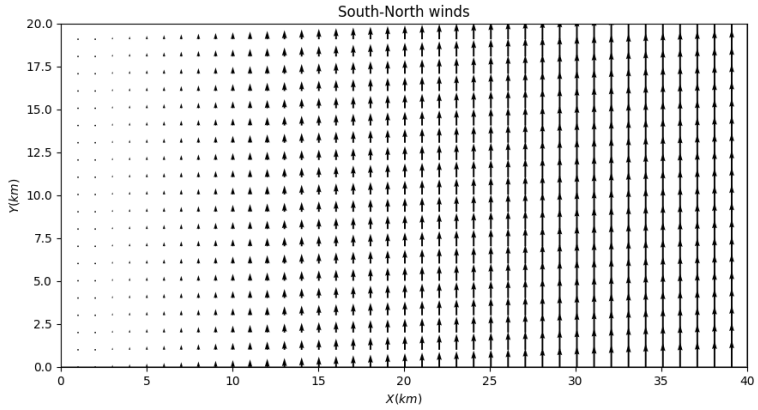

Figure 5.2: Snapshot of South-North winds acting on the lake with a maximum speed of $U_m = 4$ m/s

5.2.1 Wind Forcing for the Model (Idealized Lake)

$$Windy = U_m \frac{x}{L_x} \tag{5.1}$$

Equation (5.1) is implemented numerically as

$$Windy(i) = U_m(i + 0.5)\frac{\Delta x}{L_x} \tag{5.2}$$

where U_m is a multiplier with unit m/s, $x = (i+0.5) \times \Delta x$, $\Delta x = \frac{L_x}{N_x}$, and i goes from 0 to $N_x - 1$, x was replaced with $(i+0.5)$ as earlier explained in section 5.1, the northward wind stress, *windy* that was applied to the model and it varies from 0 at the western boundary to U_m at the eastern boundary.

Please note that in this model, the northward wind stress (in the y direction) was imposed at the V grid points (see 5.1).

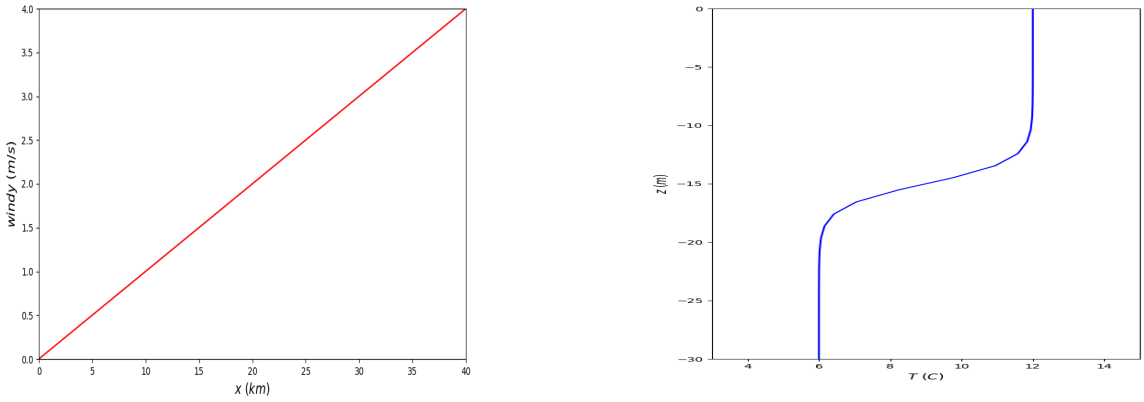

(a) (b)

Figure 5.3: (a) South-North Winds acting on the idealized lake, (5.3a) with $U_m = 4\ m/s$ and (b) Temperature profile with $T_s = 12\ ^oC$, $T_b = 6\ ^oC$, $z_0 = -15\ m$, and $d = 2\ m$.

Initial State

The initial temperature field is horizontally uniform and has a single thermocline separating two layers of constant temperatures. It is given as

$$T(z) = T_b + \frac{1}{2}(T_s - T_b)\left(1 + \tanh\left(\frac{(z - z_0)}{d}\right)\right) \tag{5.3}$$

Equation (5.3) is the temperature at height z, where T_b and T_s are the temperatures at the bottom and surface respectively, z_0 is the middle of the thermocline and d is the thickness of the thermocline (layer where the temperature changes rapidly).

5.3 Lake Erie Model Setup

For all our Lake Erie simulations, we used 500 m bathymetry with two open boundaries; the Detroit (where 80% of the lake's water flows in) and Niagara rivers [17]. The bathymetry was obtained from the Great Lakes Environmental Research Laboratory (GLERL). Smagorinsky parameterization and KPP mixing scheme were used for the horizontal diffusion and vertical mixing respectively. The atmospheric forcing varies across the lake spatially and temporally.

The surface forcing data were generated based on information from the meteorological buoys using an inverse distance weighting interpolation method by [16] following [17]. The models were initialized using temperature from four thermistor chains. For the 6 months of interest in 2008, there are noticeable variations in the values of the data for the different seasons: The long wave radiations varies between 210 $W\ m^{-2}$ to 400 $W\ m^{-2}$, short wave radiation varies between 80 $W\ m^{-2}$ and 900 $W\ m^{-2}$, air temperature between 1 ^oC and 30 ^oC, relative humidity between 0.1 and 1, wind speeds are mainly between $-15\ m\ s^{-1}$ and $+15\ m\ s^{-1}$ with the westerly (zonal) winds being the strongest; the zonal winds (uwinds or westerly winds) varies between $-14\ m\ s^{-1}$ and $+15\ m\ s^{-1}$ while the meridional winds (vwinds) varies between $-15\ m\ s^{-1}$ and $+14\ m\ s^{-1}$ (see Figure 5.5).

Hourly data is used to force the model. The forcings include wind speed and wind direction, surface air temperature, relative humidity, observed net longwave radiation and short wave radiation, and river inflows and outflows for accurate description of the circulation and thermal structures of Lake Erie ([5]; [17]). These meteorological data were obtained from the National Water Research Institute (NWRI) of Environment Canada (EC) and the National Data Buoy Center (NDBC) for year 2008 [17]. The forcing data were observed at four meteorological stations across Lake Erie; SBIO1 (South Bass Island 01) located in the western basin, EC341 stationed at between western and central basin, EC Stanley (Port Stanley) stationed at the central basin, and EC Colborne stationed in the eastern basin. (see Figure 5.4) [17].

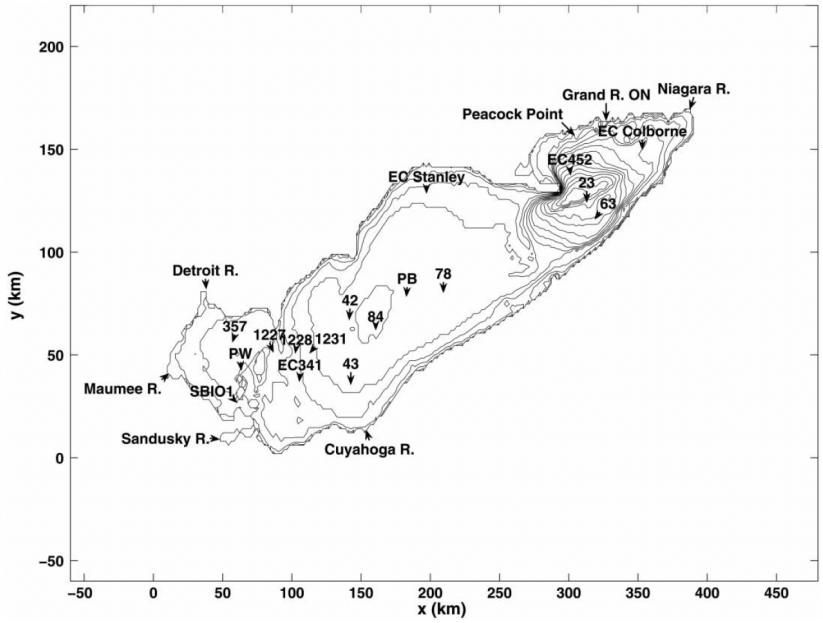

Figure 5.4: Bathymetry of Lake Erie showing the locations of the meteorological buoys, water temperature and ADCP moorings, and rivers in Lake Erie copied from [17].

The number of grid points in the x, y, and z directions are 784, 352, and 80, respectively and the vertical resolution, $\Delta z = 0.782\ m$. We used 256 core processors and the duration for running each simulation was about 2 days.

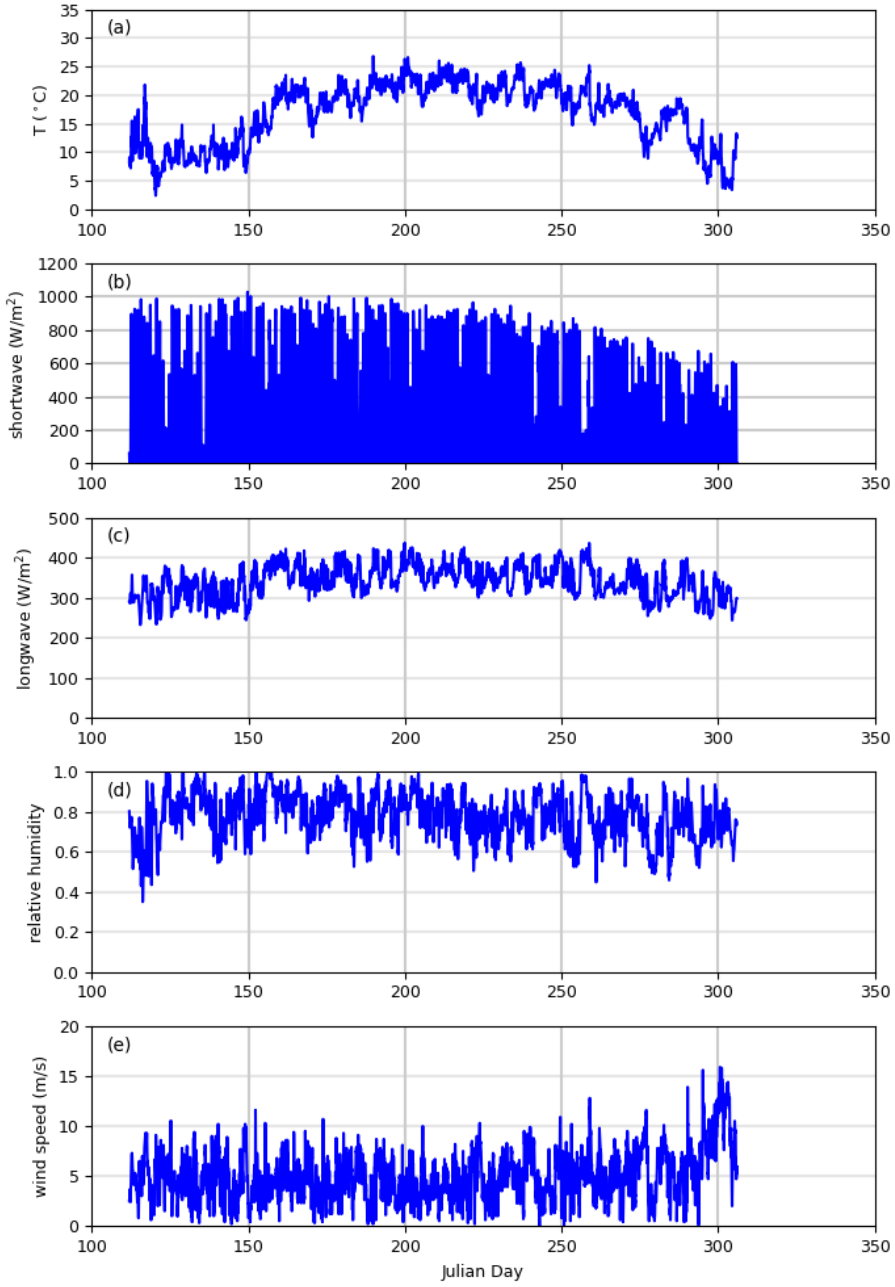

Figure 5.5: Observed forcing data from Station 341 (Central Basin) in Lake Erie: (a) Temperature; (b)Shortwave radiation; (c) Long wave radiation; (d) Relative humidity; and (e) Wind speed

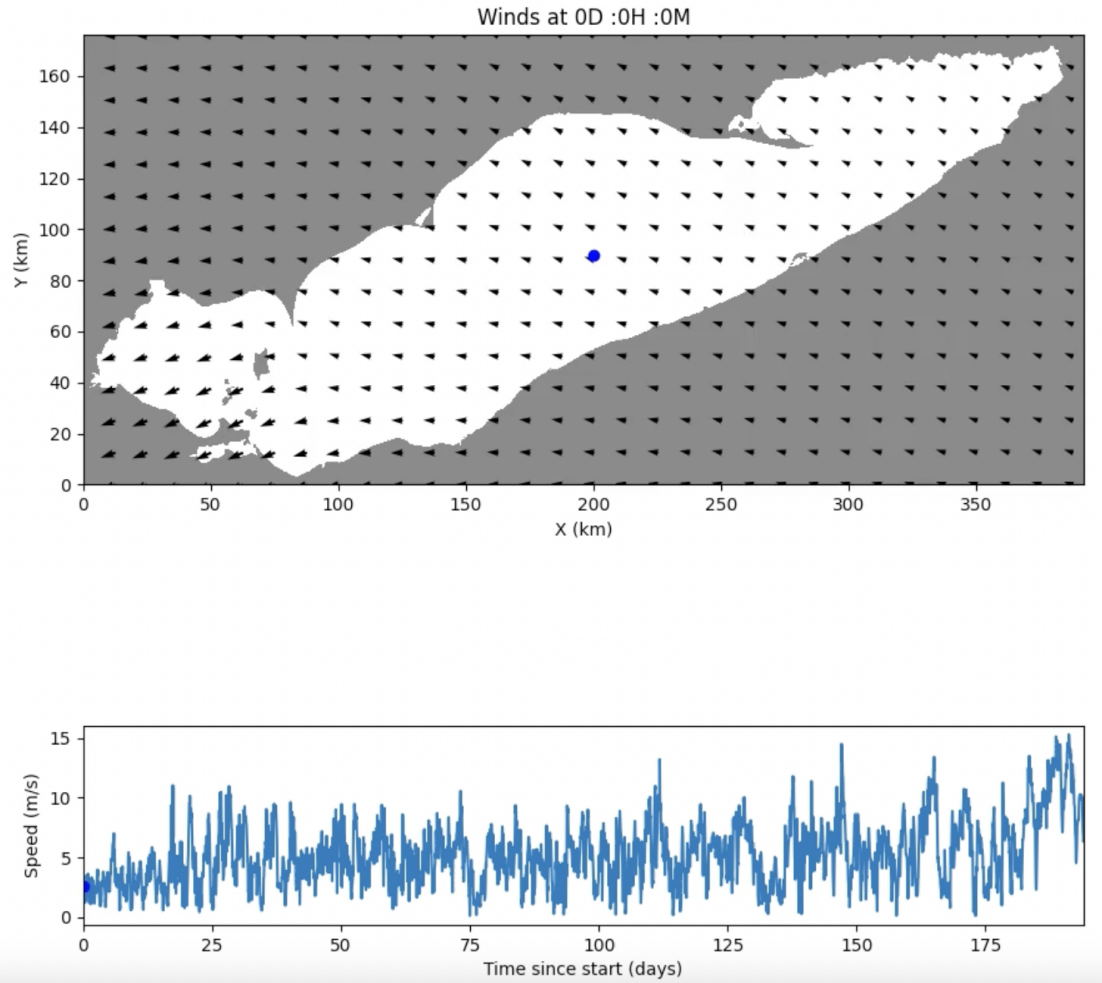

Figure 5.6: Top panel: Spatial plot of the initial wind field. Bottom panel shows the wind speed ($m\ s^{-1}$) at a point in the central basin indicated by a blue dot in the upper panel.

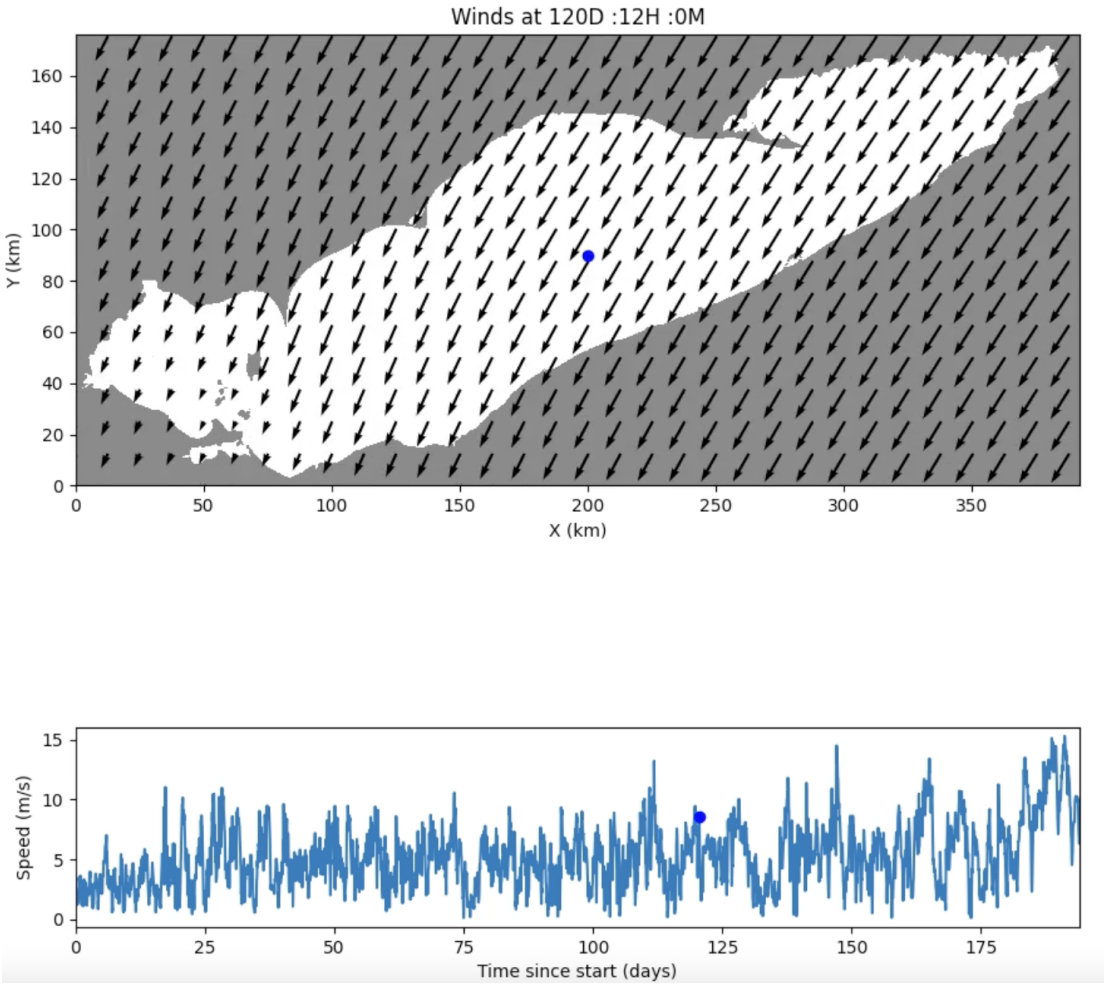

Figure 5.7: Same as Figure 5.6 but at time 120 days, 12 hours (120D:12H). This time is indicated by the blue dot in the lower panel.

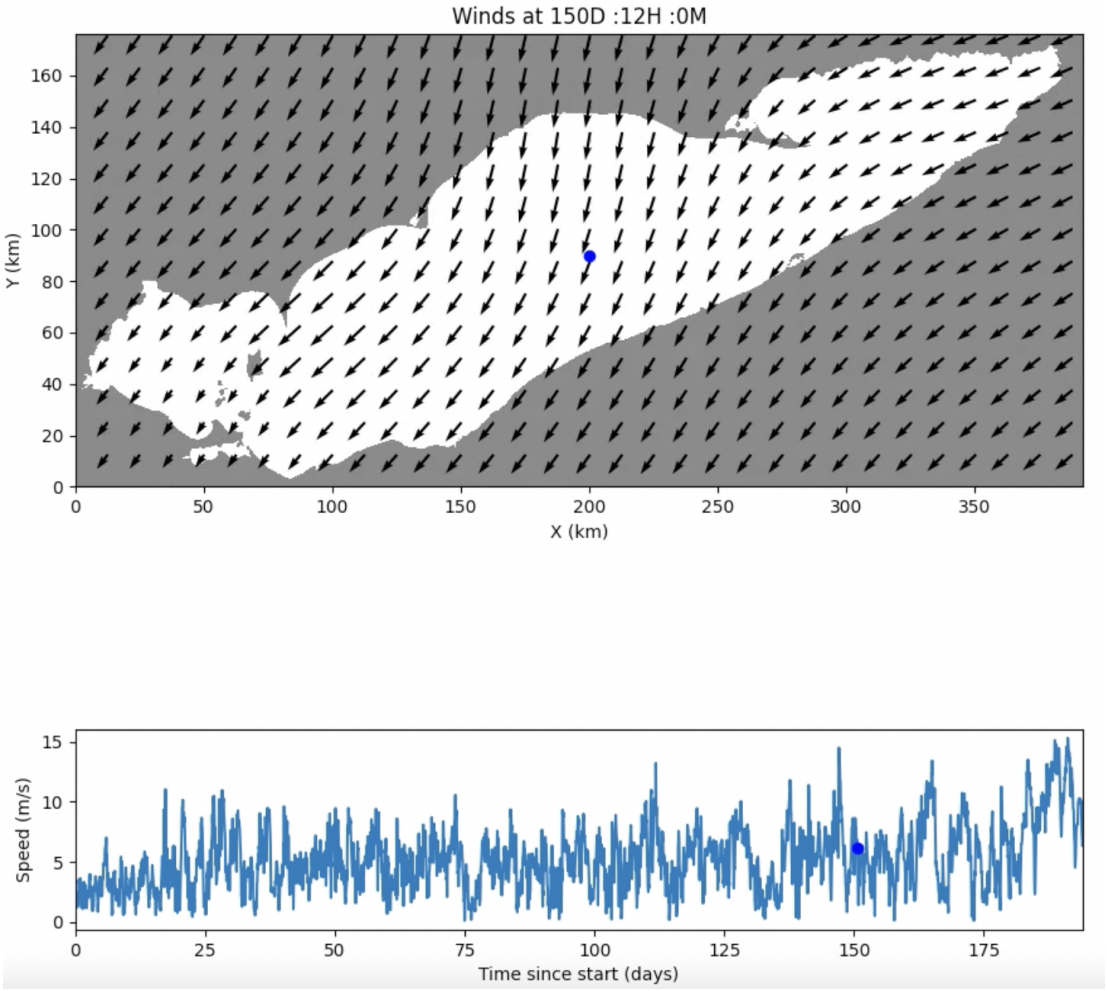

Figure 5.8: Same as Figure 5.6 but at time 150 days, 12 hours (150D:12H).

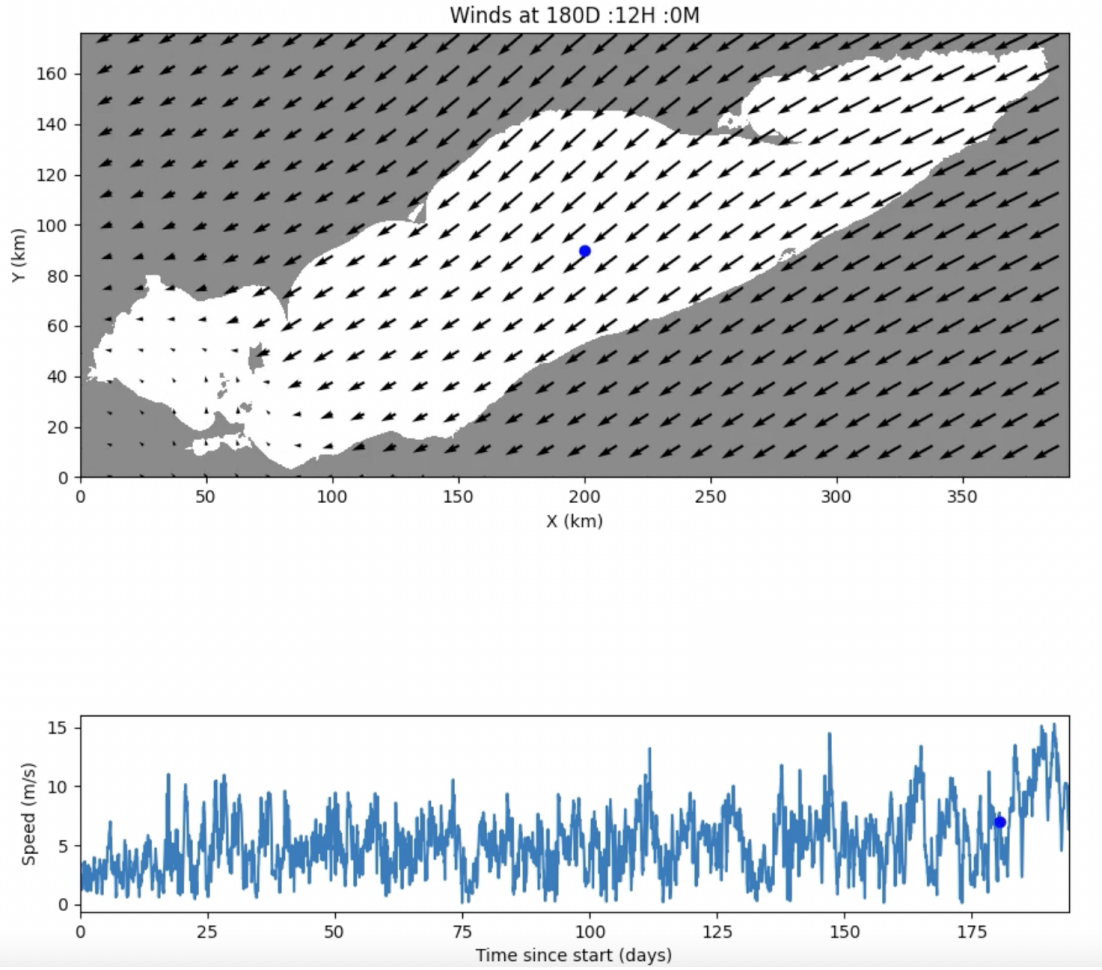

Figure 5.9: Same as Figure 5.6 but at time 180 days, 12 hours (180D:12H).

Chapter 6

Simulating Motion in Idealized Lake

Like other forces that drive physical processes in lakes, absorption of solar energy and its conversion as heat have huge effects on the thermal structure as well as the circulation patterns in lakes. This in return influences nutrient cycling, distribution of dissolved oxygen (DO) and biota, and adaptation of the aquatic organisms [39]. In this chapter we use the MITgcm to model a toy lake by varying some of the forcing parameters such as short wave and long wave radiation, air temperature, relative humidity etc., to study their effects on the Toy Lake. See chapter 5 for the model setup.

We also compare the model results against the estimated current in the upper layer in the toy lake using the expression derived earlier in chapter 4.

List of Cases	**Model employed/ Parameters**	**Expected Outcomes**
Base case	(i) 2-band model using Jerlov IA., (ii) 40 km by 20 km., and (iii) All the forcing parameters.	To provide data to compare the other cases to
Case 2	Same as the Base case but with the Coriolis force close to zero (i.e $9E-9$).	To see the effects of modeling a very small Coriolis force
Case 3	Same as the Base case but with (i) no short wave & long wave radiation and, and (ii) the Coriolis force is close to zero (i.e $9E-9$)	To see the effect of the absence of short wave & long wave radiation on the results
Case 4	Same as the Base case but with Jerlov IB	To know the effect of using Jerlov IB in the model
Case 5	Same as the Base case but with 3-band model	To know the effect of using 3-band model
Case 6	Same as the Base case but with (i) different lake size (20 km by 20 km) and, and (ii) thermocline thickness ($d = 2\ m$)	To see the effect of running the same model on a smaller lake with thinner thermocline
Case 7	Same as the Case 6 but with (i) no long wave and, and (ii) short wave radiation	To see the effect of the absence of long wave & short wave radiation on the small lake
Case 8	Same as the Case 6 but with no long wave radiation	To have an idea of what happens when we run a model without long wave radiation
Case 9	Same as the Case 6 but with no short wave radiation	To have an idea of what happens when we run a model without short wave radiation

Table 6.1: List of Cases, Setup Parameters, and Expected Outcomes for an Idealized Lake.

6.1 Base Case: Modeling the Toy Lake of Size 40km by 20km with all the Forcing Parameters

For the Base Case, the Toy Lake of length $L_x = 40\ km$ in x -direction, width $L_y = 20\ km$ in y direction, and depth $H = 30\ m$ was modeled using the hydrodynamic MITgcm 2-band model for Jerlov water type 2 (IA). The model was forced with South-North linearly varying winds (see (5.1)), U_m of 4 m/s speed. T_b, T_s, z_0 and d in (5.3b) are set to be 12 ^oC, 6 ^oC, $-15\ m$, and 10 m respectively. Long wave and short wave radiation, relative humidity, and air temperature are (6.1), (6.2), (6.3), and (6.4), respectively:

$$\text{lw} = 410 + 30 \sin\left(\frac{2\pi(t+3)}{24}\right) \tag{6.1}$$

$$\text{sw} = \begin{cases} 750\ W\ m^{-2} \sin\left(\frac{2\pi t}{24}\right) & \text{if } t < 12\ h\text{: t=0 depicts sunrise} \\ 0 & \text{if } t \geq 12\ h\text{: t=12 depicts sunset.} \end{cases} \tag{6.2}$$

$$\text{RelHum} = 0.8 + \sin\left(\frac{2\pi(t+15)}{24}\right) \tag{6.3}$$

$$\text{airtemp} = 273.15 + 24 + \sin\left(\frac{2\pi(t+3)}{24}\right) \tag{6.4}$$

The start and end times for the simulation were 0 and 8.25 days.

The results of modeling the Toy Lake using the MITgcm model (Base Case) are represented in Figures 6.1 to 6.5. Figures 6.1 and 6.2 show the horizontal surface currents in the x and y directions respectively after 8 days. Clearly from Figures 6.1 and 6.2 the horizontal current is counterclockwise; that is, the water flows eastward along the southern boundary, north along the eastern boundary, west along the northern boundary and back south along the western boundary of the Toy Lake. This is in agreement with [5]'s observation, that due to the effects of rotation, the curl of the wind stress and that of the surface flow have the same sign in the northern hemisphere.

Figure 6.3 shows slices of the temperature at middle of the thermocline (see 5.3b) taken at different times. As can be observed from figure 6.3, cyclonically propagating Kevin waves

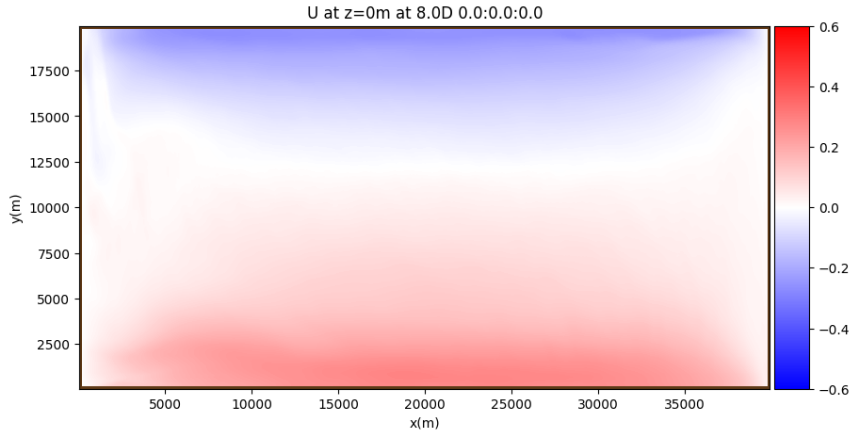

Figure 6.1: Base case: Horizontal current in the x-direction at the surface taken at time 8.0D: 0.0: 0.0: 0.0 (8 days, 0 hour, 0 minute, 0 second). The color bar represents values of currents in m/s

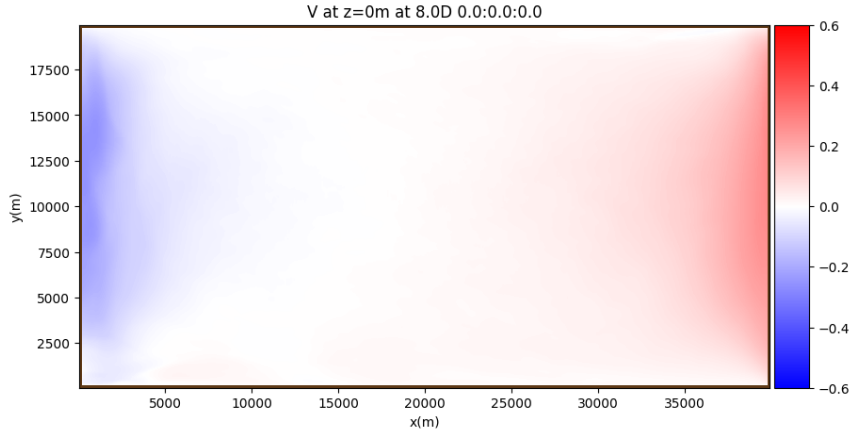

Figure 6.2: Base case: Same as Figure 6.1 but in the y-direction.

were noticed along the northern boundary right after 12 h (0.5 day).

Figure 6.4 shows a vertical slice of the temperature field at $y = 10$ km while Figure 6.5 is the corresponding horizontal currents in y directions. In Figure 6.4, a dome shaped thermocline was revealed, this is not surprising since the wind stress curl is cyclonic resulting in Ekman transport divergence in the upper layer and a positive vertical current in the middle of the domain resulted in a dome shaped thermocline (i.e., it is raised in the centre

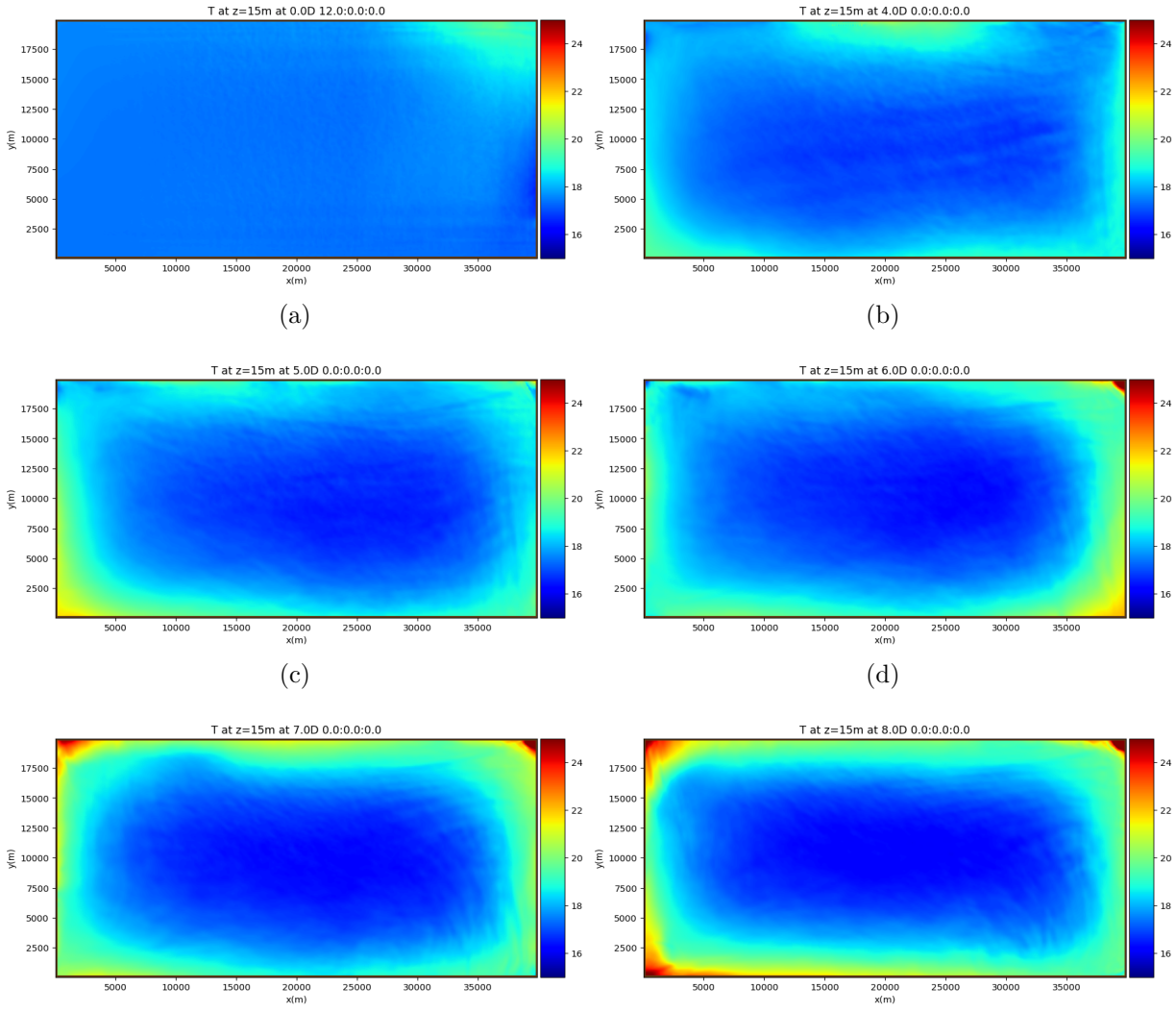

Figure 6.3: Base case: Snapshots of the temperature at 15 m depth (the middle of the thermocline; see Figure 5.3b) taken at (a) 0.5 day; (b) 4 days; (c) 5 days; (d) 6 days; (e) 7 days; and (f) 8 days. The color bar represents values of temperature in ^oC

of the lake) (see Figure 6.4).

Figure 6.5 shows that the counterclockwise circulation in the y direction (i.e. negative val-

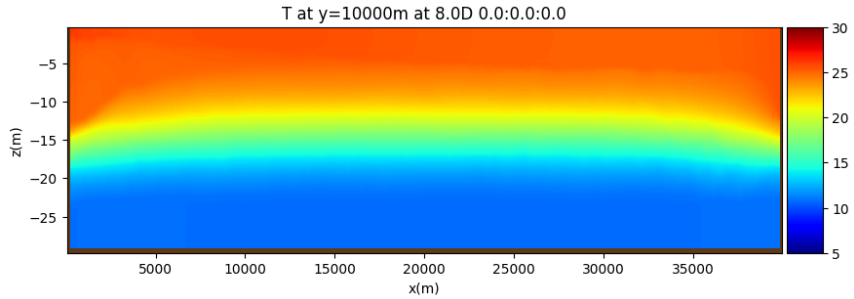

Figure 6.4: Base case: Snapshot of the temperature field at y= 10 km taken at t=8 days. The color bar represents values of temperatures in ^oC

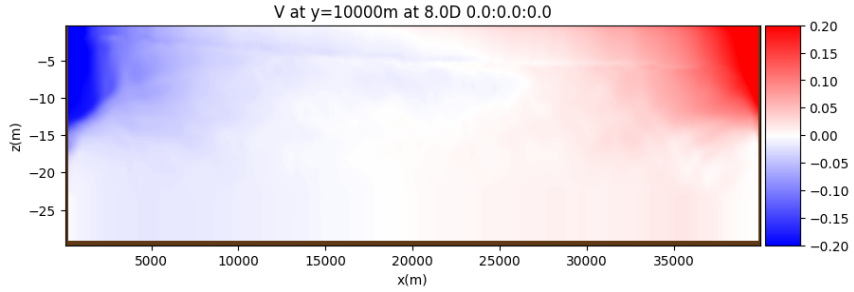

Figure 6.5: Base case: Horizontal current in the y-direction at y = 10 km taken at 8 days, 0 hour, 0 minute, and 0 second (8.0D: 0.0: 0.0: 0.0). The panel bar represents values of currents in m/s

ues along the eastern boundary and positive along the western boundary) is confined to the upper layer. The absence of currents in the lower layer implies a horizontally uniformly pressure. Similar behaviors were observed for the slices of the temperature field and the horizontal currents at $y = 2.5\ km$ $y = 5\ km$, $y = 10\ km$, $x = 5.5\ km$, and $x = 30\ km$ (not shown).

Comparing Simulated and Analytical Results

Here we compare the results from the hydrodynamic MITgcm model (Base Case) with the analytical results. For the analytical results, we assume that the fluid is motionless at the bottom (i.e. the pressure in the bottom layer is horizontally uniform). Then the following expressions hold:

$$\eta_x(x) = -\frac{\Delta\rho}{\rho_s}\zeta_x(x) \tag{6.5}$$

$$\zeta_x(x) = -\frac{\Delta z}{\Delta x} \tag{6.6}$$

$$v_s(x) = -\frac{g}{f}\frac{\Delta\rho}{\rho_s}\zeta_x(x) \tag{6.7}$$

here we have followed (4.36), (4.34), and the fact that the ζ_x is the slope of the interface to define (6.5), (6.7), and (6.6) with $\eta(x)$ and $\zeta(x)$ as the free surface and the interface respectively, $\eta_x(x)$ is the slope at the free surface, ρ_s and ρ_b are the densities in the upper and lower layer, $\Delta\rho$ is the difference between the densities, $v_s(x)$ is the current in the upper layer, f is the Coriolis force, and g is the gravitational acceleration.

From figure 6.4, we estimate $\Delta z = (-12.5 + 15)m = 2.5\ m$, $\Delta x = 2500\ m$, thus, using these values in equation (6.6), we have the value of the slope of the interface as $\zeta_x \approx 10^{-3}$.

Using $\Delta\rho = 1.7\ kg\ m^{-3}$, $\rho_s = 998\ kg\ m^{-3}$, $\rho_b = 999.7\ kg\ m^{-3}$, and $\zeta_x = 10^{-3}$ in equation (6.5), we have $\eta_x = -1.7034 \times 10^{-6}$.

Plugging $f = 10^{-4}\ s^{-1}$, $g = 10\ m/s^2$ and $\eta_x(x) = -1.7034 \times 10^{-6}$ in (6.7), we have the current in the upper layer, as $u_s = -0.1703\ m/s$.

Based on figure 6.5, the simulated values for the current is between $\pm 0.2\ m/s$, which is relatively close in value to what we arrived at analytically. Thus, we can confidently infer that the MITgcm model's prediction is accurate.

6.1.1 Case 2: Base Case with a Coriolis Force Close to Zero

This is very similar to the Base Case but modeled with a Coriolis parameter close to zero (i.e $9E-9$). Figures 6.6 and 6.7 show the slice of the stratification and horizontal current, respectively for the Case 2 taken at 8 days. Patterns are similar to what was observed in

the Base Case except that the upper mixed layer in the Base Case is thicker than that in Case 2 and the thermocline is no longer dome-shaped as observed in the Base Case which is expected due to the almost zero Coriolis force (see figure 6.4).

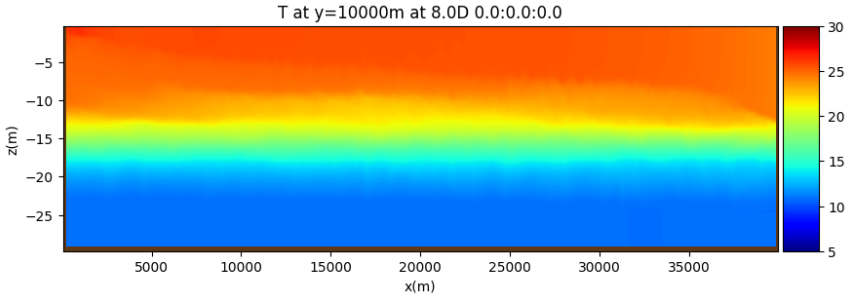

Figure 6.6: Case 2: Snapshot of the temperature at y= 10 km taken at at time 8 days, 0 hour, 0 minute, and 0 second (8.0D: 0.0: 0.0: 0.0). The color bar represents values of temperature in ^oC

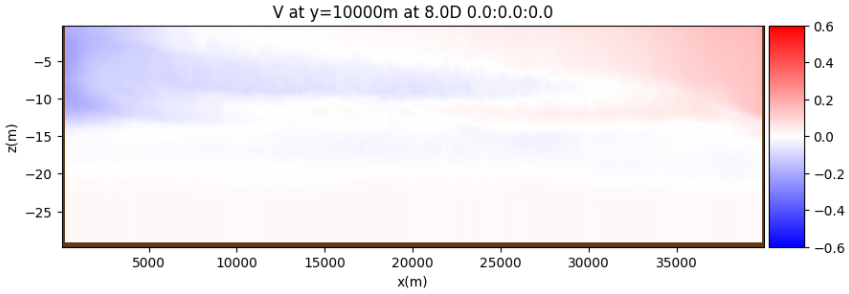

Figure 6.7: Case 2: Horizontal current in the y-direction at y = 10 km at 8 days, 0 hour, 0 minute, and 0 second (8.0D: 0.0: 0.0: 0.0). The color bar represents values of current in m/s

6.1.2 Case 3: Base Case with no Long Wave and Short wave Radiation

Case 3 is also similar to the Base Case but with no long wave and short wave radiations and the Coriolis force is close to zero (i.e $9E-9$). Figures 6.8 and 6.9 represent the modeled thermal stratification and horizontal current taken at 8 days respectively. Figure

6.9 revealed an counterclockwise circulation in the x and y direction i.e. it shows negative values along the eastern boundary and positive along the western boundary which is the with our observation with the Base Case. Even though we simulated the two cases (Base Case and Case 3) with the same thermocline thickness, ($d = 10\ m$), temperatures at the surface, ($T_s = 12\ ^oC$) and at the bottom ($T_b = 6\ ^oC$), the water is warmer at the surface in the Base Case (modeled with both long wave and short wave radiation and the Coriolis parameter) with observed water temperature of about 25 ^oC at the surface while that in Case 3 where the observed temperature is approximately 12.5 ^oC, this is understandable given the lack of additional heating from the solar radiation (short wave and long wave radiation) (see figures in Case 3, 6.4 and 6.8).

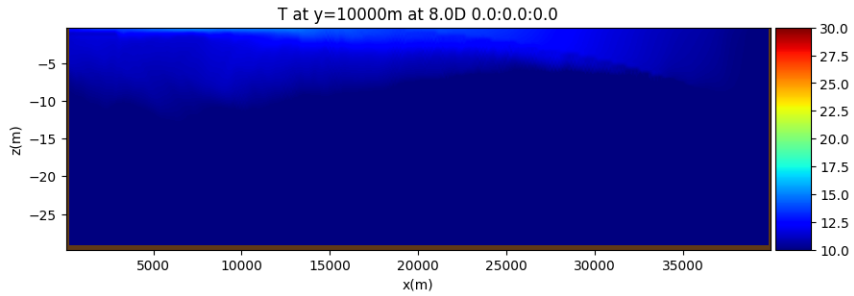

Figure 6.8: Case 3: Snapshot of the temperature field at y= 10 km taken at t=8 days. The color bar represents values of temperature in ^oC

6.1.3 Using the 2-band Model Jerlov IB (Case 4) and a 3-band Model (Case 5)

For **Case 4**, the Toy Lake was modeled with the 2-band model Jerlov IB instead of Jerlov 1A using the values for the fractions of the insolation resident from [17] provided in Table 3.2. All other parameters used in the Base Case are unchanged.

For **Case 5**, the 3-band model was used with the values for the fractions of the insolation resident and the extinction length scales from [17] provided in Table 3.1. All other parameters specified in Base Case remain the same here as well.

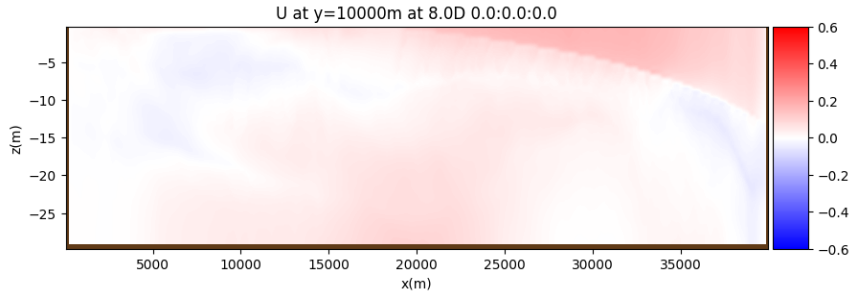

(a)

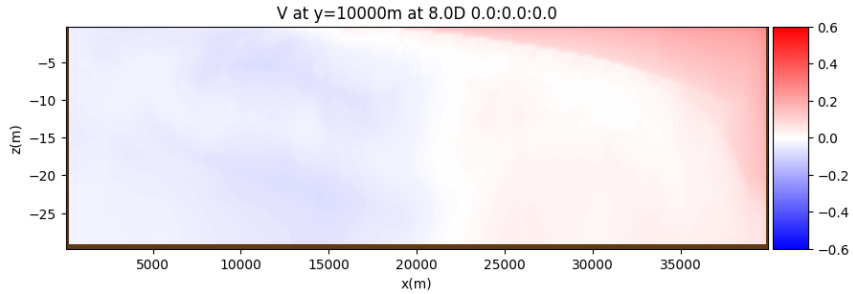

(b)

Figure 6.9: Case 3: Horizontal current in the x-direction (a) and y-direction (b) at y = 10 km taken at t=8 days. The color bar represents values of current in m/s

Comparing the Results from the Base Case, Case 4 and Case 5

Similar to the observations by [17], as a result of the difference in the extinction length scales in the 2-band (Jerlov IA and IB) and 3-band model, the incoming shortwave radiation penetrates deeper into the water column in the Base Case and Case 4 (2-band model Jerlov IA and IB) than in Case 5 (3-band model) i.e. Case 5 produced warmer upper mixed layer (top 5 m) with surface temperature of about 25 ^oC than the results in the Base Case and Case 4 with the surface temperatures of about 18 ^oC, this is in line with [17]'s findings (see Figure 6.10). The water temperature in the hypolimnion is also slightly colder in Case 5 than in the Base Case since a larger amount of energy is being absorbed near the surface. In addition, all the three cases (Base Case, Case 4, and Case 5) produce a consistent dome-shaped thermocline across the length of the Toy Lake with a characteristic anticlockwise circulation (i.e. negative values along the eastern boundary and positive values along the western boundary), these are evident in Figures 6.10 and 6.11.

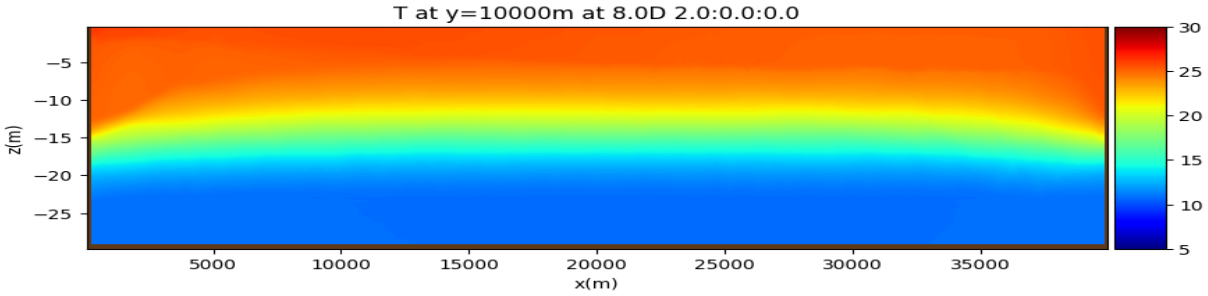

(a)

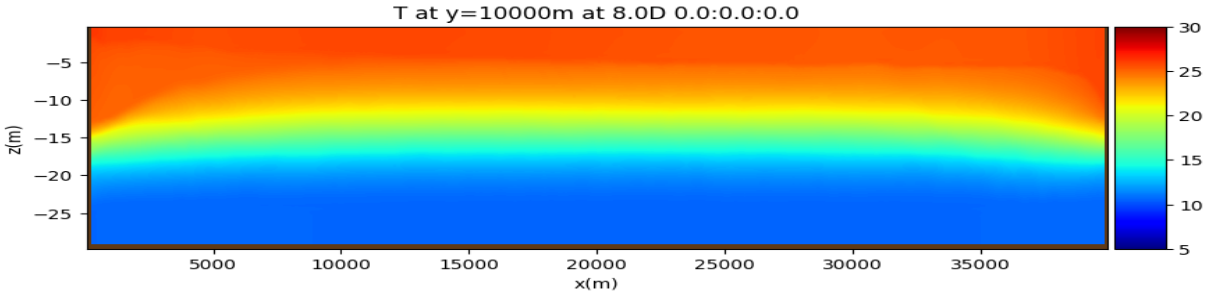

(b)

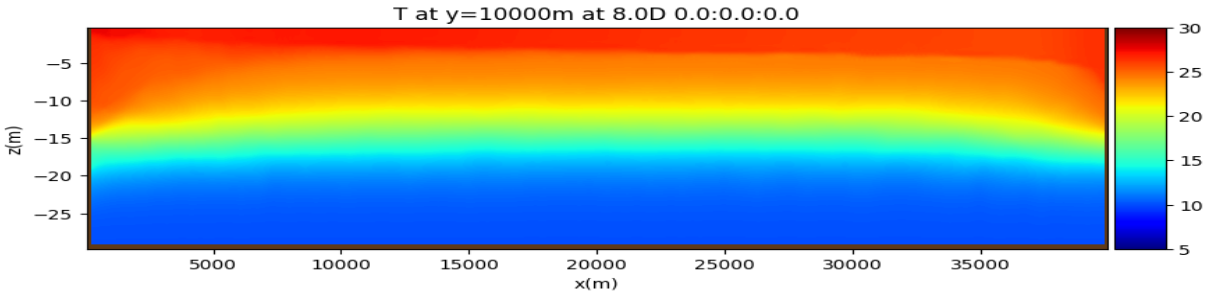

(c)

Figure 6.10: Snapshots of the temperature field at y= 10 km for the (a) Base Case, (b) Case 4, and (c) Case 5. The color bar represents values of temperature in ^oC

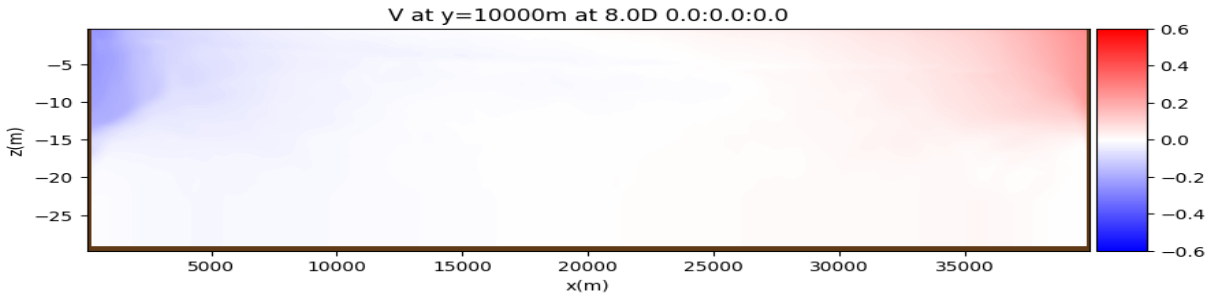

(a)

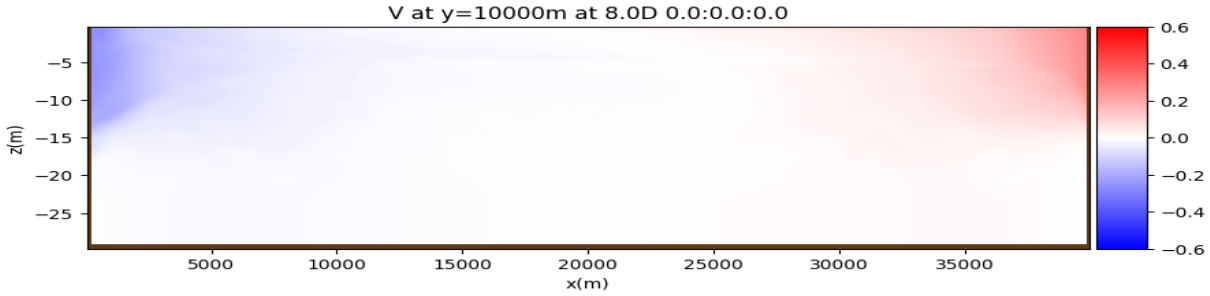

(b)

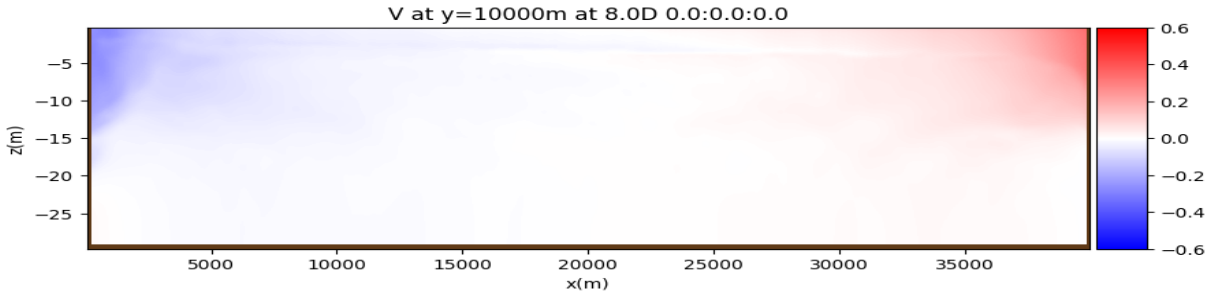

(c)

Figure 6.11: Snapshots of the horizontal currents in the y-direction at y= 10 km for (a) Base Case (b) Case 4, and (b) Case 5, taken at 8 days. The color bar represents values of current in m/s

6.2 Modeling the Toy Lake of Size 20km by 20km While Varying Some of the Forcing Parameters

1. **Case 6**: This case is identical to the Base Case except that $L_x = 20\ km$ instead of 40 km, the thermocline thickness is $d = 2\ m$ instead of 10 m, and the water depth is

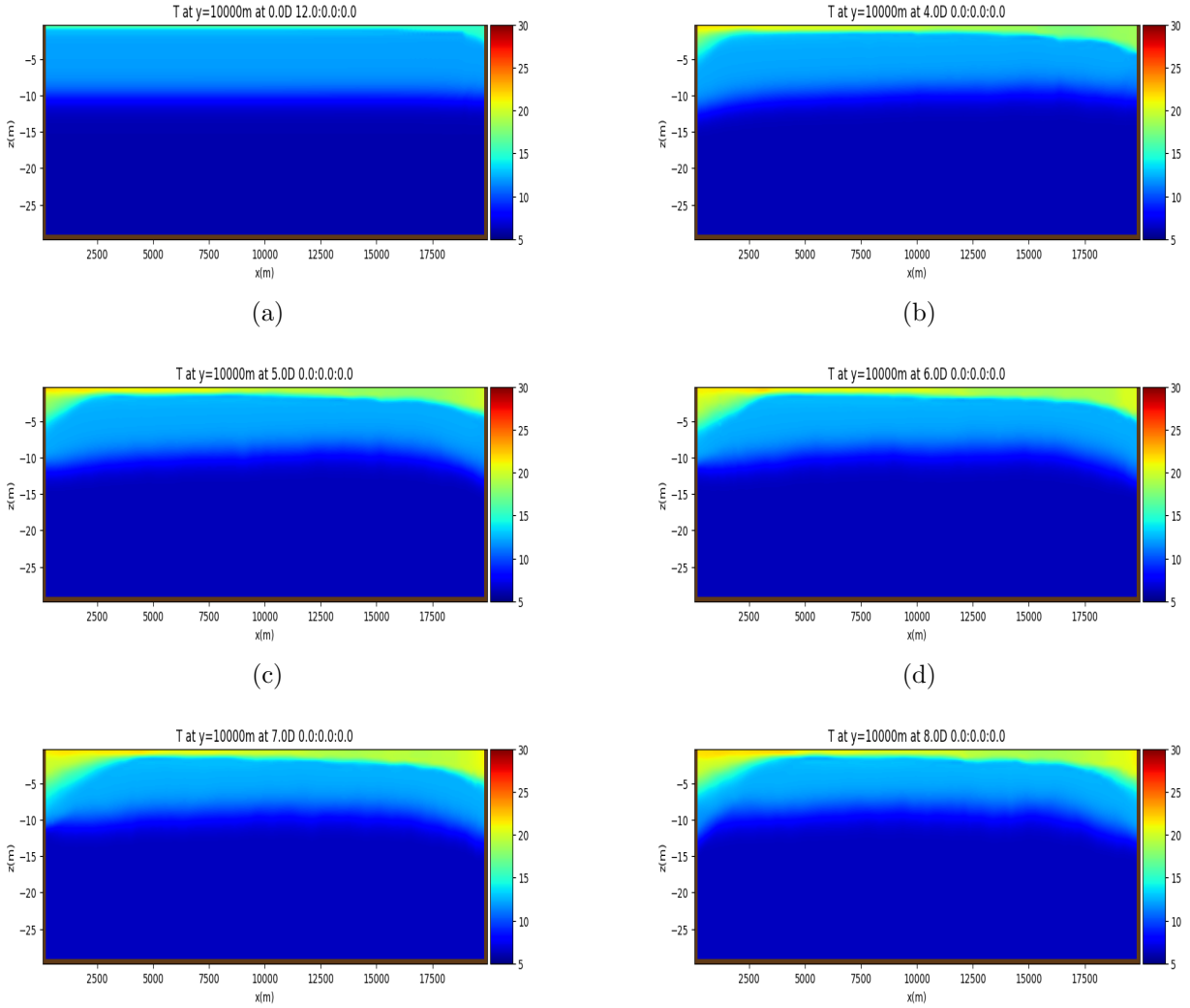

(a) (b) (c) (d) (e) (f)

Figure 6.12: Case 6: Snapshots of the temperature at y= 10 km taken at (a) 0.5 day; (b) 4 days; (c) 5 days; (d) 6 days; (e) 7 days; and (f) 8 days; modeled using all the forcing parameters. The color bar represents values of temperature in ^oC

doubled to $H = 60\ m$.

2. **Case 7**: Same as Case 6 but with no short wave radiation and no long wave radiations

3. **Case 8**: Same as Case 6 but with no long wave radiation

4. **Case 9**: Same as Case 6 but with no short wave radiation

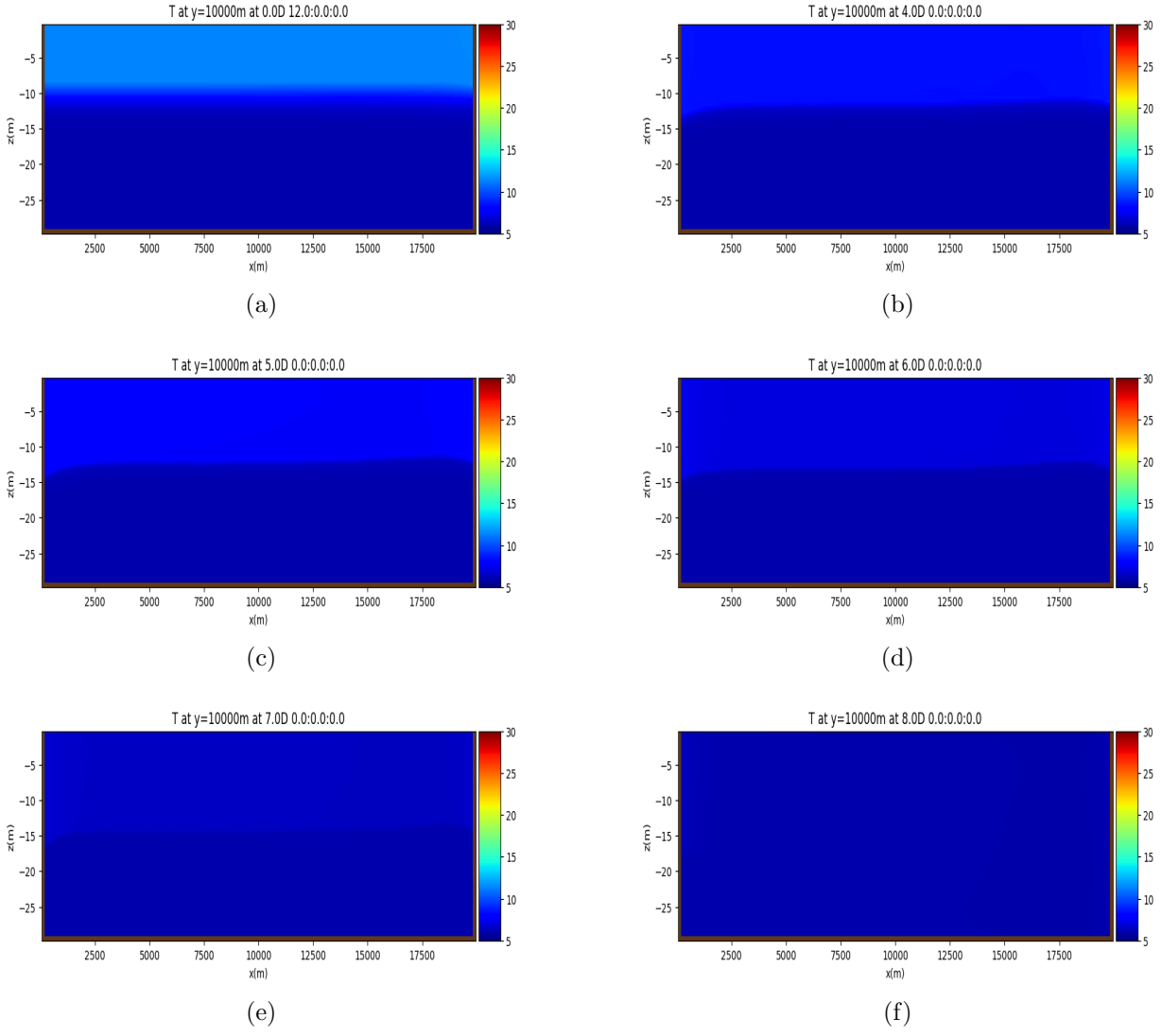

(a) (b) (c) (d) (e) (f)

Figure 6.13: Case 7: Same as Figure 6.12 but modeled with no long wave and no short wave radiation.

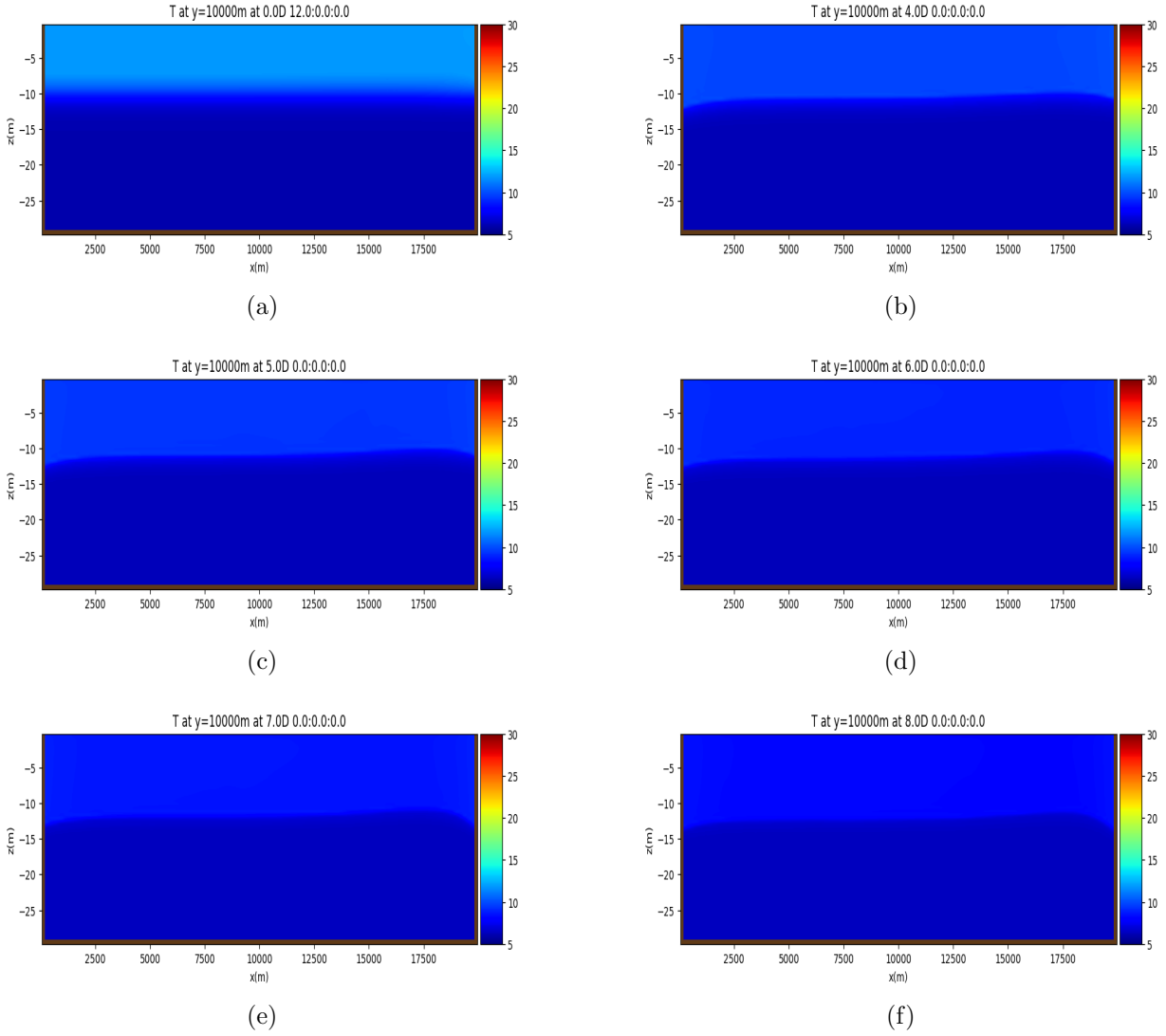

Figure 6.14: Case 8: Same as Figure 6.12 but modeled with no long wave radiation.

Figures 6.12, 6.13, 6.14, and 6.15 show the snapshots of the temperature field at $y = 10\ km$ taken at between $t = 0.5$ and $t = 8$ days when the Toy Lake was modeled with all the forcing parameters, without both the shortwave and longwave radiation, with no long wave radiation, and with no shortwave, respectively. In these figures, as expected, the characteristics dome-shaped thermoclines were observed with counterclockwise circulation patterns

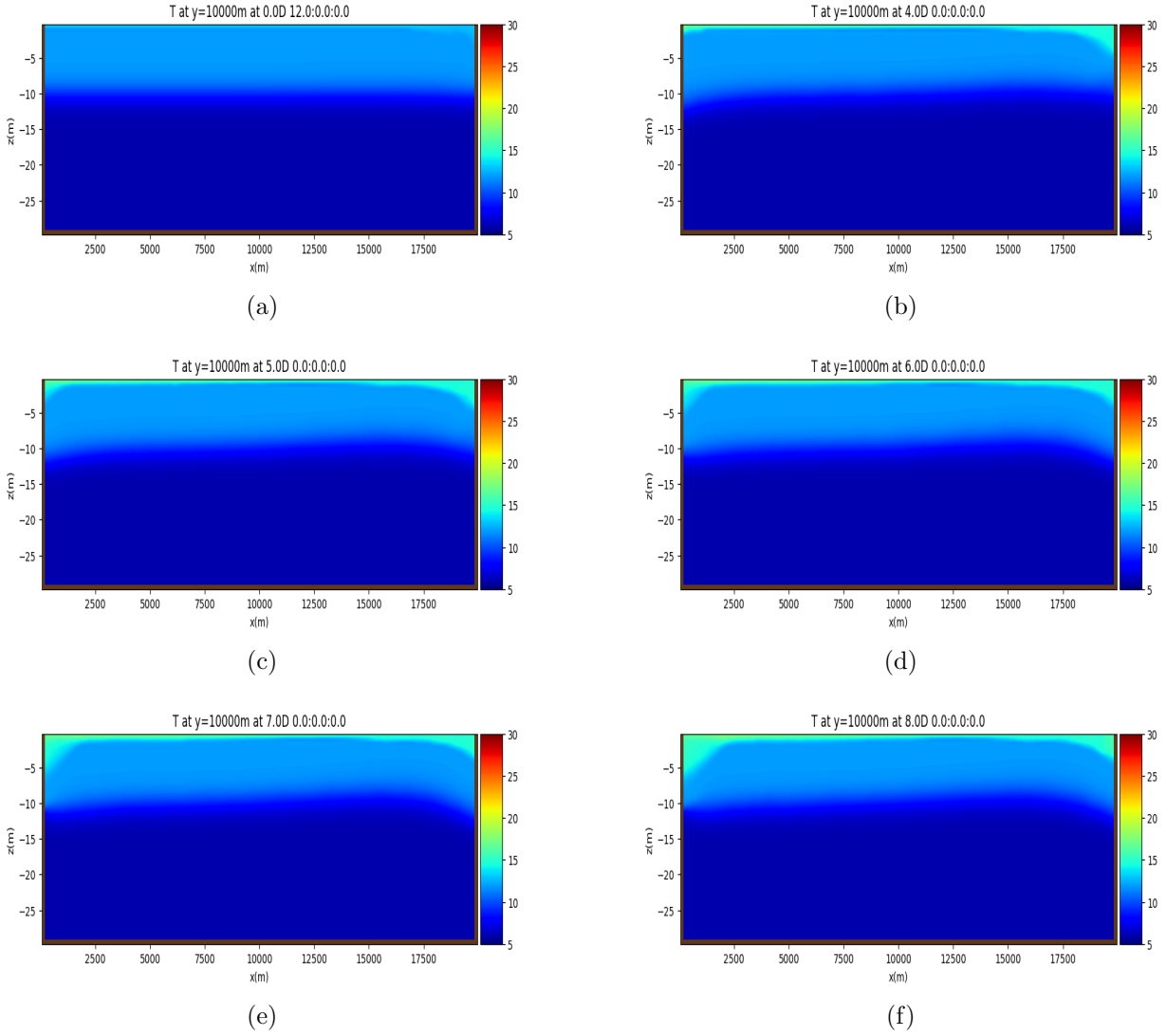

Figure 6.15: Case 9: Same as Figure 6.12 but modeled with no shortwave radiation.

which is similar to the observation with the Toy Lake of length $L_x = 40\ km$ in x direction, width $L_y = 20\ km$; we chose not to display the images for the currents here as they were all similar to what we had in our Base case model.

Observations from Figures 6.13 and 6.14, it is quite obvious that the water in the Toy

Lake cools down faster in the case without both the shortwave and longwave radiation than the case without longwave radiation as expected since amount of energy entering the lake in Case 7 is less than that in Case 8, which basically explain our result. Also when the shortwave radiation was set to zero with (6.1) as the long wave radiation, water cools down quickly, faster than what we observed when the Toy Lake was modeled with all the forcing parameters as shown in Figure 6.12.

Chapter 7

Simulating Motion in Lake Erie

In this chapter, we use the MITgcm to model Lake Erie on a 500 m horizontal grid with a uniform 0.782 m resolution in the vertical to study its summer circulation and the thermal structure. We explore the two common 2-band short wave parameterizations, Jerlov water types IA and III, and also a 3-band paramerization using values from [17] (see Tables 3.2 and 3.1). We then compare the results from the different cases at several locations in Lake Erie.

List of Cases	Model employed/ Parameters	Expected Outcomes
Base Case	(i) 2-band model using Jerlov IA, and (ii) All the forcing parameters.	To have data to validate the results from the other runs
Case 2	Everything in the Base Case except the Jerlov water type changed from IA to III	To see the effects of running the model with different Jerlov water types
Case 3	(i) 3-band model with, and (ii) all the parameters used in the Base Case	To see the effect of running the model with a 3-band model
Case 4	(i) Everything in the Base Case, and (ii) with increased air temperature	To know what happens when the temperature is increased
Case 5	(i) Everything in the Base Case, and (ii) with reduced air temperature	To know the effect of decreasing the air temperature
Case 6	(i) Everything in the Base Case, and (ii) with increased the temperature of the water inflow from the Detroit River	To see what happens when we increase the temperature of the inflow

Table 7.1: List of Cases, Setup Parameters, and Expected Outcomes.

7.1 Base Case

For the Base Case, Lake Erie was modeled using the hydrodynamic MITgcm 2-band model, Jerlov water type IA (see 3.2) which is the default short wave radiation model.

Figure 7.1 shows vertical slice of the modeled temperature field on a cross-section of the central basin at six different times. At the beginning of the simulation (22$^{\text{nd}}$ April 2008), the water in the lake is well mixed with temperature of about 10 ^{o}C everywhere in the central basin. By the 30$^{\text{th}}$ day of our simulation (Julian Day (JD) 142) which translates to the 22$^{\text{nd}}$ of May 2008, the water in the lake is weakly stratified with temperatures of

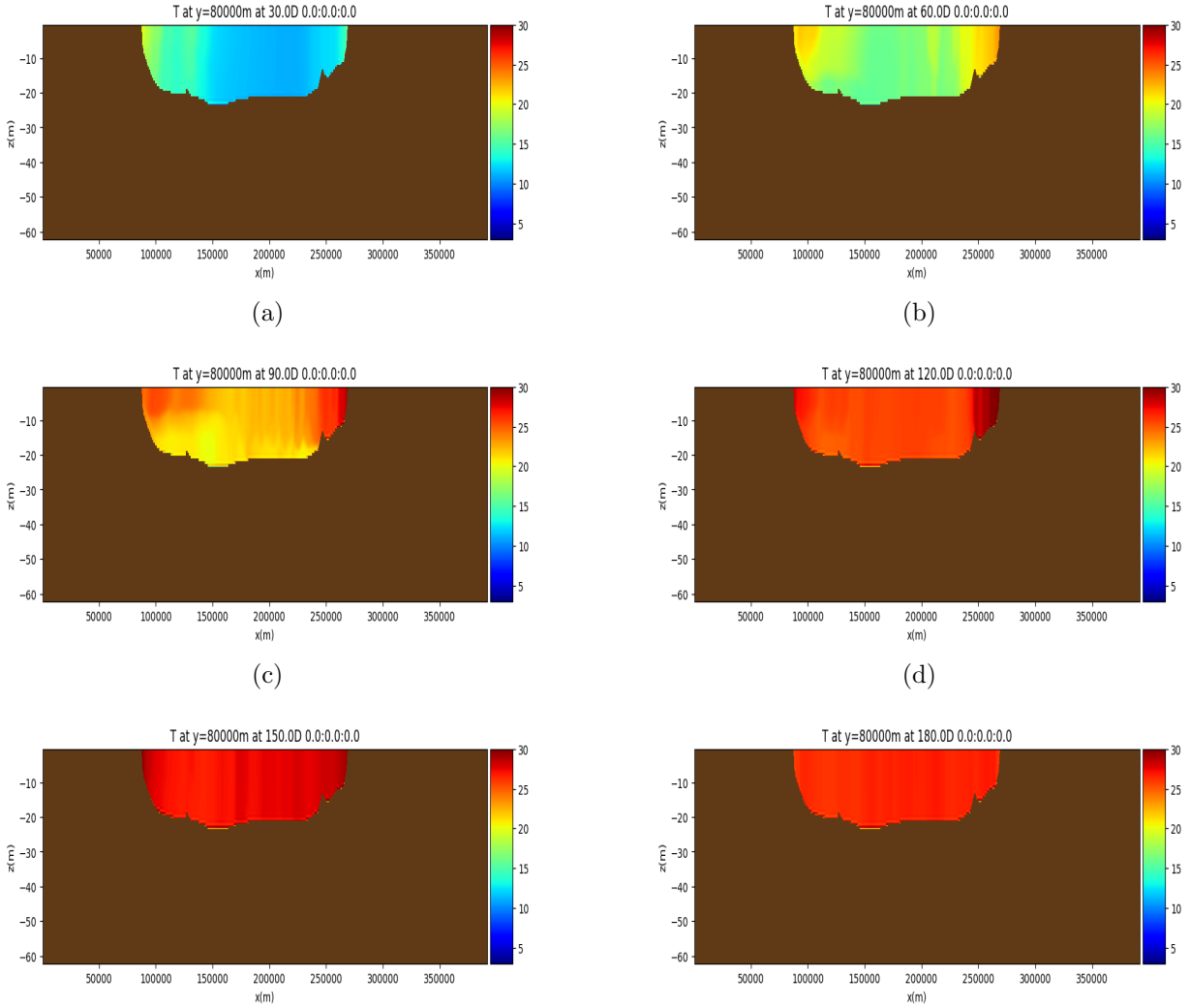

(a) (b) (c) (d) (e) (f)

Figure 7.1: Base Case: Snapshots of the temperature profiles at $y = 80\ km$ taken at every 30 days starting from 30 to 180 days, with (a), (b), (c), (d), (e), and (f) representing 30 days, 60 days, 90 days, 120 days, 150 days, and 180 days, respectively; modeled with all the forcing data. The color bar represents values of temperature in ^oC.

approximately 20 ^oC in the western end of the central basin, 15 ^oC and 12 ^oC in the shallow and deep part of the central basin respectively, while the shallow and deep part of the

eastern basin are 14 ^oC and 8 ^oC, respectively. By the 60th day (Julian Day 172; 21st June 2008), the water is warmer and the stratification becomes more pronounced with maximum temperature of 21 ^oC in the western basin being the warmest. After the 90th day (Julian Day 202; 21st July 2008), the water in the lake warms up completely with temperature varying between 22 ^oC to 30 ^oC across the lake and well defined upper mixed layer of 15 m depth. As the heating intensifies, the water temperature increases across the lake through days 120 (Julian Day 232) and 180 (Julian Day 292), and the mixed layer intersects the bottom layer by the 120th day (20th August 2008), then the water in the lake begins cooling down as a result of the change in weather (e.g. decreased air temperature, see figure 5.5).

Figure 7.2 shows the temperature along a North-South slice in the middle of the central basin. At the end of the first 30 days (JD 142; 22nd May 2008), the water in the shallow northern areas warms up to a temperatures of about 15 ^oC leaving the deeper water slightly colder with temperatures of approximately 12 ^oC. Further, at 60th day (JD 172; 21st June 2008) the shallow northern part is very warm relative to the other parts with minimum temperatures of about 15 ^oC. As expected by day 90 (21st July 2008), the shallow part of the central basin is very warm, the temperatures of the water in the deeper part of the central basin is uniform with about 20 ^oC. By day 120 (JD 202; 20th August 2008), the water in the lake is uniformly mixed as a result of the increased wind speed with an average temperatures 25 ^oC, continues to day 180 (JD 292; 19th October 2008) (see Figure 7.2).

Figure (7.3) shows vertical slice of the temperature field on an east-west cross-section of the eastern basin. As can be observed from Figure (7.3a), the water in the lake is well mixed at the beginning of the simulation (JD 112; 22nd April 2008), with temperatures around 6 ^oC. By the end of the first 30 days (JD 142; 22nd May 2008), the water in this part of the lake becomes weakly stratified. As the heating intensifies in the summer period, the water warms up quickly (see figure 7.3d) and is fully stratified at 90 days (JD 202; 21st July 2008) with an average temperature of 23 ^oC at the epilimnion and 15 ^oC in the bottom layer (about 8 ^oC difference) and the mixed layer grows to about 30 m. In the early fall on day 150 (JD 262; 19th September 2008) the difference between the temperatures in the epilimnion and the hypolimnion of the eastern basin has reduced to 4 ^oC with 27 ^oC and 23 ^oC at the surface and bottom layers, respectively. The stratification has almost disappeared by the 180th day (JD 292; 19th October 2008).

For **Case 2**, we modeled Lake Erie using the 2-band model with Jerlov III. The main difference between Jerlov III and IA shortwave parameterizations is their extinction lengths; Jerlov IA has longer extinction length than III (extinction length scales for Jerlov III and

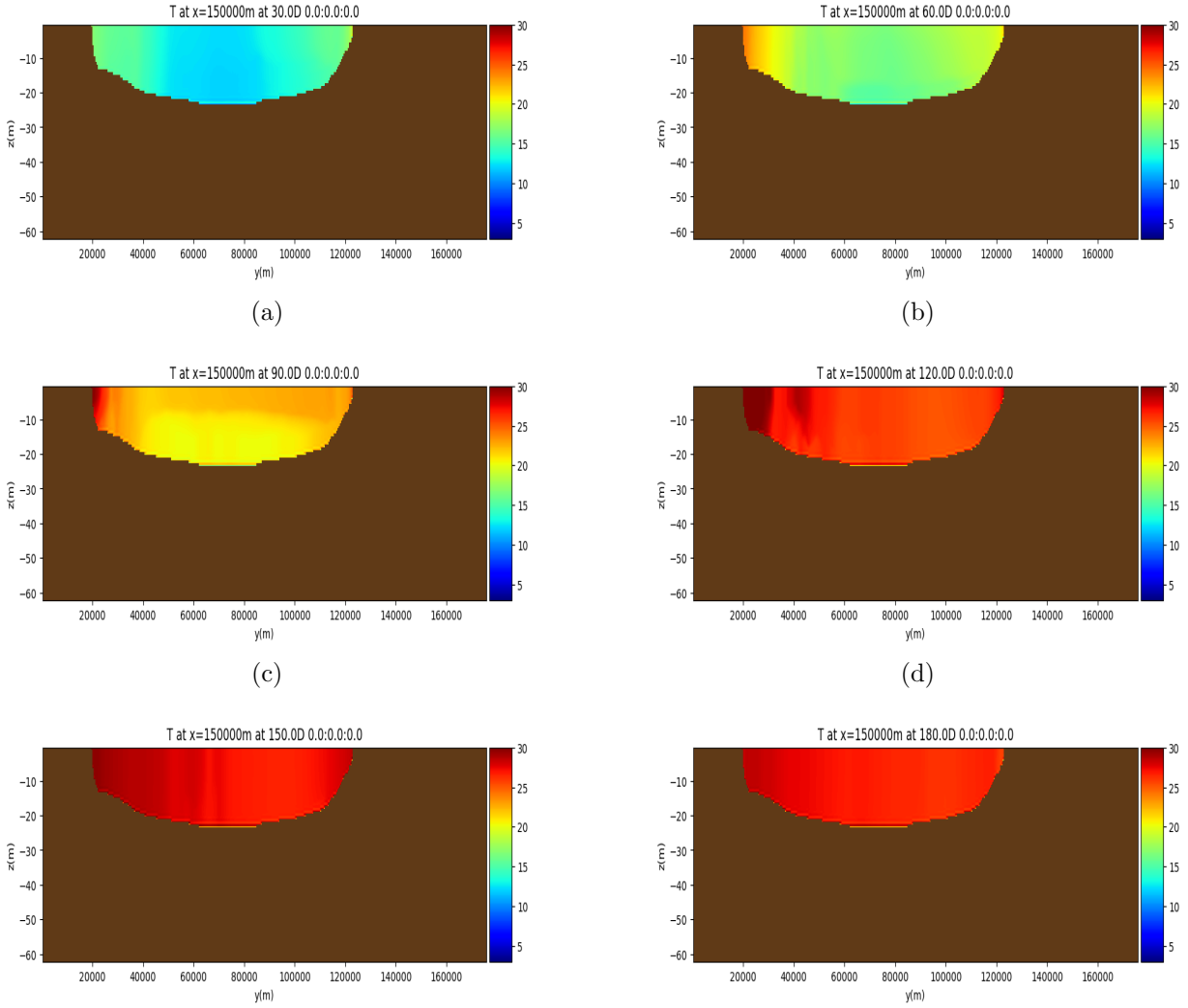

(a) (b) (c) (d) (e) (f)

Figure 7.2: Base Case: Same as Figure 7.1 but at $x = 150\ km$.

IA are 9.3 m and 20.98 m respectively, see Table 3.2), this makes it penetrates deeper into the water column than Jerlov III. The results show similar patterns (not shown) to our observations in the Base Case. Detailed comparison will be discussed later in this chapter.

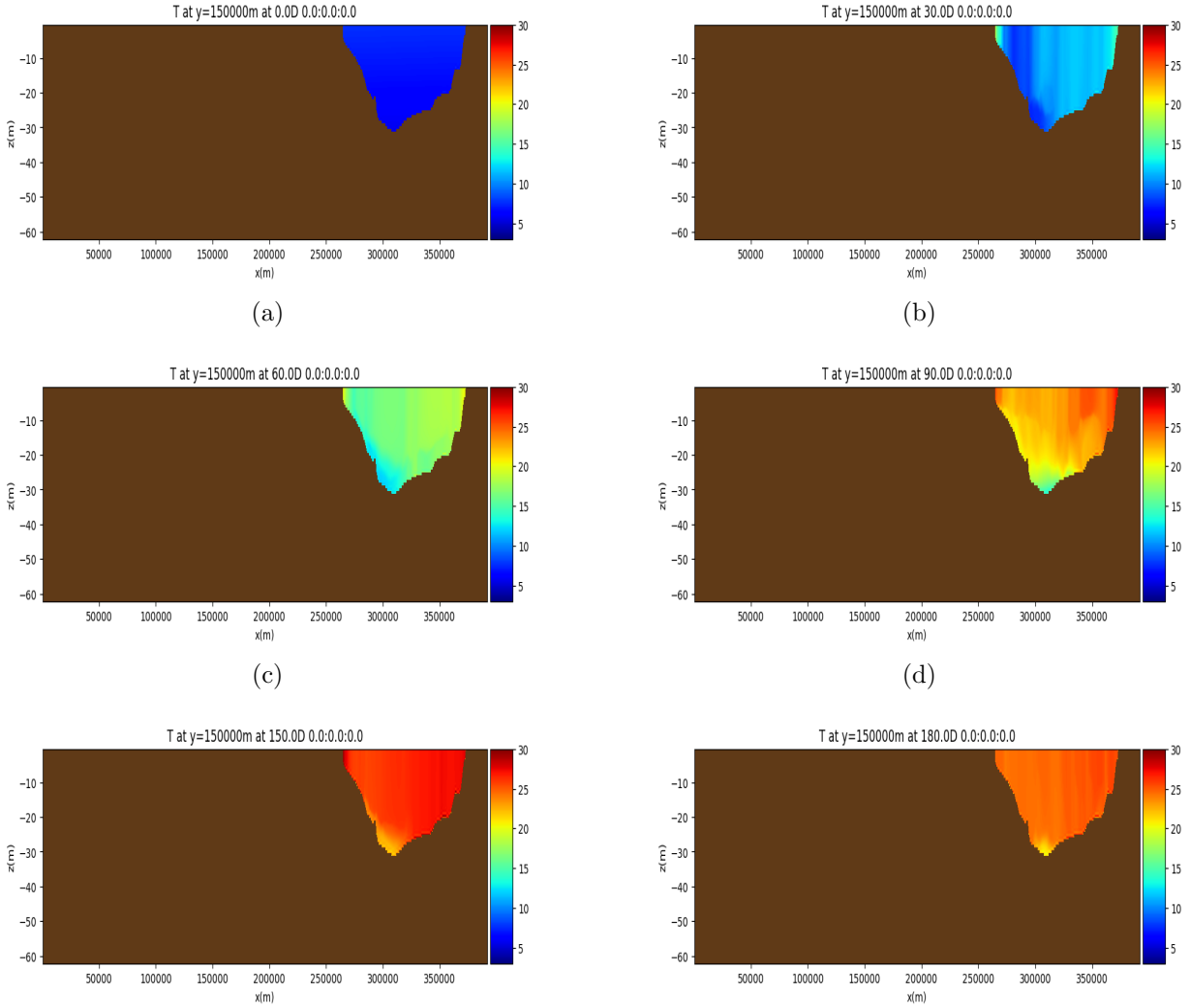

(a) (b) (c) (d) (e) (f)

Figure 7.3: Base Case: Same as Figure 7.1 but at $y = 150\ km$.

7.2 Case 3: 3-band Radiation Model

For Case 3, shortwave radiation was modeled using a 3-band model (see 3.2). In 3-band shortwave model, more energy is absorbed near the surface, which is the major difference with the 2-band shortwave radiation model. Similar to Figure 7.1, Figure 7.4 shows ver-

tical slices of the temperature field on a cross-section of the central basin at six different times. On the 30^{th} day of our simulation (JD 142; 22^{nd} of May 2008), similar to the Base Case, the water in this part of the lake is weakly stratified however, temperatures are lower than what we observed in the Base Case and the areas with cold water in Case 3 are smaller than in the Base Case (image not shown). A striking difference in Case 3 at day 30 (JD 142) is the thin layer of cold water at the bottom which is absent in the Base Case (see Figures 7.1a, 7.4a). At the 60^{th} day (21^{st} June 2008), the water is warmer and the stratification becomes more pronounced. This is also similar to the observation in the Base Case but the water temperatures are higher and larger portion of warm water here. At the 90^{th} day (21^{st} July 2008), similar to the Base Case, the water temperature in the WB is almost uniform (image not shown), however, water is warmer for the 3-band model than it is with the 2-band Jerlov IA (Base Case) and has better defined upper mixed layer of 22 m depth (thicker than that of the Base Case for the same period). As the heating intensifies, the water temperature increases across the lake through days 120 and 150. By the 120^{th} day (20^{th} August 2008), the water in the WB and the shallow part of the CB becomes very warm, warmer than what we saw in the Base Case (see Figures 7.1d and 7.4d). By the 150^{th} day (19^{th} September 2008), the water in the lake is completely mixed with temperature of over 30 ^oC (warmer than that in the Base Case for the same period) and the upper mixed layer intersects the bottom layer. By the 180^{th} day (19^{th} October 2008), the lake begins cooling down as a result of the change in weather (e.g. increased air temperature, see Figure 5.5), (see Figure 7.4).

Figure (7.5), similar to Figure (7.3) shows a vertical slice of the temperature field along a cross-section of the eastern basin. By the end of the first 30 days (22^{nd} May 2008), similar to the observation with the Base Case, the water in this part of the lake is weakly stratified, however, the hypolimnion is better defined at this period in Case 3 compared to the Base Case (see Figures 7.3b and 7.4a). Again, the water in the lake becomes well stratified by the 60^{th} day (21^{st} June 2008) this comes 30 days earlier than in the Base Case (see Figures 7.3c and 7.5c). As the heating intensifies, the thermocline becomes more pronounced by the end of the 90^{th} days (21^{st} July 2008) and the water temperature in the hypolimnion increased to about 8 ^oC, but still cooler than our observation with the Base Case (see Figures 7.3d and 7.5d). Further, by the 150^{th} day (19^{th} September 2008), the upper mixed layer grows to about 28 m. As expected, by the 180^{th} day (19^{th} October 2008), the depth of the hypolimnion is above 5 m which is thicker than in the Base Case even at day 150 (see Figures 7.5f, 7.3f, and 7.3e). Another noteworthy observation is that the thermocline does not intersect the bottom at the last day of our model (19^{th} October 2008) which is completely different from the observation with the Base Case.

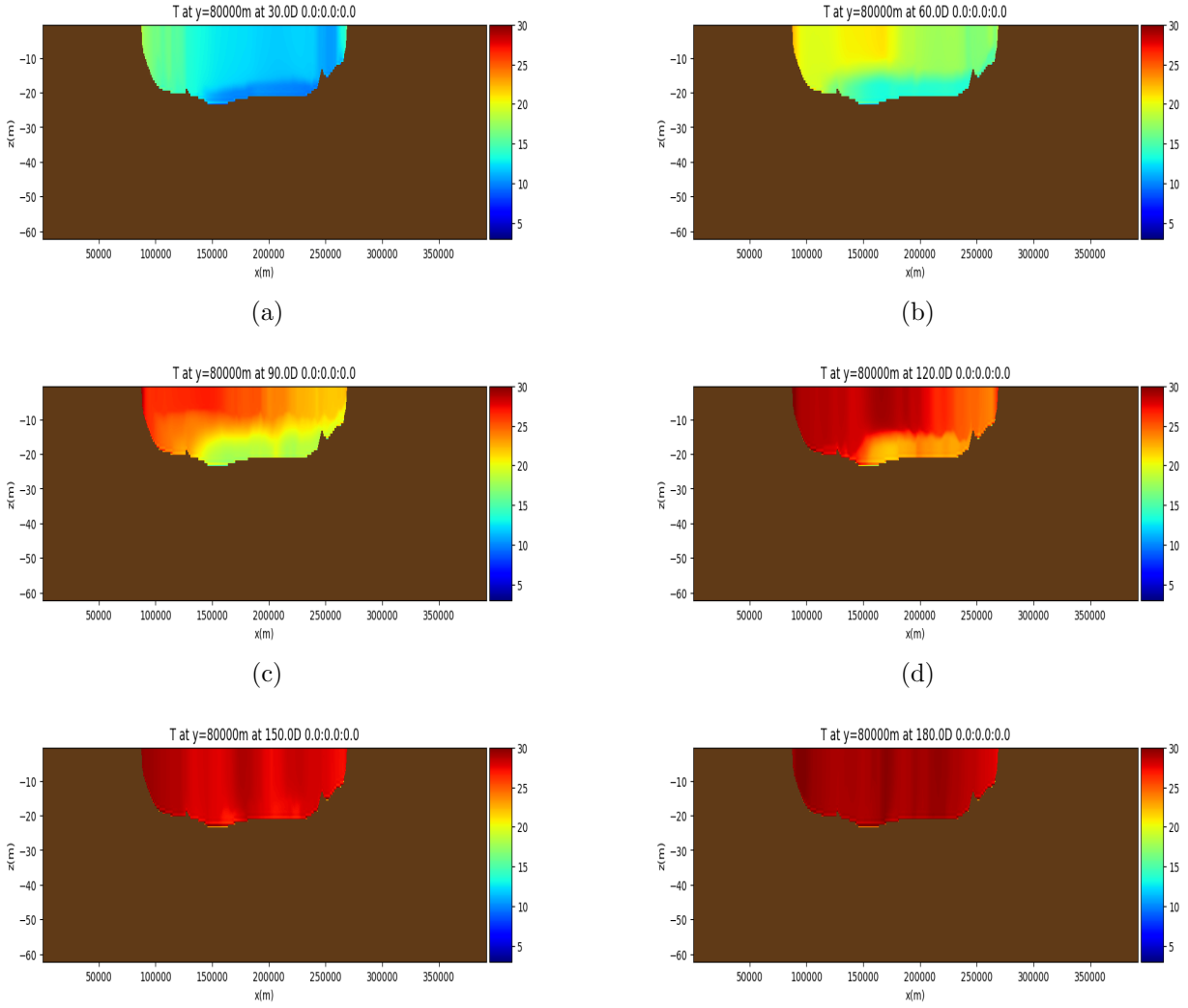

(a) (b) (c) (d) (e) (f)

Figure 7.4: Case 3: Similar to Figure 7.1 but for the 3-band short wave radiation model.

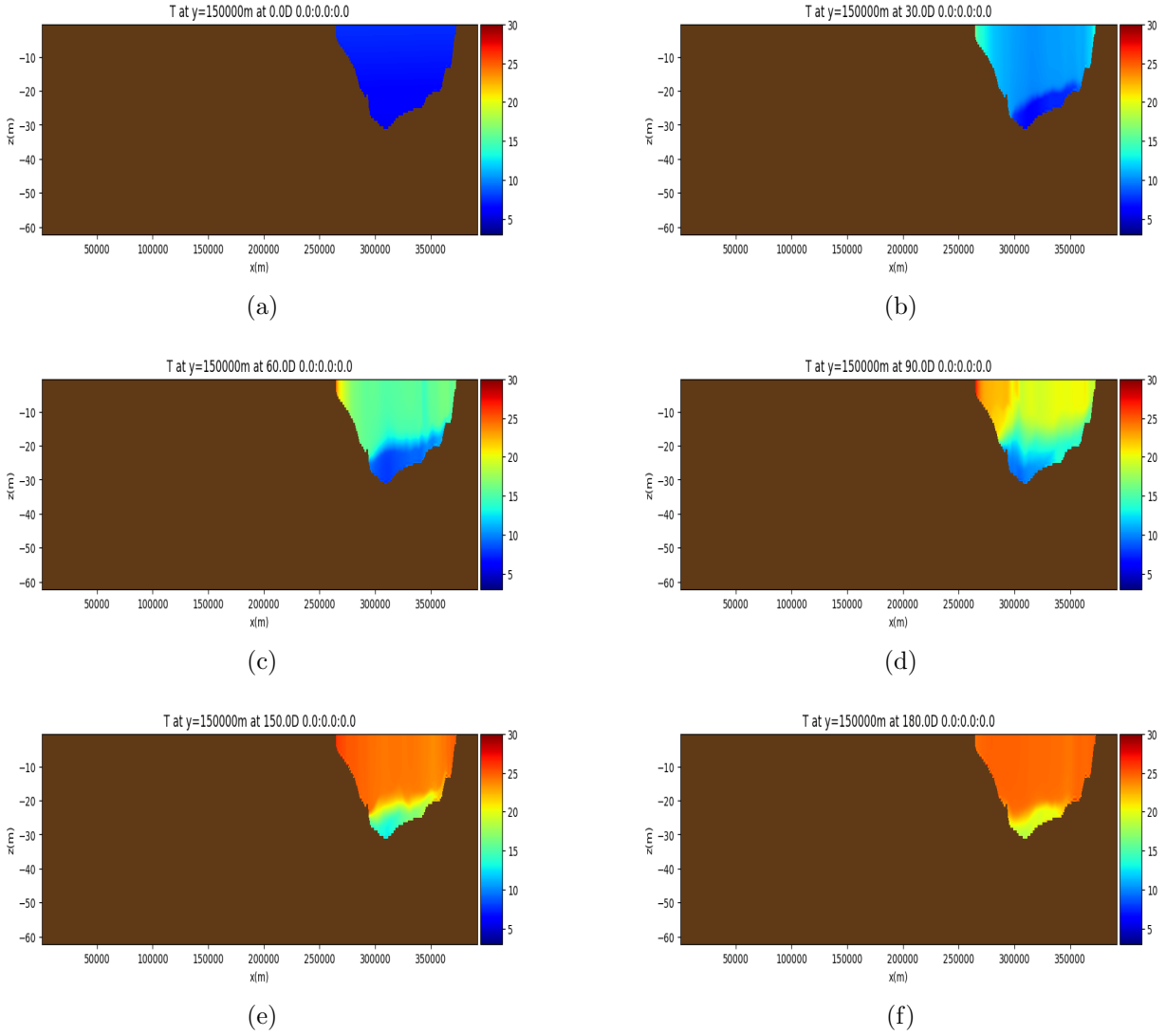

Figure 7.5: Case 3: Similar to Figure 7.3 but for the 3-band short wave radiation model.

7.3 Rerunning the Base Case with a 2-band Jerlov IA while Varying Some of the Forcing Parameters.

Many researchers are interested in simulating the seasonal variations of the lake's thermal structure because of the role it plays in the accurate assessment in the climate effects

on the water quality, lake physics, and biochemical characteristics [17]. Like many researchers, we are curious about the impacts of climate change on the thermal structure of lakes (e.g., Lake Erie), so we decided to model Lake Erie using the default 2-band Jerlov IA shortwave radiation parameterization discussed earlier with some variations in the observed meteorological forcing fields (see Case 4, Case 5, and Case 6).

1. **Case 4**: Modeling Lake Erie using the 2-band Jerlov IA model and increase air temperature. The model setup was exactly like what we had in the Base Case (that is all the forcing data remained the same), but we increased the air temperature by 2 ^oC (see A.3).

2. **Case 5**: The same as Case 4 except we reduced the air temperature by 2 ^oC instead.

3. **Case 6**: Modeling Lake Erie using the 2-band Jerlov IA model with increased inflow (Detroit River) water temperature. The model set up was similar to the Base Case but we increased the temperature of the water inflow from the Detroit River by 50%.

Please note that the plots for the modeled temperature profiles from Case 4, Case 5, and Case 6 are similar to those from the Base Case, thus we chose not to include them in this thesis. However, our findings would be discussed later in this chapter.

7.4 Comparing the Model Results

In this section, we present comparisons of the various cases that use different shortwave radiation models and different forcings.

Central Basin: The first column of Figure 7.6 shows the modeled time depth distribution at station 42 ($x = 150\ km$ and $y = 80\ km$ corresponding to Lake Erie's central basin) for the Base Case (2-band with Jerlov IA); 7.6a, Case 2 (2-band with Jerlov III); 7.6c, and Case 3 (3-band model); 7.6e. For the 3 cases, the water in the lake was initially uniformly mixed with temperature of about 10 ^oC everywhere. Weak stratification appears by the 30^{th} day (22$^{\text{nd}}$ May 2008) followed by strong stratification until the 100^{th} day (30$^{\text{th}}$ July

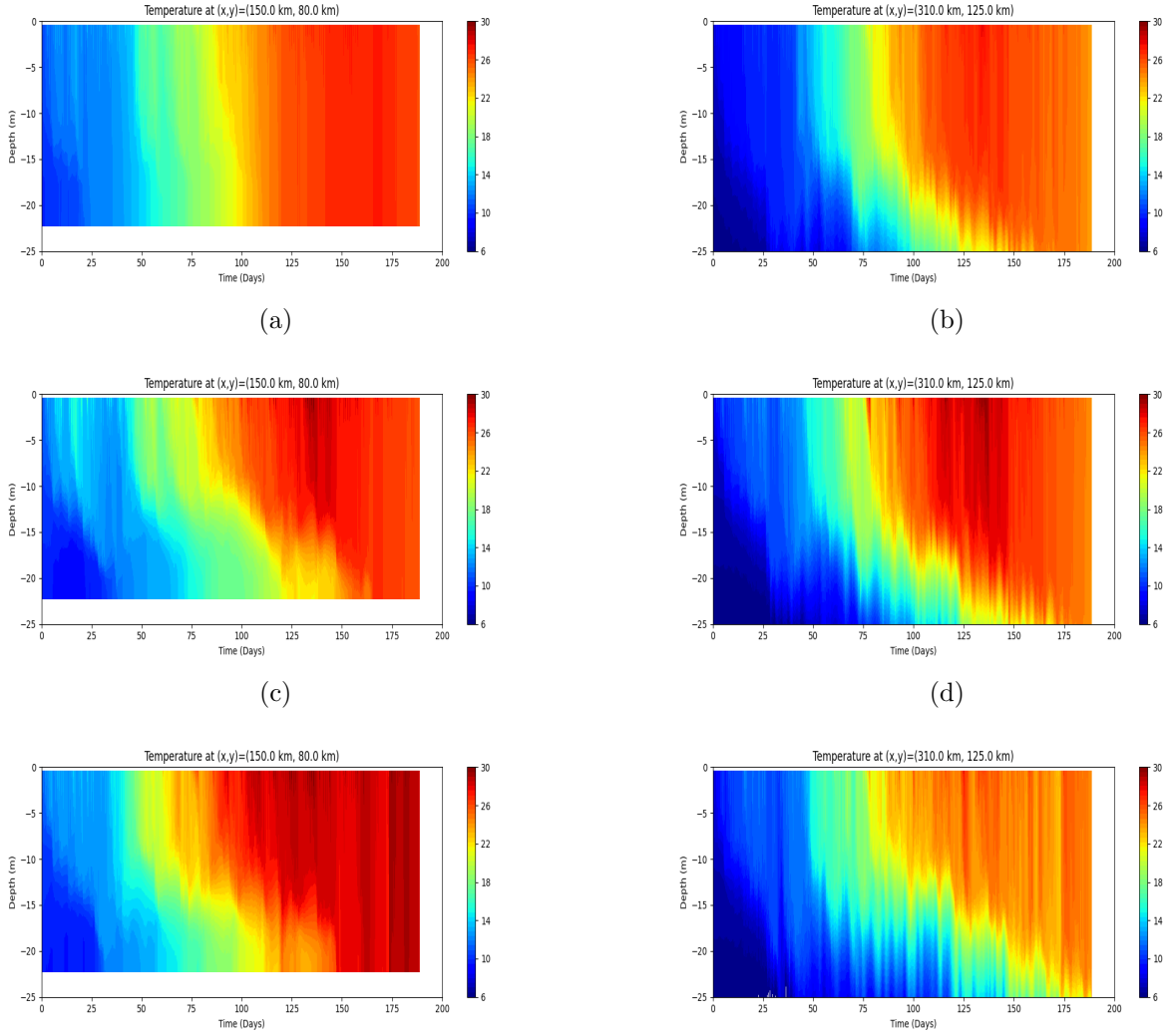

Figure 7.6: Time evolution of vertical temperature profiles at: (a, c, e) station 42 located in the central basin at $(x, y) = (150\ km, 80\ km)$; and (b, d, f) station 23 located in the eastern basin at $(x, y) = (310\ km, 125\ km)$. Shortwave radiation models: Jerlov IA (a, b); Jerlov III (c, d); and 3-band model (e, f). The color panel is the temperature in ^oC.

2008) with upper mixed layer of 10 m, 12 m, and 16 m for the 2-band Jerlov IA, 2-band Jerlov III, and 3-band models, respectively and slightly cold bottom layer.

Observations from Figure 7.6 reveal a rapidly deepening thermocline in the 2-band Jerlov IA than in both the 2-band Jerlov III and the 3-band models in the central basin of Lake Erie. For instance, at day 100 (31st July 2008), the depth of the thermocline are about 13 m, 10 m, and 7 m in the central basin when it was modeled with a 2-band Jerlov IA (Base Case), a 2-band Jerlov III (Case 2), and a 3-band (Case 3), respectively. Weak stratification continues in the central basin till the 60^{th} day (21st June 2008) in the Base Case, 70^{th} day (31st June 2008) in the Case 2, and 60^{th} day (21st June 2008) in Case 3 (see Figures 7.6a, 7.6c, and 7.6e).

In addition, from the vertical temperature profiles (Figures 7.7 and 7.8), it is evident that heat penetration into the water column varies with the different models employed, for example, at the 30th day (22nd May 2008), Jerlov IA produces a temperature difference (between the upper and the lower layers, i.e. $T_s - T_b$) of approximately 0.2 ^oC with the thermocline thickness of about 0.5 m, whereas Case 2 and Case 3 produce approximately 2 ^oC temperature change and approximately 2.7 ^oC water temperature change with the thermocline thicknesses of 3 m and 2 m, respectively. See Tables 7.2, 7.3, 7.4, 7.5, and 7.6 for more details about our observations from the 60th day (21st June 2008) to the end of the simulation, 180th day (19th October 2008).

Models	**Temperature Difference** (^oC)	**Thermocline Thickness** (m)
Jerlov IA (Base Case)	0.2 ($T_s = 16.1$, $T_b = 15.9$)	1
Jerlov III (Case 2)	5.5 ($T_s = 18$ and $T_b = 12.5$)	5
3-band model (Case 3)	7.3 ($T_s = 21.4$ and $T_b = 14.1$)	7

Table 7.2: Central Basin: Comparing the modeled vertical temperature profiles in the central basin for Jerlov IA, Jerlov III, and 3-band model taken at day 60; 7.7b.

Models	**Temperature Difference** (^oC)	**Thermocline Thickness** (m)
Jerlov IA (Base Case)	1.6 ($T_s = 21.8$ and $T_b = 20.2$)	3
Jerlov III (Case 2)	7.2 ($T_s = 24$ and $T_b = 16.8$)	10
3-band model (Case 3)	7.8 ($T_s = 26.2$ and $T_b = 18.4$)	12

Table 7.3: Same as Table (7.2) but taken at day 90; 7.7c

Eastern Basin: Figures 7.6b, 7.6d, and 7.6f show the time evolution of the vertical temperature profiles in the eastern basin from the simulations using the 2-band Jerlov IA,

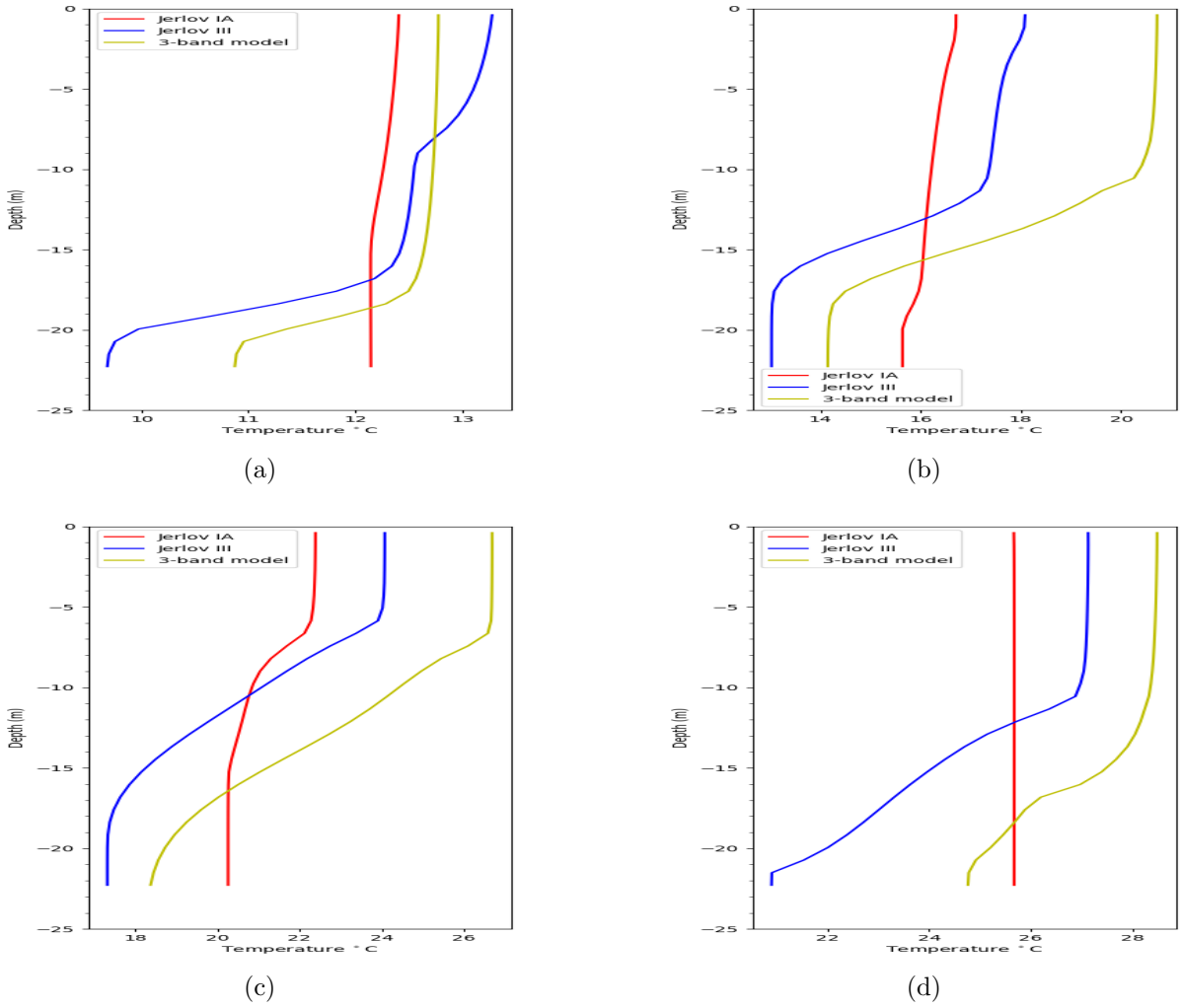

Figure 7.7: Modeled vertical temperature profiles at x=150 km and y = 80 km corresponding to the central basin (station 42) for the Jerlov IA (Red line), Jerlov III (Blue line) and 3-band model (Yellow line) taken at (a) 30 days; (b) 60 days; (c) 90 days; and (d) 120 days.

2-band Jerlov III, and 3-band short wave radiation models, respectively. Similar to the observation in the central basin, the water in this part of the lake was uniformly mixed but with temperature of about 6 ^oC at the beginning of the simulation and up to the 25$^{\text{th}}$ day (17$^{\text{th}}$ May 2008) in the deeper part (say depth of 25 m for these three cases (Base Case, Case

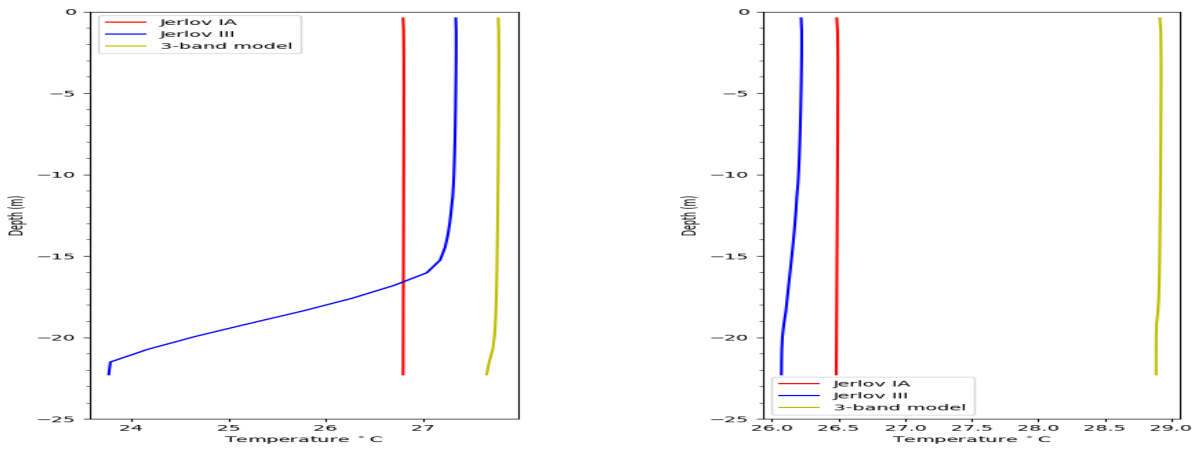

Figure 7.8: Same as Figure 7.7 but taken at (a) 150 days and (b) 180 days

Models	**Temperature Difference** (^oC)	**Thermocline Thickness** (m)
Jerlov IA	Almost uniform	Disappeared
Jerlov III	5.7 ($T_s = 26.9$ and $T_b = 21.2$)	10
3-band model	4.2 ($T_s = 29$ and $T_b = 24.8$)	7

Table 7.4: Same as Table (7.2) but taken at day 120; 7.7d

2, and Case 3). After 25^{th} day, weak stratification started and as the heating intensifies in the summer months, the temperature of water in the lake has increased all the way to the bottom layer around 50^{th} day (11^{th} June 2008) of the simulation for the three cases; Base Case (2-band Jerlov IA), Case 2 (2-band Jerlov III), and Case 3 (3-band model). Again, a rapid deepening of the thermocline was observed in both the Base Case (2-band Jerlov IA) and Case 2 (2-band Jerlov III). In Case 3 (3-band model), the thermocline deepened much more gradually. For example, at the 100^{th} day (31^{st} July 2008) the warm upper mixed layer depth is about 20 m in the Base Case and Case 2 and approximately 13 m in Case 3. Surprisingly, between 120^{th} day (20^{th} August 2008) and 140^{th} day (9^{th} September 2008) of the simulation, Case 2 produces warmer upper mixed layer than Base Case and Case 3. Also, the water temperatures at the end of the simulation is higher (warmer) in the Base Case and Case 2 relative to Case 3. To support our analyses, see Tables A.1, A.2, A.3, A.4, A.5, and A.6 for the comparison of the resulting vertical temperature profiles for the Base Case, Case 2, and Case 3 at different days based on Figures 7.10 and 7.9. Generally,

Models	**Temperature Difference** (^oC)	**Thermocline Thickness** (m)
Jerlov IA	Uniformly mixed	Disappeared
Jerlov III	3.6 ($T_s = 27.4$ and $T_b = 23.8$)	5.5
3-band model	Almost uniform ($T_{avg} = 27.9$)	1

Table 7.5: Same as Table (7.2) but taken at day 150; 7.8a.

Models	**Temperature Difference** (^oC)	**Thermocline Thickness** (m)
Jerlov IA	Uniformly mixed ($T_{avg} = 25$)	Disappeared
Jerlov III	Almost uniform ($T_{avg} = 24$)	Slightly visible
3-band model	Completely mixed ($T_{avg} = 28.9$)	Disappeared

Table 7.6: Same as Table (7.2) but taken at day 180; 7.8b.

3-band model produces the thickest thermocline throughout the period of the simulation (even on day 180) compare to the 2-band model (Jerlov IA and III) in the eastern basin, this is completely different from the results in the central basin.

To further confirm our suspicions about the relationship between the lake's thermal structure and the short wave radiation (the 2-band Jerlov IA, 2-band Jerlov III, and 3-band) penetration depth, we made some time series plots that directly compare the modeled daily temperatures at different depths d (see Figures 7.11 and 7.12). For all the time series plots, the modeled temperature values at depth d are taking from the first cell centre above depth d, i.e., at depths of 0.391, 9.775 and 19.941 for $d = 1\ m$, $10\ m$ and $20\ m$, respectively.

Figure 7.11 shows the time series of the modeled water temperature at different depths in the central basin (station 42) using the 2-band Jerlov IA (Base Case), 2-band Jerlov III (Case 2), and 3-band (Case 3) shortwave radiation parameterization models. Please note that the temperature at depth d use values at the cell centre above the specified depth. At the depth of 1 m in the central basin, Figure 7.11a, the modeled temperature for the three cases are very close for the first 10 days of our simulation. Between days 10 and 30 (22^{nd} May 2008) the 2-band Jerlov III produces the warmest temperature. However, from the 30^{th} day (22^{nd} May 2008) to the end of the simulation (180^{th} day, 19^{th} October 2008) the 3-band model produces the warmest water. The water temperature is very close to 30 ^oC between 110^{th} day (10^{th} August 2008) and 175^{th} day (14^{th} October 2008) (see Figure 7.11a). At the depth of 10 m, the water temperature in the three cases of interest are quite close, similar to the 1 m depth result but this lasted longer especially for the Jerlov III and

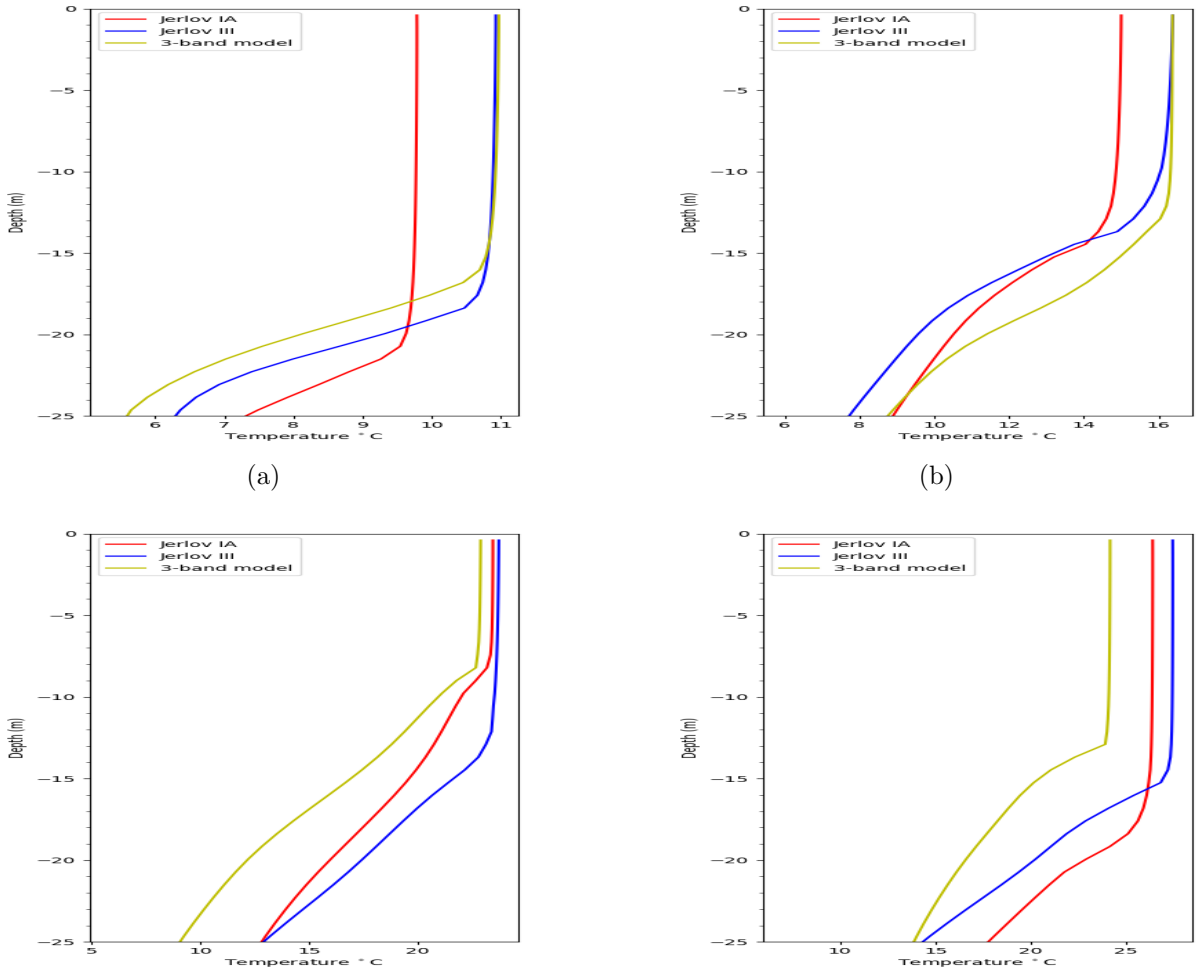

Figure 7.9: Similar to Figure 7.7 but in the eastern basin (Station 23).

3-band models (20 days). From the 30$^{\text{th}}$ day (22$^{\text{nd}}$ May 2008) the 3-band model produces the warmest water of the three cases; over 30 ^{o}C from 120 to 140 days and from 156 to 160. Overall, the 2-band Jerlov IA (Base Case) consistently produces the coolest water relative to 2-band Jerlov III (Case 2) and 3-band (Case 3) with some exceptions from 150$^{\text{th}}$ day when 2-band Jerlov IA (Base Case) and 2-band Jerlov III (Case 2) produce same water temperature (see Figure 7.11b).

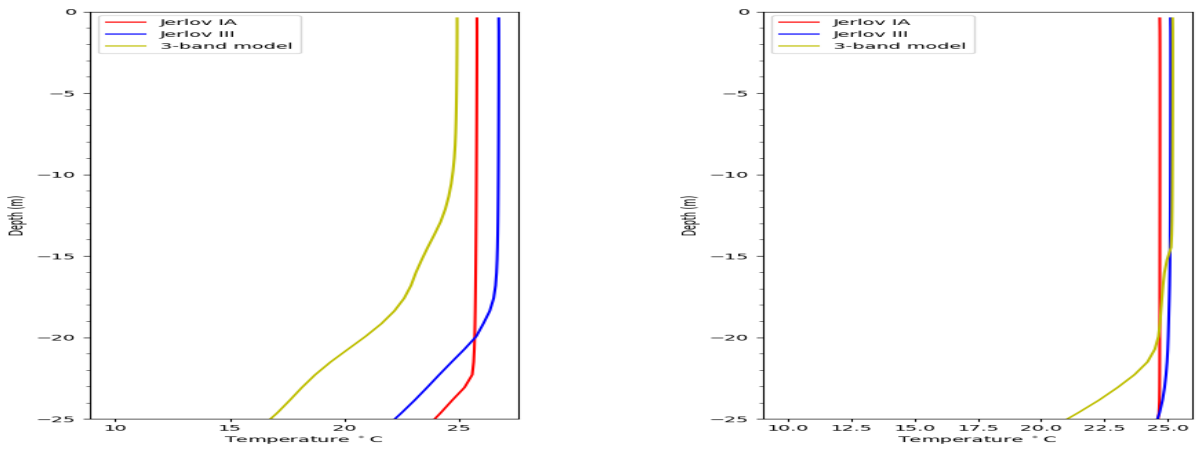

(a) (b)

Figure 7.10: Same as Figure 7.9 but taken at (a) 150 days and (b) 180 days.

At 20 m depth in the central basin, 2-band Jerlov III (Case 2) produces the coldest water relative to the other two cases (2-band Jerlov IA and 3-band model) with exception from 170$^{\text{th}}$ day, (9$^{\text{th}}$ October 2008) to the end of our simulations (180$^{\text{th}}$ day, 19$^{\text{th}}$ October 2008) (see Figure 7.11c), this is justifiable since the distance shortwave radiation penetrates into the water column depends on the extinction component for each band width [22]; (extinction length scales: Jerlov (III) is 9.3 and (IA) is 20.98, see table 3.2) and also the fact that much energy is absorbed near the surface in the 3-band model. In summary for the shortwave parameterization in the central basin of Lake Erie, Jerlov 1A is considered to be better at depth 1 m and 10 m, while Jerlov III performed very well at 20 m depth (i.e. produced less warm water).

Similarly, Figure 7.12 shows the time series of the modeled water temperature at different depths in the eastern basin (station 23) using same three shortwave radiation parameterization models. As mentioned earlier, the temperature at depth d use values at the cell centre above the specified depth. At 1 m and 10 m depths in the eastern basin, the 2-band Jerlov IA consistently produces the coldest water of the three cases of interest up to day 100 (see Figures 7.12a and 7.12b). Unlike the results in the central basin, the 3-band model produces maximum water temperature of less than 25 ^oC (in the three depths explored), even during summer months. At 20 m depth in the eastern basin, the coldest water was produced by the 3-band model from day 75 of the simulation (throughout the summer period) which is not surprising since more energy is absorbed near the surface in a 3-band

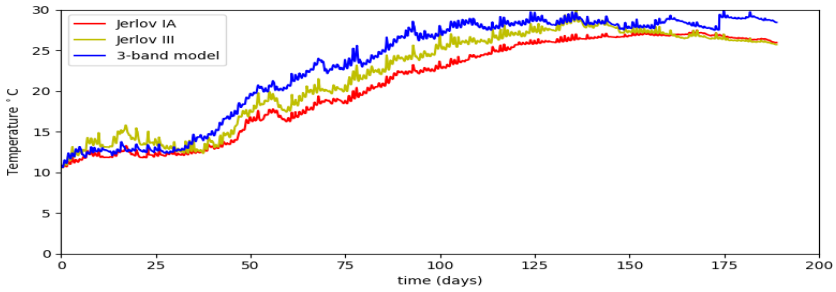

(a)

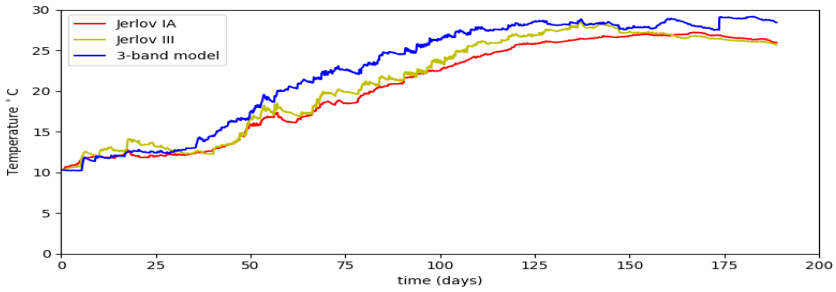

(b)

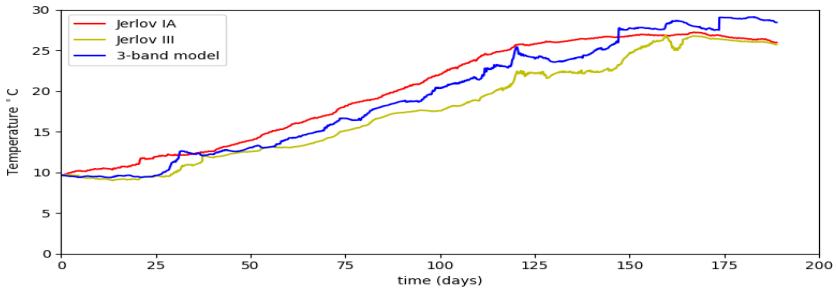

(c)

Figure 7.11: Time series of the modeled water temperature at different depths d at station 42 (central basin; $x = 150\ km$ and $y = 80\ km$) for the Jerlov IA (Red), Jerlov III (Yellow) and 3-band model (Blue) at different depths, with (a), (b), and (c) representing 1 m, 10 m, and 20 m, respectively.

model (see Figure 7.12c). It is important to state that the 3-band model does not result in higher water temperature in both 1 m and 10 m depths in the eastern basin like we saw in the central basin because of the depth of the eastern basin given that larger percentage of

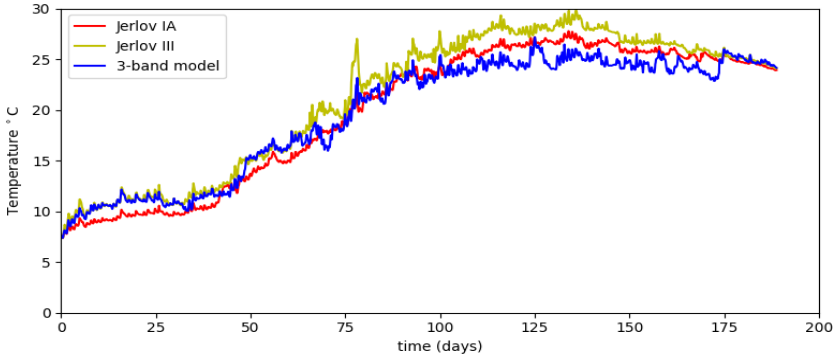

(a)

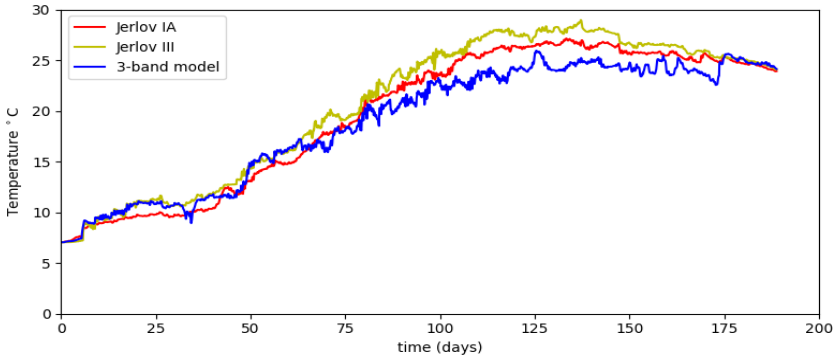

(b)

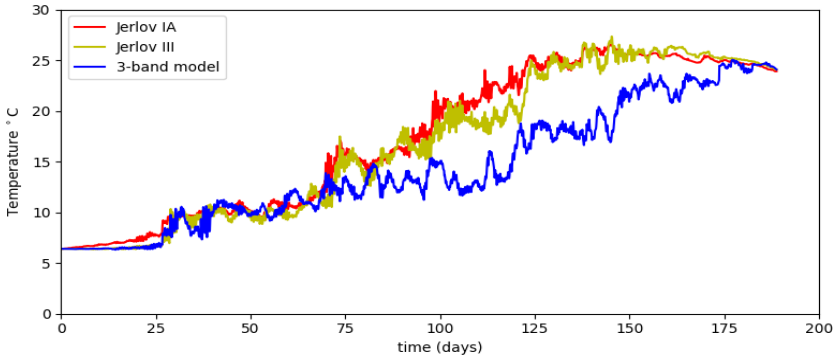

(c)

Figure 7.12: Same as Figure 7.11 but in the eastern basin (station 23).

the shortwave radiation is absorbed near the surface (see Figures 7.12a and 7.12b). Overall, the 3-band model produced less warm water in the eastern basin of the three cases of interest especially at the 20 m depth (see Figure 7.12c).

Figure 7.13 shows the time series of the modeled water temperature at different depths in the eastern basin (station 23) using 2-band Jerlov IA with some changes to the observed forcing field as earlier explained in section 7.4 [increased air temperature by 2 ^oC (Case 4); reduced air temperature by 2 ^oC (Case 5); and increased inflow water temperature by 50% (Case 6)]. Figures 7.13a and 7.13b are the time series at the 1 m and 10 m depths in the eastern basin. Please note that the temperature at depth d use values at the cell centre above the specified depth. From the beginning of our simulation to the end 180^{th} day (19^{th} October 2008), the water temperature for the four cases of interest are very close at 1 m and 10 m depths (see Figures 7.13a and 7.13b). Similar patterns were observed in the central basin, even at the 20 m depth (image not shown), this suggests that overly warm water in Lake Erie has nothing to do with the air temperature and inflow water temperature forcings.

Finally, at 20 m depth in the eastern basin, unlike the results for the 1 m and 10 m depths, the similar water temperatures are only seen in the first 60 days of the simulation, then the values started deviating slightly from one another from 60 days with Case 4 always in the lead with the warmest water and Case 5 with the coolest water, these are quite surprising patterns as one would expect a stronger stratification, less vertical mixing of heat across the thermocline, and colder hypolimnion as a result of the increased air temperature (see Figure 7.13c).

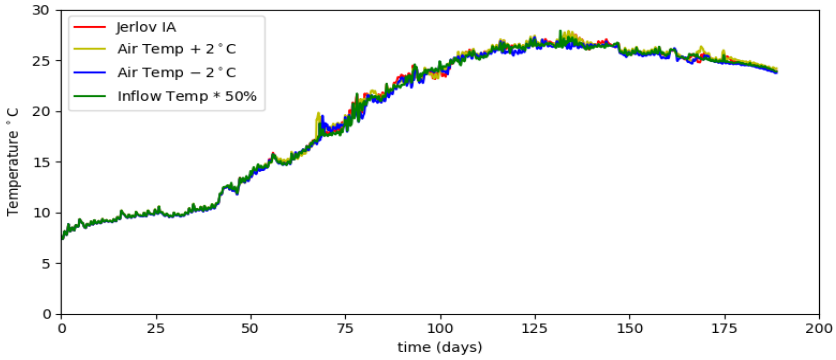

(a)

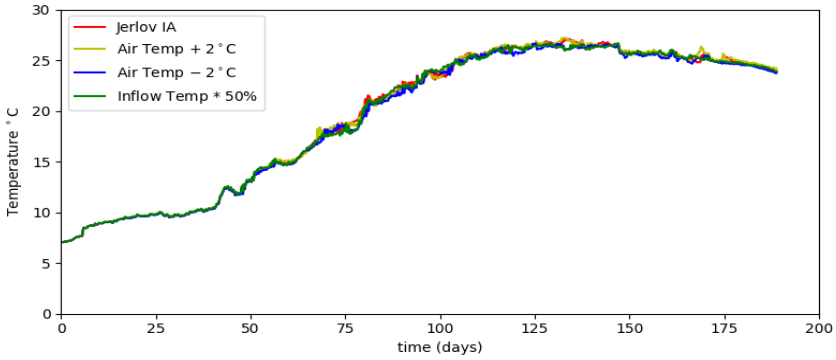

(b)

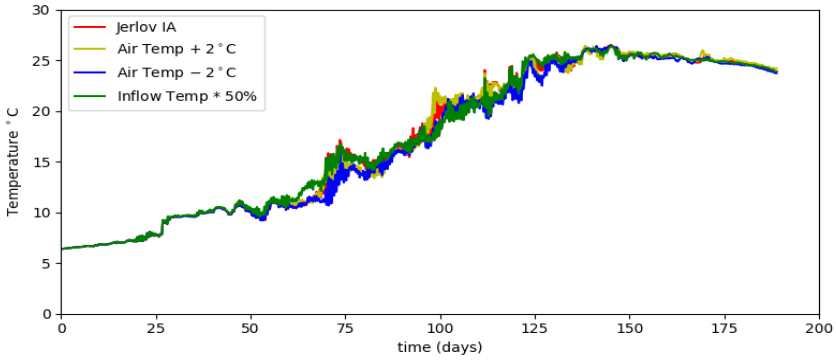

(c)

Figure 7.13: Similar to Figure 7.12 but for the Base Case (Red line), Case 4 (Yellow line), Case 5 (Blue line), and Case 6 (Green line).

Chapter 8

Conclusions

In this chapter we make some conclusions based on our observations from modeling a simple idealized lake and Lake Erie, and potential future work.

8.1 Idealized Lake

In this thesis, we studied the sensitivity of the thermal structure and circulation pattern of a simple Toy Lake over an 8 day period subject to various external forces using the two common 2-band shortwave parameterizations, Jerlov IA and IB, and a 3-band shortwave downward radiation model. The model was forced with South-North linearly varying winds, long wave and short wave radiation, relative humidity, and air temperature. Below are our conclusions based on the model results.

- From the figures and discussions in chapter 6 (e.g. the Base Case), we can conclude that simulating the Toy Lake using the hydrodynamic MITgcm model forced with South-North linearly varying winds of 4 m/s speed produced a dome-shaped thermocline with characteristic counterclockwise circulation pattern in the epilimnion (i.e. above the thermocline).

- Generally, we found great agreement between the modeled results (e.g. the current in the upper layer) and the analytical results.

- We are able to confirm the effect of the Coriolis force on the thermocline's shape and thickness (see Figures 6.4 (modeled with Coriolis force) and 6.6 (modeled with a Coriolis force close to zero)).

- We also explored the roles of the short wave and long wave radiation in modeling the thermal structure of lakes: without the solar radiation (short wave and long wave radiation) the intensity of heating would be reduced which in turn would have impact on the thermal stratification, for instance:

  1. The Toy Lake cools down faster in the case with no shortwave or no longwave radiation than in the case with shortwave and no longwave radiation (see Figures 6.13 and 6.14);
  2. When the shortwave radiation was set to zero but with long wave radiation, water warms up slowly than the case with all the forcing parameters, this is due to the reduced amount of energy entering the lake (see Figures 6.15 and 6.12).

8.2 Lake Erie

We also examined the sensitivity of the thermal structure of Lake Erie for the period of six months to various external forces using the same shortwave downward radiation model as used for the Toy Lake. The model has a horizontal and vertical resolutions of 500 m and 0.782 m, respectively and is forced with meteorological observations obtained from the National Water Research Institute (NWRI) of Environment Canada (EC) and the National Data Buoy Center (NDBC) for the six months of interest in 2008 (April to October). From our model results and discussions in chapter 7, we arrive at the following noteworthy conclusions.

- The modeled water temperatures from all the cases produce comparably similar pattern.

- Incoming shortwave radiation penetrates more deeply into the water column with the 2-band model (Jerlov IA and III; given that they have longer extinction length scales) than the 3-band model in the central basin and the eastern basin of Lake Erie (see Figure 7.6).

- We also found out that the 2-band model (Jerlov IA and III) produced less warm water in the shallow areas than the 3-band model especially during summer period where it (the 3-band model) overestimated the water temperatures (see Figure 7.6e), hence, we suggest that the 3-band model should only be employed for modeling deep lakes for accurate predictions of the thermal structure.

- Further, we noticed that the effects of the selected varied external forcing in some of the cases (Base Case, Case 4, Case 5, and Case 6) is not felt at all at 1 m and 10 m depths in the eastern basin (and central basin; image not shown) (see Figure 7.13a), and that they have slight influence on the thermal structure at 20 m depth; this suggests that overly warm water in Lake Erie has little to do with the air temperature and inflow water temperature forcings, but rather related to the solar radiation (shortwave radiation) (See Figures 7.13b and 7.13c).

- The modeled water temperatures are too warm (see Fig. 4 and Fig. 6 in [17]) and more work needs to be done to determine the reasons behind this.

References

[1] Adcroft A., Hill C., Campin J., Marshall J., and Heimbach P. Overview of the formulation and numerics of the mit gcm. *Ocean Modelling*, 1:139–149, 0000.

[2] Mohsen Abdel-Tawwab, Mohamed N. Monier, Seyed Hossein Hoseinifar, and Caterina Faggio. Fish response to hypoxia stress: growth, physiological, and immunological biomarkers. *Fish Physiology Biochemistry*, 45:997–1013, 2019.

[3] Adcroft Alistair and Campin Jean-Michel. Rescaled height coordinates for accurate representation of free-surface flows in ocean circulation models. *Ocean Modelling*, 7:269–284, 2004.

[4] World Atlas. Which country has the most lakes in the world? https://www.worldatlas.com/articles/which-country-has-the-most-lakes-in-the-world.html, October 2022. Last checked on October, 2022.

[5] Dmitry Beletsky, Nathan Hawley, and Yerubandi R. Rao. Modeling summer circulation and thermal structure of Lake Erie. *Geophysical Research: Oceans*, 118:1–15, 2015.

[6] Dmitry Beletsky, Nathan Hawley, Yerubandi R. Rao, Henry A. Vanderploeg, Raisa Beletsky, David J. Schwab, and Steven A. Ruberg. Summer thermal structure and anticyclonic circulation of Lake Erie. *Geophysical Research Letters*, 39:1–6, 2012.

[7] Dmitry Beletsky and David J. Schwab. Modeling circulation and thermal structure in Lake Michigan: Annual cycle and interannual variability. *Journal of Geophysical Research*, 106:19745–19771, 2001.

[8] Dmitry Beletsky and David J. Schwab. Modeling circulation and thermal structure in Lake Michigan: Annual cycle and interannual variability. *Geophysical Research*, 106:19745–19771, 2015.

[9] William L. Blewett. Lake Erie and Lake St. Clair Handbook by Stanley J. Bolsenga and Charles E. Herdendorf. *Association of the American Geographers*, 85:744–745, 1995.

[10] Oxford University Press blog (OUPblog). Dead zones: Growing areas of aquatic hypoxia are threatening our oceans and rivers. https://blog.oup.com/2021/02/dead-zones-growing-areas-of-aquatic-hypoxia-are-threatening-our-oceans-and-rivers/ July 2022. Last checked on July, 2022.

[11] Bertram Boehrer and Martin Schultze. Stratification of lakes. *Reviews of Geophysics*, 46:1–27, 2008.

[12] Britannica. Lake Erie. https://www.britannica.com/place/Lake-Erie, July 2022. Last checked on July, 2022.

[13] New Brunswick. Lake properties. https://www2.gnb.ca/content/gnb/en/departments/elg/environment/content/water/content/lakes/properties.html, October 2022. Last checked on October, 2022.

[14] BYJU'S. Eutrophication. https://byjus.com/chemistry/eutrophication/, July 2022. Last checked on July, 2022.

[15] Joseph D. Conroy, Leon Boegman, Hongyan Zhang, William J. Edwrads, and David A. Culver. "Dead Zone dynamics in Lake Erie: the importance of weather and sampling intensity for calculated hypolimnetic oxygen. *Aquatic Sciences*, 73:289–304, 2011.

[16] Shepard D. A two-dimensional interpolation for irregularly-spaced data function. *In Proceedings of the 1968 ACM National Conference*, 00:517–524, 1968.

[17] G. Djoumna, Kevin G. Lamb, and Yerubandi R. Rao. Sensitivity of the parameterizations of vertical mixing and radiative heat fluxes on the seasonal evolution of the thermal structure of Lake Erie. *Atmosphere-Ocean*, 56:294–313, 2014.

[18] Edublogs. DP Geography at NIS/The diagram above shows the Earth-Atmosphere energy balance. https://cpb-us-e1.wpmucdn.com/share.nanjing-school.com/dist/1/43/files/2012/10/Solar-long-wave-energy-balance-19mx61t.jpg, September 2022. Last checked on Sep 20, 2022.

[19] National Geographic. Lake. https://education.nationalgeographic.org/resource/lake, July 2022. Last checked on July, 2022.

[20] Adrian E. Gill. *Atmosphere-Ocean Dynamics*. Academic Press, London, UK, 1982.

[21] John Greenbank. Limnological conditions in ice-covered lakes, especially as related to winter-kill of fish. *Ecological Society of America*, 15:345–390, 1945.

[22] Ben Hodges and Chris Dallimore. Estuary, lake and coastal ocean model: Elcom. *Science Manual*, 2.2:1–46, 2006.

[23] Penelope Howell and David Simpson. Abundance of marine resources relation to dissolved oxygen in long island sound. *Estuaries*, 17:394–402, 1994.

[24] Kolumban Hutter, Yongqi Wang, and Irina P. Chubarenko. *Physics of Lakes: Foundation of the Mathematical and Physical Background*, volume 1. Springler, Verlag Berlin Heidelberg, 2011.

[25] Jörg Imberger and John C. Patterson. Advances in applied mechanics. *Physical Limnology*, 27:303–475, 1990.

[26] Marshall J., Adcroft A., Hill C., Perelman L., and Heisey C. A finite-volume, incompressible Navier Stokes model for studies of the ocean on parallel computers. *Geophysical Research*, 102(C3):5753–5766, 1997.

[27] William M. Lewis Jr. A revised classification of lakes based on mixing. *Fisheries and Aquatic Sciences*, 40:1779–1787, 1983.

[28] Pijush K. Kundu and Ira M. Cohen. *Fluid Mechanics*. Academic Press, London, UK, 2002, 1990.

[29] Andre Morel and David Antoine. Heating rate within the upper ocean in relation to its bio-optical state. *Physical Oceanography*, 24:1652–1665, 1993.

[30] Andre Morel and David Antone. Heating rate within the upper ocean in relation to its bio-optical state. *Physical Oceanography*, 24:1652–1665, 1993.

[31] Qianru Niu, Meng Xia, Edward S. Rutherford, Doran M. Mason, Eric J. Anderson, and David J. Schwab. Investigation of interbasin exchange and interannual variability in Lake Erie using an unstructured-grid hydrodynamic model. *Geophysical Research: Oceans*, 120:187–191, 2015.

[32] Water on the Web by the University of Minnesota. Lake ecology primer: Biological- lake zones. https://www.waterontheweb.org/under/lakeecology/10_biological_lakezones.html, July 2022. Last checked on July, 2022.

[33] Krishnakumar Ranganathan. Lake restoration: Triozon-Lake structure presentation.ppt final. https://www.slideshare.net/KrishnakumarRanganathan/triozonlake-structure-presentationppt-final, July 2022. Last checked on July, 2022.

[34] Yerubandi R. Rao, Nathan Hawley, Murray N. Charlton, and William M. Schertzer. Physical processes and hypoxia in the central basin of Lake Erie. *Limnology and Oceanography*, 53:2007–2020, 2008.

[35] Yerubandi R. Rao, Todd Howell, Susan B. Watson, and Scott Abernethy. On hypoxia and fish kills along the north shore of Lake Erie. *Great Lakes Research*, 40:187–191, 2014.

[36] National Ocean Services. What is eutrophication? https://oceanservice.noaa.gov/facts/eutrophication.html, October 2022. Last checked on October, 2022.

[37] Joshua M. Tellier, Nicholas I. Kalejs, Benjamin S. Leonhardt, David Cannon, Tomas O. Höök, and Paris D. Collingsworth. Widespread prevalence of hypoxia and the classification of hypoxic conditions in the Laurentian Great Lakes. *Great Lakes Research*, 48:13–23, 2022.

[38] Susan B. Watson, Caro Miller, George Arhonditsis, George L. Boyer, Wayne Carmichael, Murray N. Charlton, Remegio Confesor, David C. Depew, Tomas O. Höök, Stuart A. Ludsin, Gerald Matisoff, Shawn P. McElmurry, Michael W. Murray, R. Petter Richards, Yerubandi R. Rao, Morgan M. Steffen, and Steven W. Wilhelm. The re-eutrophication of Lake Erie: Harmful algal blooms and hypoxia. *Elsevier Harmful Algae*, 56:44–66, 2016.

[39] Robert G. Wetzel. *Limnology: Lake and River Ecosystems*. Academic Press, California, USA, 2001, 1983, 1975.

[40] Wikipedia. Amictic lake. https://en.wikipedia.org/wiki/Amictic_lake, July 2022. Last checked on July, 2022.

[41] Wikipedia. Dimictic lake. https://en.wikipedia.org/wiki/Dimictic_lake, July 2022. Last checked on July, 2022.

[42] Wikipedia. Geostrophic current. https://en.wikipedia.org/wiki/Geostrophic_current, July 2022. Last checked on July, 2022.

[43] Wikipedia. Lake. https://en.wikipedia.org/wiki/Lake, June 2022. Last checked on June, 2022.

[44] Wikipedia. Meromictic lake. https://en.wikipedia.org/wiki/Meromictic_lake, July 2022. Last checked on July, 2022.

[45] Wikipedia. Monomictic lake. https://en.wikipedia.org/wiki/Monomictic_lake, July 2022. Last checked on July, 2022.

[46] Wikipedia. Polymictic lake. https://en.wikipedia.org/wiki/Polymictic_lake, July 2022. Last checked on July, 2022.

[47] Alfred Wüest and Andreas Lorke. Small-scale hydrodynamics in lakes. *Annual Reviews of Fluid Mechanics*, 35:373–412, 2003.

[48] Bai X. Z., Wang J., Schwab D. J., Yang Y., Luo L., Leshkevich G. A., and Liu S. Z. Modeling 1993–2008 climatology of seasonal general circulation and thermal structure in the great lakes using fvcom. *Ocean Modelling*, 65:40–63, 2013.

APPENDICES

Appendix A

Python Code for Generating the Forcing Data and Tables from the Model Results Comparison

A.1 Tables from the Model Results Comparison-Eastern Basin

Models	**Change in Temperature** (^oC)	**Thermocline Thickness** (m)
Jerlov IA	2.5 ($T_s = 9.8$ and $T_b = 7.3$)	3.5
Jerlov III	4.5 ($T_s = 10.8$ and $T_b = 6.3$)	6
3-band model	5 ($T_s = 10.8$ and $T_b = 5.8$)	7

Table A.1: Eastern Basin: Comparing the modeled vertical temperature profiles in the eastern basin for Jerlov IA, Jerlov III, and 3-band model taken at day 30; 7.9a.

Models	**Change in Temperature** (^oC)	**Thermocline Thickness** (m)
Jerlov IA	5.5 ($T_s = 14.5$ and $T_b = 9$)	5
Jerlov III	9.4 ($T_s = 16.2$ and $T_b = 6.8$)	5
3-band model	7.2 ($T_s = 16.2$ and $T_b = 9$)	7

Table A.2: Same as Table (A.1) but taken at day 60; 7.9b.

Models	Change in Temperature (^oC)	Thermocline Thickness (m)
Jerlov IA	9.5 ($T_s = 23$ and $T_b = 13.5$)	2
Jerlov III	10.5 ($T_s = 24$ and $T_b = 13.5$)	4
3-band model	13 ($T_s = 22$ and $T_b = 9$)	12

Table A.3: Same as Table (A.1) but taken at day 90; 7.9c

Models	Change in Temperature (^oC)	Thermocline Thickness (m)
Jerlov IA	7 ($T_s = 25$ and $T_b = 18$)	5
Jerlov III	12.5 ($T_s = 27$ and $T_b = 14.5$)	4
3-band model	14 ($T_s = 28$ and $T_b = 14$)	6

Table A.4: Same as Table (A.1) but taken at day 120; 7.9d

A.2 Python Routine for the Forcing Data

All forcing data for the Lake Erie simulation were generated from the Python routine below.

```
# EC: Environment Canada

# Colb: Colborne

# Stl: Port Stanley

# SBI: South Bass Island

# 2008met_01_Extend.dat:   data from EC Colborne
#  2008met_02_Extend.dat:   data from Port Stanley
#  2008met_03_Extend.dat:   data from EC 341
#  2008met_04_Extend.dat:   data from South Bass Island
```

Locations of interest are on Figure 5.4 of this thesis.

```
#  Columns are:
#     time in days  (hourly)
#     wind speed
```

Models	Change in Temperature (^oC)	Thermocline Thickness (m)
Jerlov IA	2 ($T_s = 26$ and $T_b = 24$)	2
Jerlov III	5 ($T_s = 28$ and $T_b = 23$)	4
3-band model	7.5 ($T_s = 23.5$ and $T_b = 16$)	8

Table A.5: Same as Table (A.1) but taken at day 150; 7.8a.

Models	Change in Temperature(^oC)	Thermocline Thickness (m)
Jerlov IA	Completely mixed ($T_{avg} = 24.9$)	Disappeared
Jerlov III	Almost uniform ($T_{avg} = 24.9$)	Disappeared
3-band model	3 ($T_s = 24.9$ and $T_b = 21.8$)	5

Table A.6: Same as Table (A.1) but taken at day 180; 7.10b.

```
#     wind direction
#     shortwave radiation
#     temperature
#     humidity
#     longwave radiation


import numpy as np
from convert_lat_lon_to_km_forcing import *
from bathyfix import *
from math import pi
from scipy import interpolate, ndimage
import matplotlib
matplotlib.use('Agg')
import matplotlib.pyplot as plt
from variables import *
from pylab import imshow, show
import gc

degrees_to_radians = pi/180

dt = np.dtype('>f8')

#Loading data :
A_1 = np.loadtxt('2008met_03_Extend.dat')
A_2 = np.loadtxt('2008met_02_Extend.dat')
A_3 = np.loadtxt('2008met_01_Extend.dat')
A_4 = np.loadtxt('2008met_04_Extend.dat')


#plotting X and Y
Xp = 100
Yp = 50

#manual spacing override
ny = nyd
nx = nxd
```

```
# number of data values
Nb = len(A_1[:,0])

# 4000  28 day left (JD 278.625)

B2_341 = np.zeros((Nb))
B3_341 = np.zeros((Nb))

# All- and long-wave radiation
B4_341 = np.zeros((Nb))
B7_341 = np.zeros((Nb))
#B1_Stl = np.zeros((Nb))     #remove
B2_Stl = np.zeros((Nb))
B3_Stl = np.zeros((Nb))
B4_Stl = np.zeros((Nb))
B7_Stl = np.zeros((Nb))

#B1_Colb = np.zeros((1,Nb))    #remove
B2_Colb = np.zeros((Nb))
B3_Colb = np.zeros((Nb))
B4_Colb = np.zeros((Nb))
B7_Colb = np.zeros((Nb))

#B1_SBI = np.zeros((Nb))  #remove

B2_SBI = np.zeros((Nb))
B3_SBI = np.zeros((Nb))
B4_SBI = np.zeros((Nb))
B7_SBI = np.zeros((Nb))

Tref = 273.2

B1 = np.zeros((Nb))
B11 = np.zeros((Nb))
wind_speed_341 = np.zeros((Nb))
wind_dir_341 = np.zeros((Nb))

#B1_Stl = np.zeros((Nb))    #remove
wind_speed_Stl = np.zeros((Nb))
wind_dir_Stl = np.zeros((Nb))


#B1_Colb = np.zeros((Nb))    #remove
wind_speed_Colb = np.zeros((Nb))
wind_dir_Colb = np.zeros((Nb))

#B1_SBI = np.zeros((Nb))  #remove
wind_speed_SBI = np.zeros((Nb))
wind_dir_SBI = np.zeros((Nb))



#Loops
for i in range(Nb):
    #EC 341
    B11[i]      = (A_1[i,0]-2008000)
    B1[i]      = (A_1[i,0]-A_1[0,0])*24*3600

 wind_speed_341[i]    = A_1[i,1]
    wind_dir_341[i]    = A_1[i,2]
```

```
    #EC Stanley
    wind_speed_Stl[i]    = A_2[i,1]
    wind_dir_Stl[i]    = A_2[i,2]

    #EC Colborne
    wind_speed_Colb[i]    = A_3[i,1]
    wind_dir_Colb[i]    = A_3[i,2]

    #SBI01
    wind_speed_SBI[i]    = A_4[i,1]
    wind_dir_SBI[i]    = A_4[i,2]

    # EC 341
    B2_341[i]    = A_1[i,4]+Tref
    B3_341[i]    = A_1[i,5]
    B4_341[i]    = A_1[i,3]
    B7_341[i]    = A_1[i,6]

    #EC Stanley
    B2_Stl[i]    = A_2[i,4]+Tref
    B3_Stl[i]    = A_2[i,5]
    B4_Stl[i]    = A_2[i,3]
    B7_Stl[i]    = A_2[i,6]


    #EC Colborne
    B2_Colb[i]    = A_3[i,4]+Tref
    B3_Colb[i]    = A_3[i,5]
    B4_Colb[i]    = A_3[i,3]
    B7_Colb[i]    = A_3[i,6]

    #SBI01
    B2_SBI[i]    = A_4[i,4]+Tref
    B3_SBI[i]    = A_4[i,5]
    B4_SBI[i]    = A_4[i,3]
    B7_SBI[i]    = A_4[i,6]


# compute zonal (u) and meridional (v) wind velocities. Direction is the
direction the wind domes from in degrees c from north.
# so for direction = 0 (u,v) = (0,-wind_speed) and for direction = 90

degrees (u,v) = (-wind_speed, 0)

u_341 = -wind_speed_341*np.sin(degrees_to_radians*wind_dir_341)
v_341 = -wind_speed_341*np.cos(degrees_to_radians*wind_dir_341)

u_Colb = -wind_speed_Colb*np.sin(degrees_to_radians*wind_dir_Colb)
v_Colb = -wind_speed_Colb*np.cos(degrees_to_radians*wind_dir_Colb)

u_Stl = -wind_speed_Stl*np.sin(degrees_to_radians*wind_dir_Stl)
v_Stl = -wind_speed_Stl*np.cos(degrees_to_radians*wind_dir_Stl)

u_SBI = -wind_speed_SBI*np.sin(degrees_to_radians*wind_dir_SBI)
v_SBI = -wind_speed_SBI*np.cos(degrees_to_radians*wind_dir_SBI)


# plt.plot(np.linspace(0, 190, len(B2_341)), B2_341, label='341')
#plt.plot(np.linspace(0, 190, len(B2_341)), B2_Stl, label='Stl')
#plt.plot(np.linspace(0, 190, len(B2_341)), B2_Colb, label='Colb')
```

```
#plt.plot(np.linspace(0, 190, len(B2_341)), B2_SBI, label='SBI')
#plt.ylabel("Temperature K")
#plt.xlabel("Time (days)")
#plt.legend()
#plt.show()
#plt.clf()

#Lat/Lon values of buoys
mx_341  =  82.3803
mx_Stl  =  81.2156
mx_Colb = 79.2509
mx_SBI  = 82.8

my_341  = 41.89144
my_Stl  = 42.64
my_Colb = 42.84
my_SBI  = 41.6

x = -x

print(x,y)

#converts lat/lon values to KM and fits to relevant grid
(xKm, yKm) =convert_lat_lon_to_km([mx_341, mx_Stl, mx_Colb,

mx_SBI],[my_341, my_Stl, my_Colb, my_SBI])

(xLow, yLow) = convert_lat_lon_to_km([78], [41])
(xHigh, yHigh) = convert_lat_lon_to_km([84], [43])
'''
mx_341_km = (xHigh - xKm[0]) * nx / (xHigh - xLow)
my_341_km = (yHigh - yKm[0]) * ny / (yHigh - yLow)

mx_Stl_km = (xHigh - xKm[1]) * nx / (xHigh - xLow)
my_Stl_km = (yHigh - yKm[1]) * ny / (yHigh - yLow)

mx_SBI_km = (xHigh - xKm[2]) * nx / (xHigh - xLow)
my_SBI_km = (yHigh - yKm[2]) * ny / (yHigh - yLow)

mx_Colb_km = (xHigh - xKm[3]) * nx / (xHigh - xLow)
my_Colb_km = (yHigh - yKm[3]) * ny / (yHigh - yLow)
'''

mx_341_km = int(185*500/dx)
my_341_km = int(120*500/dx)

mx_SBI_km = int(115*500/dx)
my_SBI_km = int(55*500/dx)

mx_Stl_km = int(377*500/dx)
my_Stl_km = int(285*500/dx)

mx_Colb_km = int(701*500/dx)
my_Colb_km = int(329*500/dx)

print(mx_341_km, my_341_km)
print(mx_Stl_km, my_Stl_km)
print(mx_SBI_km, my_SBI_km)
print(mx_Colb_km, my_Colb_km)
```

```
(X, Y) = convert_lat_lon_to_km(x,y)

for i in range(len(X)):
    X[i] = (xHigh - X[i]) * nx / (xHigh - xLow)
#    print(X[i])

for i in range(len(Y)):
    Y[i] = (yHigh - Y[i]) * ny / (yHigh - yLow)

print(X,Y)

X=range(0,nx)
Y=range(0,ny)

Nbb=1


#Wind  for the whole domain
Wind   = np.zeros((nx,ny,Nbb), dtype = dt)
PHI    = np.zeros((nx,ny,Nbb), dtype = dt)


#Zonal and meridional Wind, stress for the whole domain
ZWind   = np.zeros((nx,ny,Nbb), dtype = dt)
MWind   = np.zeros((nx,ny,Nbb), dtype = dt)
ZWind_341   = np.zeros((nx,ny,Nbb), dtype = dt)
MWind_341   = np.zeros((nx,ny,Nbb), dtype = dt)
ZWind_Stl   = np.zeros((nx,ny,Nbb), dtype = dt)
MWind_Stl   = np.zeros((nx,ny,Nbb), dtype = dt)
ZWind_Colb   = np.zeros((nx,ny,Nbb), dtype = dt)
MWind_Colb   = np.zeros((nx,ny,Nbb), dtype = dt)
ZWind_SBI   = np.zeros((nx,ny,Nbb), dtype = dt)
MWind_SBI   = np.zeros((nx,ny,Nbb), dtype = dt)



#All- and Long-wave radiation throughout the whole domain
SOR_2008 = np.zeros((nx,ny,Nbb), dtype = dt)
LWR_2008 = np.zeros((nx,ny,Nbb), dtype = dt)
Temp     = np.zeros((nx,ny,Nbb), dtype = dt)
REL_HUM  = np.zeros((nx,ny,Nbb), dtype = dt)
AIR_PRES = np.zeros((nx,ny,Nbb), dtype = dt)
HS = np.zeros((nx,ny,Nbb), dtype = dt)


#array distances from buoys
ds_341       = np.zeros((len(X),len(Y)))
ds_Stl       = np.zeros((len(X),len(Y)))
ds_Colb      = np.zeros((len(X),len(Y)))
ds_SBI       = np.zeros((len(X),len(Y)))
d_Sum_Prod   = np.zeros((len(X),len(Y)))

Y=Y[::-1]

print(np.shape(X))
print(np.shape(Y))

for k in range(len(X)):
    for j in range(len(Y)):
```

```
        ds_341[k,j]  = ( abs(X[k] - mx_341_km)**2 + abs(Y[j] - my_341_km)**2 )
#        print(X[k]-mx_341_km)
        ds_Stl[k,j]  = ( abs(X[k] - mx_Stl_km)**2 + abs(Y[j] - my_Stl_km)**2 )
        ds_Colb[k,j] = ( abs(X[k] - mx_Colb_km)**2 + abs(Y[j] - my_Colb_km)**2 )
        ds_SBI[k,j]  = ( abs(X[k] - mx_SBI_km)**2 + abs(Y[j] - my_SBI_km)**2 )
#        print(ds_341[k,j])

#xnew=range(0,nxd)
#ynew=range(0,nyd)

#f341=interpolate.interp2d(X, Y, ds_341)
#ds_341=f341(xnew, ynew)
#fStl=interpolate.interp2d(X, Y, ds_Stl)
#ds_Stl=fStl(xnew, ynew)
#fColb=interpolate.interp2d(X, Y, ds_Colb)
#ds_Colb=fColb(xnew, ynew)
#fSBI=interpolate.interp2d(X, Y, ds_SBI)
#ds_SBI=fSBI(xnew, ynew)

'''
plt.imshow(ds_341)
plt.colorbar()
plt.show()

plt.imshow(ds_Stl)
plt.colorbar()
plt.show()

plt.imshow(ds_Colb)
plt.colorbar()
plt.show()

plt.imshow(ds_SBI)
plt.colorbar()
plt.show()
'''

#print (ds_341)
d_Sum_Prod = ds_Stl*ds_Colb*ds_SBI + ds_341*ds_Colb*ds_SBI +

ds_341*ds_Stl*ds_SBI + ds_341*ds_Stl*ds_Colb


alb_LW  = 0.08
albedo = 0.1


#computes these coefficient arrays out of main loop to save computation time
d1 = ds_Stl * ds_Colb * ds_SBI / d_Sum_Prod
d2 = ds_341 * ds_Colb * ds_SBI / d_Sum_Prod
d3 = ds_341 * ds_Stl * ds_SBI / d_Sum_Prod
d4 = ds_341 * ds_Stl* ds_Colb / d_Sum_Prod

print(np.max(d1))
print(np.max(d2))
print(np.max(d3))
print(np.max(d4))


print ("done phase 1!")
```

```
#gc.collect()

#opens file to write
#Zdata = np.fromfile('ZonalWind_Erie2008_MITgcm_200m.bin', dtype='>f8',

count=-1)
#Zdata = Zdata.reshape((Nb, ny, nx))

#Mdata = np.fromfile('MeridWind_2008_MITgcm_200m.bin', dtype='>f8',

count=-1)
#Mdata = Mdata.reshape((Nb, ny, nx))


ZWind_fid = open("zonal_wind.bin", "wb")
MWind_fid = open("merid_wind.bin", "wb")
T_fid = open("temperature.bin", "wb")
RH_fid = open("relative_humidity.bin", "wb")
HS_fid = open("HS.bin", "wb")
SOR_2008_fid = open("shortwave_rad.bin", "wb")
LWR_2008_fid = open("longwave_rad.bin", "wb")



#coefficients for use in main loop calculations
C = 0.98/1.22 * 640380
SD = 1 - albedo
LD = 1 -  alb_LW

abscissa = []
ordinates =  []

uwindplot=[]
vwindplot=[]
tempplot=[]
lwplot=[]
swplot=[]
humplot=[]
timecount=[]
tempplotdata=np.zeros((nx,ny,Nb))
swplotdata=np.zeros((nx,ny,Nb))
lwplotdata=np.zeros((nx,ny,Nb))


#main interpolation loop
for j in range(Nb):

    ZWind[:,:,0] = np.fliplr( u_341[j]*d1[:,:] +  u_Stl[j]*d2[:,:]
                            + u_Colb[j]*d3[:,:] + u_SBI[j]* d4[:,:] )
    MWind[:,:,0] = np.fliplr( v_341[j]*d1[:,:] +  v_Stl[j]*d2[:,:]
                            + v_Colb[j]*d3[:,:] + v_SBI[j]* d4[:,:] )

#    Wind[:,:,0] = np.fliplr( wind_speed_341[j]*d1[:,:] +  wind_speed_Stl[j]*d2[:,:]

#                             + wind_speed_Colb[j]*d3[:,:] +

wind_speed_SBI[j]* d4[:,:] )

    PHI[:,:,0] = np.fliplr( wind_dir_341[j]*d1[:,:] +  wind_dir_Stl[j]*d2[:,:]
```

```
                            + wind_dir_Colb[j]*d3[:,:] + wind_dir_SBI[j]*d4[:,:] )

    Temp[:,:,0] = np.fliplr( B2_341[j]*d1[:,:] + B2_Stl[j]*d2[:,:]
                             + B2_Colb[j]*d3[:,:] + B2_SBI[j]*d4[:,:] )
                             # / 4 + 3*Tref/4

    REL_HUM[:,:,0] = np.fliplr( B3_341[j]*d1[:,:] +  B3_Stl[j]*d2[:,:]
                                + B3_Colb[j]*d3[:,:] + B3_SBI[j]*d4[:,:] )

    print("j, Nb, min(Temp) and max(Temp) in degrees C = ", j, Nb,

    np.min(Temp)-Tref, np.max(Temp)-Tref)



#    ZWind[:,:,0] = Wind[:,:,0]*np.sin(degrees_to_radians * PHI[:,:,0])
#    MWind[:,:,0] = Wind[:,:,0]*np.cos(degrees_to_radians * PHI[:,:,0])

    HS[:,:,0] = C * np.exp( -5107.4/ Temp[:,:,0])
    SOR_2008[:,:,0] = SD * ( B4_341[j])
    LWR_2008[:,:,0] = LD * ( B7_341[j])

    if j % 1000 == 0:
        timecount.append(j)
   #    tempplotdata[:,:,j]=Temp[:,:,0]
    #    lwplotdata[:,:,j]=LWR_2008[:,:,0]
#        swplotdata[:,:,j]=SOR_2008[:,:,0]


    uwindplot.append(ZWind[Xp,Yp,0])
    vwindplot.append(MWind[Xp,Yp,0])
    tempplot.append(Temp[Xp,Yp,0]-Tref)
    lwplot.append(LWR_2008[Xp,Yp,0])
    swplot.append(SOR_2008[Xp,Yp,0])
    humplot.append(REL_HUM[Xp,Yp,0])
    abscissa.append(j)

    #writes to .bin files
    ZWind.ravel(order='F').tofile(ZWind_fid)
    MWind.ravel(order='F').tofile(MWind_fid)
    Temp.ravel(order='F').tofile(T_fid)
    REL_HUM.ravel(order='F').tofile(RH_fid)
    HS.ravel(order='F').tofile(HS_fid)
    SOR_2008.ravel(order='F').tofile(SOR_2008_fid)
    LWR_2008.ravel(order='F').tofile(LWR_2008_fid)


#   if j  % 20 == 0:
#       plt.plot(abscissa, ordinates)
#       readMLdata(j)
#       plt.savefig("CompareOut.png")
#       plt.show()

  if j % 12 == 0:
    if 1 == 0:

        if j<10:
            numstring='0000'+str(j)

        if j<100 and j>=10:
```

```
            numstring='000'+str(j)

        if j<1000 and j>=100:
            numstring='00'+str(j)

        if j<10000 and j>=1000:
            numstring='0'+str(j)



#       imshow(Temp[:,:,0], vmin=265, vmax=300)
        plt.plot(my_341_km, mx_341_km, 'ro')
        plt.plot(my_Stl_km, mx_Stl_km, 'bo')
        plt.plot(my_Colb_km, mx_Colb_km, 'go')
        cbar=plt.colorbar()
        cbar.ax.set_ylabel("Temp K")
        plt.title("Temp plot at %d days" % round(j*3600/86400, 1))
        show()
        plt.savefig('temp'+numstring+'png')
        plt.clf()

#       imshow(SOR_2008[:,:,0], vmin=0, vmax=1000)
        cbar=plt.colorbar()
        cbar.ax.set_ylabel("Shortwave Radiation W/m^2")
        plt.title("SOR plot at %d days" % round(j*3600/86400, 1))
        show()
        plt.savefig('SOR'+numstring+'png')
        plt.clf()

#       imshow(LWR_2008[:,:,0], vmin=0, vmax=600)
        cbar=plt.colorbar()
        cbar.ax.set_ylabel("Longwave Radiation W/m^2")
        plt.title("LWR plot at %d days" % round(j*3600/86400, 1))
        show()
        plt.savefig('LWR'+numstring+'png')
        plt.clf()

        imshow(ZWind[:,:,0], vmin=-20, vmax=20)
        cbar=plt.colorbar()
        cbar.ax.set_ylabel("Wind Speed m/s")
        plt.title("Wind plot at %d days" % round(j*3600/86400, 1))
        show()
        plt.savefig('zwind'+numstring+'png')
        plt.clf()


  #  print(np.max(ZWind), np.min(ZWind), np.max(MWind), np.min(MWind), np.max(Temp),

  np.min(Temp), np.max(HS), np.min(HS), np.max(SOR_2008), np.min(SOR_2008),

  np.max(LWR_2008), np.min(LWR_2008))
#    print("done ", j+1, " of ", Nb)

#gc.collect() }\\

fig=plt.figure()
plt.plot(abscissa, uwindplot)
plt.xlabel("Time (hours)")
plt.ylabel("U Wind speed (m/s)")
plt.savefig("uwindplot.png")
```

```
plt.clf()

fig=plt.figure()
plt.plot(abscissa, vwindplot)
plt.xlabel("Time (hours)")
plt.ylabel("V Wind speed (m/s)")
plt.savefig("vwindplot.png")
plt.clf()

fig=plt.figure()
plt.plot(abscissa, tempplot)
plt.xlabel("Time (hours)")
plt.ylabel("Temperature (degrees C)")
plt.savefig("tempplot.png")
plt.clf()

fig=plt.figure()
plt.plot(abscissa, lwplot)
plt.xlabel("Time (hours)")
plt.ylabel("Longwave radiation (W/m^2)")
plt.savefig("lwplot.png")
plt.clf()

fig=plt.figure()
plt.plot(abscissa, swplot)
plt.xlabel("Time (hours)")
plt.ylabel("Shortwave radiation (W/m^2)")
plt.savefig("swplot.png")
plt.clf()

fig=plt.figure()
plt.plot(abscissa, humplot)
plt.xlabel("Time (hours)")
plt.ylabel("Relative Humidity")
plt.savefig("humplot.png")
plt.clf()
'''
fig=plt.figure()
ax=plt.subplot(111)
colorplot=ax.pcolormesh(tempplotdata[:,:,0], vmin=265, vmax=300)
ax.set_xlabel("X Coord")
ax.set_ylabel("Y coord")
cbar=plt.colorbar()
cbar.ax.set_ylabel("Temperature (degrees K)")
ax.set_aspect('equal')
ax.set_title('Plotted at t=0 hours')
def animate(itermov):
    ax.set_title('Plotted at t={} hours' % timecount[itermov])
   colorplot.set_array(tempplotdata[:,:,itermov])
anim= animation.FuncAnimation(fig, animate, blit=False, repeat=False)
anim.save("tempmovie.mp4")
plt.clf()

fig=plt.figure()
ax=plt.subplot(111)
colorplot=ax.pcolormesh(swplotdata[:,:,0], vmin=0, vmax=500)
ax.set_xlabel("X Coord")
ax.set_ylabel("Y coord")
cbar=plt.colorbar()
cbar.ax.set_ylabel("Shortwave Radiation")
```

```
ax.set_aspect('equal')
ax.set_title('Plotted at t=0 hours')
def animate(itermov):
    ax.set_title('Plotted at t={} hours' % timecount[itermov])
    colorplot.set_array(swplotdata[:,:,itermov])
anim= animation.FuncAnimation(fig, animate, blit=False, repeat=False)
anim.save("swmovie.mp4")
plt.clf()

fig=plt.figure()
ax=plt.subplot(111)
colorplot=ax.pcolormesh(lwplotdata[:,:,0], vmin=0, vmax=500)
ax.set_xlabel("X Coord")
ax.set_ylabel("Y coord")
cbar=plt.colorbar()
cbar.ax.set_ylabel("Longwave Radiation")
ax.set_aspect('equal')
ax.set_title('Plotted at t=0 hours')
def animate(itermov):
    ax.set_title('Plotted at t={} hours' % timecount[itermov])
    colorplot.set_array(lwplotdata[:,:,itermov])
anim= animation.FuncAnimation(fig, animate, blit=False, repeat=False)
anim.save("tempmove.mp4")
plt.clf()
'''

ZWind_fid.close()
MWind_fid.close()
T_fid.close()
RH_fid.close()
HS_fid.close()
SOR_2008_fid.close()
LWR_2008_fid.close()
```

A.3 Python Routine for the Inverse Distance Weighting Interpolation Method

For the Lake Erie Base Case, Case 2 and Case 3, we used the Python routine below (excerpted from A.2) while we manipulated the routine to vary some of the forcing parameters for the other Lake Erie Cases.

```
ZWind[:,:,0] = np.fliplr( u_341[j]*d1[:,:] +  u_Stl[j]*d2[:,:]
                          + u_Colb[j]*d3[:,:] + u_SBI[j]* d4[:,:] )
MWind[:,:,0] = np.fliplr( v_341[j]*d1[:,:] +  v_Stl[j]*d2[:,:]
                          + v_Colb[j]*d3[:,:] + v_SBI[j]* d4[:,:] )

PHI[:,:,0] = np.fliplr( wind_dir_341[j]*d1[:,:] +  wind_dir_Stl[j]*d2[:,:]
                        + wind_dir_Colb[j]*d3[:,:] + wind_dir_SBI[j]*d4[:,:] )
```

```
Temp[:,:,0] = np.fliplr( B2_341[j]*d1[:,:] + B2_Stl[j]*d2[:,:]
                    + B2_Colb[j]*d3[:,:] + B2_SBI[j]*d4[:,:] )# / 4 + 3*Tref/4
REL_HUM[:,:,0] = np.fliplr( B3_341[j]*d1[:,:] +  B3_Stl[j]*d2[:,:]
                                + B3_Colb[j]*d3[:,:] + B3_SBI[j]*d4[:,:] )
```